# Feasibility Study of UHMWPE Fibre-based Impact Shielding for Spacecraft Applications

On the Modelling of Hypervelocity Impact using Smoothed Particle Hydrodynamics

B. Verheijen

MSc. Thesis

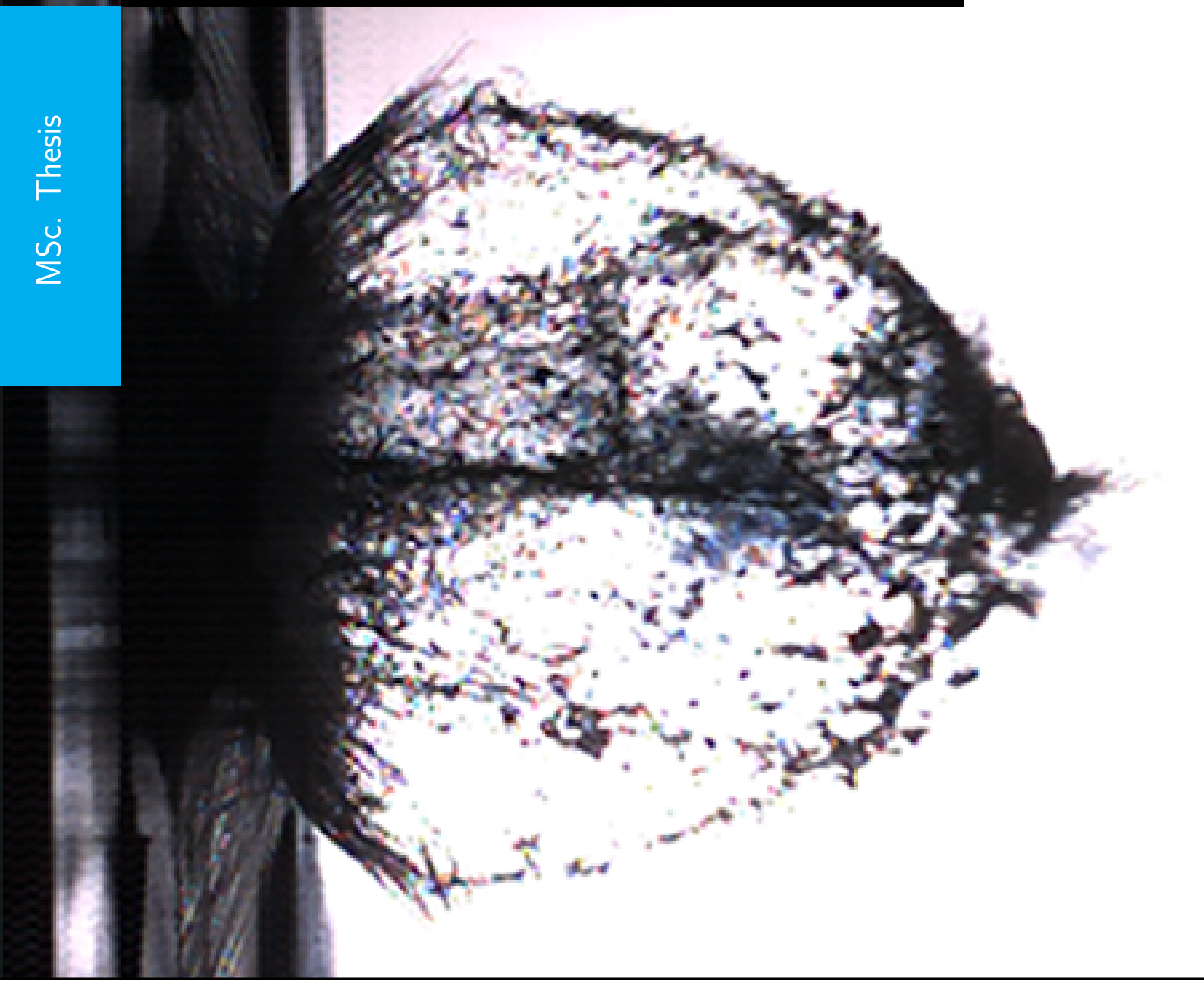

TU Delft Delft University of Technology

Aerospace Structures and Materials

# Feasibility Study of UHMWPE Fibre-based Impact Shielding for Spacecraft Applications

## On the Modelling of Hypervelocity Impact using Smoothed Particle Hydrodynamics

MSc. Thesis

B. Verheijen

Supervisor: Dr.ir. O.K. Bergsma

14 December 2017

Faculty of Aerospace Engineering · Delft University of Technology

This thesis was supported by DSM Dyneema® . Their support is gratefully acknowledged. Impact footage, as used on the cover page, was provided by the Fraunhofer Institute


Delft University of Technology
Department of Structural Integrity and Composites

The undersigned hereby certify that they have read and recommend to the Faculty of Aerospace Engineering for acceptance a thesis entitled

# Feasibility Study of UHMWPE Fibre-based Impact Shielding for Spacecraft Applications

by

B. Verheijen

in partial fulfillment of the requirements for the degree of

Master of Science in Aerospace Engineering

Dated: 14 December 2017

Chair Holder:

Dr.ir. R.C. Alderliesten

Committee members:

Dr.ir. O.K. Bergsma

Dr.ir. W. van der Wal

Ir. M.J. Schuurman

# Abstract

Spacecraft are under constant threat of structural damage from hypervelocity impacts by micrometeoroids and orbital debris. To bolster the shielding used for protection against these impacts, ballistic materials can be employed. Aramid-based materials are currently used aboard the International Space Station (ISS), but Ultra High Molecular Weight PolyEthylene (UHMWPE) fibres are a common alternative for ballistic protection on Earth. In this report, the suitability of UHMWPE-based composites for spacecraft impact shielding is investigated. Hypervelocity impact simulations using smoothed particle hydrodynamics discretisation form an essential part of the design and analysis of such protection systems. Two formulations of nonlinear orthotropic hydrocode models are proposed for this purpose, which are validated using footage from hypervelocity impact experiments on Dyneema® HB26 targets. One of the proposed models yields good prediction of residual impactor velocities, generally being within 10% of experimental data. The other reproduces both residual velocities and debris cloud shape well for the highest considered impact velocities, but suffers from decreased performance as the ballistic limit is approached. Numerical comparison between UHMWPE- and aramid-based composites shows comparable ballistic performance for the considered cases.

# Preface

This Master Thesis came about through a conversation with Dr. Gransden. The wish list for a Thesis topic consisted of a project containing composites, impact, numerical modelling and an experimental component. Dr. Gransden replied he did not have a project with this description laying ready, but that he had wanted to get research into the field of hypervelocity impact going at the faculty for a long time. He suggested investigating the suitability of Dyneema® based composites for spacecraft, maybe involving some radiation ageing experiments. He brought up the idea with Dr. Van der Werff, who works at DSM. He in turn involved Dr. Heisserer who specialises in impact simulations at DSM. All parties involved were very enthusiastic about the plan, and so it began.

A paper containing the latest incarnation of an impact model for Dyneema® HB26 formed the tarting point for the project. The initial project plan consisted of a two pronged approach. Step one was to modify the model to use it in combination with a Smoothed Particle Hydrodynamics discretisation. Shielding systems aboard the ISS currently use Kevlar® based shielding systems. A Smoothed Particle Hydrodynamics based material model for Kevlar fibre reinforced polymers was available, so a comparison of the impact response for the two materials would be made based on simulations. Step two would involve radiation ageing experiments using proton radiation to characterise the expected effects of the space radiation environment on the mechanical properties and molecular structure of gel-spun UHMWPE polymers.

The plan was ambitious, and as it turned out, somewhat too ambitious for a single Master Thesis. First, it was found that converting existing Dyneema® HB26 impact models to models suitable for use with Smoothed Particle Hydrodynamics would be more involved than expected. Second, obtaining radiation time at a proton radiation facility proved more time consuming than expected. In the end, both of these tasks where achieved, but time ran out. The scope of the project was redefined to only encompass hypervelocity impact modelling. Performing the radiation ageing experiments and ballistic testing were decided to be part of a potential follow up project. The results of this Thesis project were presented at the $9^{th}$ conference of the International Association for the Advancement of Space Safety.

# Acknowledgements

I would like to start of by thanking Dr. Derek Gransden and Dr. Otto Bergsma for supervising me during this thesis, providing feedback and guidance wherever required. I would also like to thank Dr. Ulrich Heisserer and Dr. Harm van der Werff from DSM Dyneema for their enthusiasm regarding the project, their input, and their willingness to help out whenever possible.

I would also like to thank the external parties whose expertise made this project possible. Without the support of Dr. Long Nguyen from the Australian Government Department of Defence Science and Technology Group, and Dr. Torsten Lässig and Prof. Werner from the Fraunhofer Institut it would not have been possible to master the fundamentals of high speed dynamical processes and their modelling within the scope of this project. To Dr. Mark Millinger from the European Space Agency and Dr. Marc-Jan van Goethem from the KVI-Center for Advanced Radiation Technology I owe a debt of gratitude for the time and effort they spent on helping me understand spacecraft radiation testing and design of radiation ageing experiments respectively. I am very sorry the radiation testing originally proposed did not come to fruition.

Last, I would like to thank Tomasso Sgobba from the International Association for the Advancement of Space Safety and Dr. Michael Kezirian and Prof. Stuart Phoenix from the International Space Safety Foundation for their support. This project was backed by the ISSF Graduate Student Fellowship Program.

Delft, University of Technology — B. Verheijen
14 December 2017

# Summary

HyperVelocity Impacts (HVI) from micrometeoroids and orbital debris form a constant threat to the safety of spacecraft. Multi-layered shielding systems containing ballistic composites, such as the Stuffed Whipple Shield (SWS), can be used for protect against such events. The SWS configurations in use on the International Space Station (ISS) use aramid-based composites. For ballistic protection on Earth, Ultra High Molecular Weight PolyEthylene (UHMWPE) fibre-based composites are widely used. The objective of this project is to assess the feasibility of UHMWPE-based HVI shielding for spacecraft applications.

A thorough literature review identified three aspects of the space environment that could potentially cause degradation to UHMWPE-based composites. These are exposure to extreme temperatures, atomic oxygen and radiation. Proper design of shielding configurations is expected to be able to mitigate these threats. It was also found that UHMWPE possessed radiation shielding properties that could be valuable for spacecraft applications.

HVI simulations using Smoothed Particle Hydrodynamics (SPH) discretisation form a valuable tool in the design and analysis of spacecraft HVI shielding solutions. To this end, two new nonlinear orthotropic hydrocode material models were created for the simulation of hypervelocity impacts in Dyneema® HB26. Validation was performed using experimental footage of HVI experiments.

Simulations were performed for equal areal density test cases using both formulated Dyneema® models and a published Kevlar®-epoxy model. These involved both direct impact test cases, and cases where the composite materials were placed inside and SWS. These test cases showed comparable ballistic performance for both UHMWPE- and aramid-based systems. Additional experimental testing is recommended to serve as validation material and to provide further insights on the relative HVI performance of the two types of ballistic materials. Preliminarily, UHMWPE-based spacecraft HVI shielding is deemed feasible. Further research on the topic is recommended.

# Table of Contents

# Glossary

## List of Acronyms

| | |
|---|---|
| AD | Areal Density |
| AO | Atomic Oxygen |
| CFRP | Carbon Fibre Reinforced Polymer |
| CME | Coronal Mass Ejections |
| DM | Dyneema Model |
| EOS | Equation Of State |
| FOD | Foreign Object Damage |
| GCR | Galactic Cosmic Radiation |
| GUI | Graphical User Interface |
| HVI | HyperVelocity Impact |
| HZE | High atomic number (Z) and Energy |
| IFPI | Inverse Flyer Plate Impact |
| IM | Intermediate Model |
| ISS | International Space Station |
| KFRP | Kevlar Fibre Reinforced Polymer |
| LEO | Low Earth Orbit |
| MMOD | MicroMeteoroids and Orbital Debris |
| NEE | Near Earth Environment |
| SHB | Split Hopkinson Bar |
| SPE | Solar Particle Event |
| SPH | Smoothed Particle Hydrodynamics |
| SWS | Stuffed Whipple Shield |
| UHMWPE | Ultra High Molecular Weight PolyEthylene |

# List of Symbols

### Latin Symbols

| Symbol | Description | Unit |
|---|---|---|
| $A$ | Polynomial EOS Material Constant | $[Pa]$ |
| $B$ | Polynomial EOS Material Constant | $[-]$ |
| $C$ | Stiffness Matrix Entry | $[Pa]$ |
| $C$ | Damage Coupling Coefficient | $[-]$ |
| $D$ | Damage Parameter | $[-]$ |
| $G$ | Fracture Energy | $[J/m^2]$ |
| $L$ | Characteristic Cell Length | $[m]$ |
| $S$ | Shock Wave Velocity Relationship Parameter | $[-]$ |
| $S$ | Ultimate Stress | $[Pa]$ |
| $V$ | Velocity | $[m/s]$ |
| $V$ | Volume | $[m^3]$ |
| $W$ | Weighting Function | $[-]$ |
| $a$ | Orthotropic Yield Model Control Parameter | $[-]$ |
| $c$ | Bulk Sound Speed | $[m/s]$ |
| $c^*$ | Cunniff Velocity | $[m/s]$ |
| $e$ | Failure Initiation Parameter | $[-]$ |
| $e$ | Energy | $[J]$ |
| $h$ | Smoothing Length | $[m]$ |
| $k$ | Yield Surface Constant | $[-]$ |
| $m$ | Mass | $[kg]$ |
| $n$ | Counter | $[-]$ |
| $p$ | Pressure | $[Pa]$ |
| $p$ | Linear Momentum | $[Nm]$ |
| $s$ | Stress Tensor | $[Pa]$ |
| $t$ | Time | $[s]$ |
| $v$ | Particle Velocity | $[m/s]$ |
| $\mathbf{x}$ | Node Location Vector | $[m]$ |

### Greek Symbols

| Symbol | Description | Unit |
|---|---|---|
| $\Gamma$ | Mie-Grüneisen Coefficient | $[-]$ |
| $\Delta$ | Discrepancy | $[-]$ |
| $\delta$ | Kronecker Delta | $[-]$ |
| $\varepsilon$ | Strain | $[-]$ |
| $\mu$ | Compression Term | $[-]$ |

| | | |
|---|---|---|
| $\rho$ | Density | $[kg/m^3]$ |
| $\sigma$ | Stress | $[Pa]$ |

### Subscripts

| Symbol | Description |
|---|---|
| $0$ | Initial Condition |
| $0$ | State before Shock Wave |
| $1$ | State after Shock Wave |
| $cr$ | Critical Value |
| $eff$ | Effective Value |
| $E$ | Difference with Experimental Data |
| $fs$ | Free Surface |
| $f$ | Fibre Property |
| $H$ | Hugoniot State |
| $ii$,$ij$ | Material Direction |
| $I$ | Difference within Simulation Series |
| $S$ | Shock Wave Property |
| $u$ | Ultimate Value |
| $x$ | X-direction |
| $y$ | Y-direction |

### Superscripts

| Symbol | Description |
|---|---|
| $\bar{}$ | Master Effective Parameter |
| $\dot{}$ | Rate |
| $Dev$ | Deviatoric |
| $p$ | Plastic |
| $Vol$ | Volumetric |

# List of Figures

# List of Tables

"Everything is physics."

— *Drs. Michael F. van Kempen*

# Chapter 1

# Introduction

The time space exclusively was the playing field where nations displayed their engineering prowess by going higher, longer, faster and further is long gone. The Near Earth Environment (NEE) has become a valuable resource mankind uses to deal with challenges on Earth. Satellite navigation, telecommunications and atmospheric observation are just some examples of how the exploitation of space has become ingrained into everyday life. More audacious plans, such as the return of man to the Moon, travel to Mars, asteroid mining and even more exiting concepts are also becoming ever more concrete. With space infrastructure becoming more mature, ensuring the safety of its various elements becomes ever more important. One substantial threat experienced by spacecraft is that of Foreign Object Damage (FOD). Impacts from MicroMeteoroids and Orbital Debris (MMOD), travelling at relative velocities on the order of kilometres per second, can cause significant damage to spacecraft. The implications of this threat are magnified in the NEE by the fact that ever since man started his space activity, significant amounts of man-made space debris have been produced. This is a problem that is not showing any signs of abating in the near future. For missions outside the NEE, the fact that rescue of a spacecraft and its crew are not an option weighs heavily on the amount of protection warranted. Therefore, it is of paramount importance that spacecraft, manned and otherwise, are adequately protected against the threat of hypervelocity impact damage.

Part of the arsenal of protection options available to engineers are ballistic fibre materials, such as Kevlar® or Dyneema®, or composites reinforced with these kinds of fibres. Because of the widespread use of these materials in terrestrial personal and vehicle protection systems, numerical impact simulation models are usually geared towards simulation of impacts in the ballistic velocity range, rather than the HyperVelocity Impact (HVI) range encountered in space. The objective of this project is to assess the suitability of ballistic composites containing Ultra High Molecular Weight PolyEthylene (UHMWPE) fibres, e.g. Dyneema®, to spacecraft protection applications. To this end, two numerical models are proposed that can be used to simulate HVI using Smoothed Particle Hydrodynamics (SPH) in Dyneema® HB26 based composites. Formulating these models has yielded insights into the process of hypervelocity modelling of ballistic composites. Further development of these models will help in the design of ballistic composite protection systems for HVI applications.

Chapter 2 contains an overview of the research objectives and research questions that drove the work presented in this report. In Chapter 3 a literature review is presented that provides background information required to reach these objectives. An overview of

the modelling approach and the modelling tools used throughout this work is provided in Chapter 4. Validation of the material models used for the modelling of SPH-based metallic components, namely impactor and certain wall structures, and particle density refinement studies for these components are presented in Chapter 5. In Chapter 6, an existing material model formulation for Dyneema® HB26, designed for use with an element-based mesh, is combined with and SPH-based discretisation. In this chapter observed discrepancies between numerical and experimental data are reported, as is the approach taken to determine the cause of these discrepancies. Chapter 7 subsequently contains two new material model formulations for Dyneema® HB26. Particle density refinement studies for targets containing these models are presented in Chapter 8. Evaluation of these models, and validation using experimental data are covered in Chapter 9. Chapter 10 contains a study into the effect of target plate areal density on orthotropic model response. Sensitivity studies for both proposed models are covered in Chapter 11. In Chapter 12, aluminium and ballistic composite models are combined into Stuffed Whipple Shield (SWS) configurations, and a comparative test case is simulated using both Kevlar®- and Dyneema®-based shielding configurations. Conclusions and recommendations are covered in Chapter 13.

# Chapter 2

# Thesis Goals

To guide the course of this Master Thesis, a research objective and research question were defined. The research objective, as presented in Section 2.1, represents the central task set for this project. The research question presented 2.2 represents the central question, to be answered by the research. For both the research objective and question, it holds that they are deliberately phrased in quite broad wordings. Sub-objectives and sub-questions are then formulated to further define and illustrate them.

## 2.1 Research Objectives

The overarching research objective of this Master Thesis is defined as follows:
*Assess the feasibility of UHMWPE fibre-based spacecraft hypervelocity impact shielding in an SWS configuration, by means of numerical impact simulations in ANSYS® Autodyn®.*

This overarching objective has been subdivided into three sub-objectives:

1. Assess the compatibility between UHWMPE fibre-based composites and the space environment, by means of a literature review.
2. Formulate a material model for Dyneema® HB26, compatible with an SPH discretisation, by using modelling options available in ANSYS® Autodyn® R16.2 Academic.
3. Compare the ballistic performance of the formulated Dyneema® HB26 model to that of a published Kevlar®-epoxy composite model, by means of equal areal density, equal configuration simulations using ANSYS® Autodyn® R16.2 Academic.

## 2.2 Research Question

The overarching research question of this Master Thesis is defined as follows:
*Are UHMWPE fibre-based composites a viable material for use in spacecraft hypervelocity impact shielding, if integrated into an SWS structure as currently used aboard the Columbus module of the International Space Station (ISS)?*

This overarching question has been subdivided into 3 sub-questions:

1. What aspects of the space environment are expected to cause degradation to UHMWPE fibre-based composites, thus affecting the ballistic performance of Dyneema®-based spacecraft protection systems?

2. Can the response of Dyneema® HB26 to hypervelocity impacts accurately be predicted using an SPH-based discretisation?

   (a) Can the residual velocity of the debris cloud produced by a hypervelocity impact be predicted?

   (b) Can the general shape of the debris cloud produced by a hypervelocity impact be predicted?

3. How do the ballistic performances of simulated Dyneema®- and Kevlar®-based composites compare in response to hypervelocity impacts?

# Chapter 3

# Literature Review

In this chapter, the literature review that has been performed as part of this Thesis is presented. Its sections have been selected to give the reader a comprehensive overview of the problem at hand. In Section 3.1, the material Dyneema® is introduced, and a review of its properties is presented. In Section 3.2, the fundamentals of ballistic impacts in fibre reinforced composites are discussed. Section 3.3 subsequently covers the shock wave phenomena generally associated with the hypervelocity impact regime. Section 3.4 gives an overview of both historic and contemporary developments in the quest to protect spacecraft from impacts in the hypervelocity range. In Section 3.5 the space environment, and its expected interaction with spacecraft structures are discussed. Literature on the modelling of hypervelocity impacts in Dyneema®, as well as the modelling of KFRP and Carbon Fibre Reinforced Polymer (CFRP) is discussed in Section 3.6.

## 3.1 Background Information on Dyneema®

The name Dyneema® refers to fibres consisting of highly crystalline, highly oriented Ultra High Molecular Weight Polyethylene UHMWPE, produced by DSM. UHMWPE, in turn, consists of very long chains of carbon atoms, fully saturated with hydrogen. "Very long", in this case, means a molecular weight in the range of $3.5 - 7.5 \cdot 10^6\ g \cdot mol^{-1}$ [1]. Through a process of gel-spinning and drawing these long, initially tangled, molecules become aligned. This process yields a material with high crystallinity (in excess of 85%) and a highly degree of orientation (in excess of 95%) [2].

The desired consequence of this high degree of orientation is that Dyneema fibres carry tensile loads mostly through very strong, intra-molecular covalent bonds. This is combined with a simple molecular structure, allowing for dense packing. The result is a fibre with very high tensile strength and stiffness, both on a per unit mass and volume basis, often outperforming materials such as carbon and aramid fibre when it comes to these properties [2]. The simple molecular structure of UHMWPE also means it generally has superior chemical and UV radiation resistance to aramid-based materials [2].

One notable downside of UHMWPE-based material, to be revisited in Subsection 3.5.2, is a relative sensitivity to high temperatures when compared to aramid. With material melting starting at approximately 150 $°C$ [3], prolonged exposure to high temperatures may affect the crystallinity and orientation of the material, with reduced material properties as a result.

## 3.2 Background Information on Ballistic Impact Shielding

As described in Section 3.1, fibrous materials such as Dyneema excel when loaded in tension. Combining fibres in multiple directions, as done in fabrics or multi-directional laminates, creates a state in which out-of-plane loading translates into an in-plane membrane response of the material. Cunniff [4] proposed that the ballistic performance of a fibre based ballistic material is proportional to the Cunniff velocity $c^*$, presented in Equation 3-1. In this equation, the subscript $f$ indicates fibre properties are considers and $u$ refers to ultimate properties.

$$c^* = \left( \frac{\sigma_{u,f} \varepsilon_{u,f}}{2\rho_f} \sqrt{\frac{E_f}{\rho_f}} \right)^{\frac{1}{3}} \tag{3-1}$$

The quantity $\frac{\sigma_{u,f} \varepsilon_{u,f}}{2\rho_f}$ represents the specific work to cause fibre breakage at the ultimate strength, under the assumption of linear elastic behaviour until failure. The quantity $\sqrt{\frac{E_f}{\rho_f}}$ represents the bulk speed of sound along the fibre direction. Increasing this latter property increases the information propagation speed in the material, allowing more material to become involved in the membrane stretching.

For use in ballistic protection applications, it is required that the material properties used in Equation 3-1 are not lost at high strain rates. Hudspeth et al. [5] and Sanborn et al. [6] tested Dyneema® SK76 single fibres at rates up to $1.156 \cdot 10^3\ s^{-1}$ and $0.600 \cdot 10^3\ s^{-1}$ respectively, and found material performance was generally not adversely affected by higher strain rates. Note that during hypervelocity impacts, typical strain rates are on the order of $1.0 \cdot 10^6\ s^{-1}$ [7]. Limits on characterisation techniques generally make data at such strain rates difficult to obtain. Therefore hypervelocity impact experiments are often used to proof material suitability to armour concepts [8].

The importance of membrane behaviour is illustrated by Karthikeyan et al. [9] and O'Masta et al. [10]. They found that preventing the fibre reinforced composites from flexing out-of-plane reduced their ballistic performance. Karthikeyan et al. achieved this by varying the used matrix material, and O'Masta et al. by providing an aluminium backing to their Dyneema® target. In such cases, the shearing of the fibres and crushing of the composite becomes the dominant energy absorption phenomena, rather than tensile failure of the fibre. Nguyen et al. [11] found that for thick laminates, this behaviour can also be self-induced. For these laminates, the presence of bulk material on the back prevents membrane behaviour at the impact face. This creates a region at the impact face in which shear plugging dominates, and a region at the back face where bulging occurs.

## 3.3 Background Information on Shock Waves in Solids

In Section 3.2 it was pointed out that the speed of sound along the fibres is the measure that dictates the upper limit to how rapidly a composite plate can respond to an impact. When the velocity of the impactor exceeds this value, the target material will not have time to globally respond during the impact process. For space applications, relative velocities are generally on the order of kilometres per second or higher [12, 13]. Well above the reported through-thickness speed of sound of 1922 $m/s$ reported for Dyneema® HB26 [8]. At these velocities, the shock waves that arise in solids as consequence of the impact become important.

For a more elaborate discussion on the conditions under which a shock wave arises, the reader is referred to [7]. In short, a shock wave is a pile-up of pressure waves, which becomes so strong that material states change instantaneous over the wave front. The state variables of concern here are pressure ($p$), density ($\rho$), energy ($e$) and particle velocity ($v$). To relate the unknown material states behind the shock wave (denoted by subscript 1) to the known states before it (denoted by subscript 0), conservation equations are used. These equations are called the Rankine-Hugoniot, or Hugoniot, equations. Conservation of mass, momentum and energy respectively yield Equation 3-2 to 3-4. These are taken from [7] and presented in their most general form. The subscript $S$ stands for properties of the shock wave.

$$\rho_0(v_S - v_0) = \rho_1(v_S - v_1) \tag{3-2}$$

$$p_1 - p_0 = \rho_0(v_S - v_0)(v_S - v_1) \tag{3-3}$$

$$p_1 v_1 - p_0 v_0 = \rho_0(v_s - v_0)\left(e_1 - e_0 + \frac{v_1^2}{2} - \frac{v_0^2}{2}\right) \tag{3-4}$$

These three equations form a single set of solutions in $p-V-e$ space that lay on the state surface of the material. This curve forms the set of all possible peak conditions after the shock wave. To solve for the four unknown state variables after the shock wave, four equations are needed. This set is completed by Equation 3-5. This equation represents the material specific relationship between the velocity of the shock wave and the particle velocity behind the shock. The $S$ parameters are used to fit the function. This $v_S - v_1$ relationship can be derived from Inverse Flyer Plate Impact (IFPI) experiments. The series are usually truncated at the third order term for gasses and porous materials, and at the first order term for other solids, leading to Equation 3-6. Equation 3-2 to 3-6 fully describe the Hugoniot state.

$$v_S = c_0 + \sum_{i=1}^{n} S_i v_1^i \tag{3-5}$$

$$v_S = c_0 + S v_1 \tag{3-6}$$

The pressure in the shocked state consists of the Hugoniot pressure and a term related to the change in thermal energy of the shocked medium. To capture this interaction between energy and pressure in the shocked medium, an Equation Of State (EOS) is required. As will be elaborated on in Section 4.1.1, the choice of EOS for composite materials is limited. The two available formulations considered for this thesis are the Mie-Grüneisen EOS with either the Shock or the polynomial formulation. The Shock formulation is presented in Equation 3-7. The $\Gamma(V)$ term is called the Grüneisen coefficient and is a volume dependent material parameter, which is often taken as a constant for simulation purposes [14]. The $H$ subscript refers to Hugoniot states. .

$$p(V,e) = p_H + \frac{\Gamma(V)}{V}(e - e_H) \tag{3-7}$$

Different formulations for the relationship presented in Equation 3-7 can be used, as long as they possess the same physical characteristics. The polynomial formulation, is presented in Equation 3-8.

$$p(V,e) = A_1\mu + A_2\mu^2 + A_3\mu^3 + (B_0 + B_1\mu)\rho_0(e - e_H) \tag{3-8}$$

The $\mu$, $A_1$, $A_2$ and $A_3$ parameters are as defined in Equation 3-9 to 3-12. The $B_0$ and $B_1$ parameters can be selected to enforce certain relationships between $\Gamma$ and $\rho$ that follow from the volume dependence indicated in Equation 3-7.

$$\mu = \frac{\rho}{\rho_0} - 1 \tag{3-9}$$

$$A_1 = \rho_0 c_0^2 \tag{3-10}$$

$$A_2 = \rho_0 c_0^2(1 + 2(S-1)) \tag{3-11}$$

$$A_3 = \rho_0 c_0^2(2(S-1) + 3(S-1)^2) \tag{3-12}$$

Characterisation of the shock Hugoniot is generally performed through IFPI experiments. The dataset used in this thesis is that used by Lässig et al [8] and Nguyen et al. [15], which is based on experiments from Hazell et al. [16] and Lässig et al [17].

From the information presented in the current Section and Section 3.2, it becomes apparent that as the impactor velocity increases and eventually reaches the HVI stage, the phenomena that govern the impact process change. Penetration itself is mostly caused by the impactor compressing the material in its trajectory, causing it to shear away from the target bulk. Compressive shock waves propagate outwards from the impact site. If these waves reach free surfaces, they become reflected, creating regions of tensile stress. If this stress exceeds the spall strength of the material, cavitation and fragmentation will occur. This phenomenon is known as spallation and is why, even if penetration does not occur, secondary debris from the back face of an impacted surface can still pose a danger to the contents of a vessel [7].

## 3.4 Background Information on Spacecraft Protection

Spacecraft protection systems can take many forms, depending on the available mass, volume and monetary budgets, and required level of protection.

### 3.4.1 Historic Developments

One of the earliest proposed dedicated spacecraft impact protection measures is "meteor bumper" proposed by Dr Fred Whipple [18]. It consisted of a metallic outer bumper, placed at some distance from the spacecraft outer wall. This bumper would serve to fragment incoming foreign objects, dissipating some of the impactor energy, and spreading the impact on the actual spacecraft wall out over a larger area. The concept proved effective, has been applied ever since, and is currently known as a Whipple Shield.

#### Outer Bumper Material

Swift and Hopkins [19] investigated the effect of different outer bumper materials on the protection offered by a Whipple shield. Hypervelocity impact experiments using aluminium impactors were used for this campaign, which is often recommended as approximation for orbital debris because of the match in average density [20]. They observed that as long as the material density of the bumper was above 2 $g \cdot cm^{-3}$, ballistic protection was more or less independent of material choice. Low melting and sublimation energy values appeared to further improve ballistic protection above this point. It was found that the ballistic protection offered by Whipple Shields rapidly decreased as the density of bumper materials dropped below this limit density value. Destefanis et al. [21] compared a titanium and aluminium outer bumper in a Kevlar®-based SWS, and found comparable protection for both. These observations imply that in the hypervelocity impact regime, material strength plays a diminishing role in the ballistic protection offered by the outer bumper. This observation may have been influenced by the choice of impactor. The density of aluminium (2.8 $g \cdot cm^{-3}$) is quite close to the suggested limit bumper density.

Hiermaier [7] discusses the state of the debris could, calculated using a Tillotson EOS, based on impact velocity. Impactor and bumper material are not given [7], and the original data from Schonberg [22] were not available, but in similar publications Schonberg used aluminium impactors and bumpers [23]. From about 4 $km/s$ the fraction of liquid in the debris cloud increases approximately linearly to a fraction of 1.0 at about 9 $km/s$. Vapour material starts to occur around 12 $km/s$. The significant amount of melting during the impact process, provides an explanation of the transition from strength dominated to density and transition energy dominated shielding performance.

### Additional Bumper Layers

A minimal density threshold for outer bumpers would mean lightweight composite materials, such as Dyneema®-based composites, are not ideal for this purpose from a ballistic protection point of view. Schonberg and Walker [24] hypervelocity impact experiments on Whipple shielding configurations where the ballistic composites did not replace the outer bumper, but were added as additional layers between the outer bumper and spacecraft wall. This configuration is known as a Stuffed Whipple Shield, and is illustrated in Figure 3.1. As stuffing layer, they used aluminium-, and Kevlar®- and Spectra®-based (Alternative brand of UHMWPE fibres) composite bumpers. Using ballistic composites as stuffing layer was found to offer better protection when compared to equal Areal Density (AD) configurations consisting only of aluminium. During this test campaign insufficient tests with comparable set-ups were performed to be able to distinguish between the performance of the Spectra®- and Kevlar®-based composites.

Christiansen and Kerr [25] also experimented using both Kevlar®- and Spectra®-based stuffing materials. Based on their tests, again, global ballistic performance of Kevlar®- and Spectra®-based shields appeared to be comparable.

From the publication by Christiansen and Kerr [25] onwards, research into UHMWPE-based SWS has not been found. For both the American and European contributions to the ISS, Kevlar®-based SWS protection systems were eventually selected. No explicit explanation for this choice has been found in literature, and direct questions to ESA [26] also did not yield conclusive answers. It is suspected sensitivity to either atomic oxygen or high temperature, as will be covered in Subsection 3.5.1 and 3.5.2 respectively, are part of this decision.

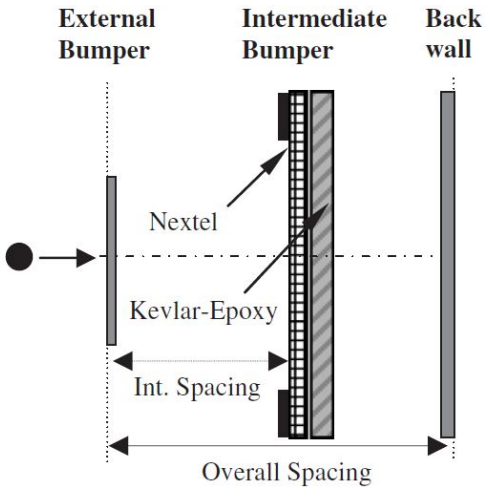


**Figure 3.1:** A representation of the SWS configuration as used aboard the Columbus module of the ISS. Figure obtained from Destefanis et al. [21].

### 3.4.2 State of the Art

Screening for potentially promising impact shielding materials and configurations, is still very much an experimental business [21, 27, 28, 29, 30]. This places a heavy reliance on hypervelocity impact experiments using light gas gun. This approach has its trade-offs. Creating tests set-ups may be rather straight forward. However, the costs associated with operating a light gas gun generally means repetition of tests on individual configurations is limited. Furthermore, Destefanis et al. [21] remark upon the fact that hypervelocity impact testing itself is prone to threshold effects. At the used energy levels, slight variations in impactor velocity, material properties or set-up choice can have dramatic effects on test results. Thoma et al. [31] proposed a shift towards careful material characterisation and numerical modelling to support the screening of new material. High strain rate characterisation, such as flyer plate experiments, are also costly and often still fall short of actual MMOD impact velocities. In the end, a mix of the flexibility of modelling and the validity of experimentation will most likely be most effective.

One recurring theme in contemporary spacecraft shielding research is the proposed use of foam materials. The considered foam materials vary [21, 29], but aluminium is a recurring choice [27, 28, 29, 30]. The underlying reason for this interest is the hypothesis that the many cell walls in the foam will repeatedly shock the impactor and its fragments, causing more effective fragmentation than equal AD monolithic aluminium walls. Integrating foams into sandwich panels seems particularly promising, since it negates the debris channelling effect often caused by the honeycomb cells in honeycomb sandwich structures [27]. When compared to an SWS, foam-based sandwich structures save non-ballistic weight by omitting components such as spacers, stiffeners and fasteners. However, when Destefanis et al. [21, 30] considered both aluminium foam-based shielding systems and shielding as applied in the Columbus module, they found that the aluminium foam configuration did not necessarily outperform the fibre-based Columbus configuration.

These contemporary sources [21, 27, 28, 29, 30] do not focus on UHMWPE fibre-based ballistic configurations. However, there is significant interest in the use of UHMWPE-based materials in the space industry for another reason. As will be explained in more detail in Subsection 3.5.3, UHMWPE is the best structural material to protect against High atomic number (Z) and Energy (HZE) radiation particles. Authors such as Khatiwada et al. [32] and Sen et al. [33] consider it for its combination of structural and radiation shielding properties.

## 3.5 Background Information on the Space Environment

One of the major challenges of the design of structures and mechanisms for spacecraft is that they do not only have very high performance requirements, but that they also have to keep meeting these requirements after prolonged exposure to very demanding environmental conditions. This section contains an overview of several facets of the

space environment that were identified as potentially threatening to the performance of ballistic composites in SWS configurations. The expected effects of these environmental factors on the mechanical properties of Dyneema® fibres and the ballistic performance of Dyneema®-based composites and identified knowledge gaps are also discussed.

### 3.5.1 Atmospheric Considerations

#### Atomic Oxygen Environment

Atomic Oxygen (AO) is present in the upper atmosphere and forms the bulk of its constituent particles between 200 and 600 km altitude. It is highly reactive when brought into contact with organic molecules, causing potential degradation of performance. Since it is created as a consequence of solar radiation, its effects and presence are not only a function of altitude, but also of solar activity [34].

#### Atomic Oxygen Effects

Finckenor et al. [35] exposed both Kevlar® and UHMWPE yarns (of unspecified make and model) to AO streams of about 5 MeV, which they state is representative of that as experienced by the ISS. The UHMWPE fibres show rapid decrease in strength with particle fluence, when compared to the Kevlar fibre. However, for the UHMWPE, neither the brand, nor the type, nor the linear mass density of the yarns is reported. For the Kevlar, the linear mass density is also not presented. Since for the pristine material samples, an equal failure load is observed, it is possible both materials were not of equal linear mass density. Requisition of original test data, or reproduction of the experiment with equal linear mass density Dyneema and Kevlar samples is recommended.

### 3.5.2 Thermal Considerations

#### Thermal Environment

An inherent problem of describing the thermal environment in space, is that since space is a vacuum, it has no temperature for engineering intents and purposes. The temperatures of different parts of the spacecraft are strongly influenced by a number of factors. Spacecraft surfaces can be exposed to direct sunlight, or empty space at 3 K [13]. The mission profile, spacecraft design choices and even the applied coating can strongly influence the temperatures of different regions. Typical reported operational temperature windows were found to range from $-100$ °C to 100 °C for antennas [34] and $-150$ °C to 110 °C for solar arrays [34, 36]. Since these are both external subsystems, it is expected spacecraft thermal control systems can generally maintain these temperature ranges. Most subsystems have significantly narrower thermal operating windows [34, 36]. In the end, a mission and spacecraft specific thermal analysis will be required to ascertain whether a certain design solution is compatible with its intended operating window.

#### Thermal Effects

When assessing temperature effects on a material, two time scales are relevant. First, there are the direct changes in material properties at different temperatures. Second, there are the effects associated with thermal ageing.

DSM Dyneema [37] investigated temperature effects by heating Dyneema® SK76 yarns up to 100°C. Tensile tests at rates of 3.5 $\%s^{-1}$, 35 $\%s^{-1}$ and 350 $\%s^{-1}$ indicated that a Cunniff velocity of 90% to 95% of the reference value was retained. Peijs et al. [38] tested Dyneema® SK60 yarns up to 80 °C at strain rates of $10^{-4}s^{-1}$ to $4 \cdot 10^{-2}s^{-1}$. They observed a decrease of about 15% in material strength at 80 °C as compared to room temperature. They also observed that the loss in strength reduced as the used strain rate increased.

For the consulted literature on the topic of accelerated ageing of UHMWPE fibres, yarns or composites [37, 39, 40] [41, 42], all focus on ageing in a terrestrial environment. Settings vary, but in general, samples are stored in air, at one or more predefined temperatures (ranging from 65°C to 130°C), at a controlled humidity. Loss of properties such as strength or ballistic limits tend to increase with time, and increase more rapidly at higher temperatures. Results range from retention of 95 % of the ballistic limit after up to 20 weeks of ageing at temperatures up to 90°C [37], to retention of 90 % and 10 % of tenacity after 70 hours at 90°C and 130°C respectively [40]. However, obtained results vary between the different authors. On the effects of accelerated ageing under space representative conditions, such as a lack of atmosphere or repeated thermal cycling over a wide range of space representative temperatures, no studies were found.

### 3.5.3 Radiation Considerations

#### Radiation Environment

The space radiation environment can roughly be divided into three regions [13, 43]. First, the NEE, where the influence of the geomagnetic field dominates. Second is interplanetary space, inside the heliosphere but outside the NEE. Third is all of space outside the heliosphere.

From this third region of space, Galactic Cosmic Radiation (GCR) permeates into the heliosphere. This GCR nominally consists of about 2% electrons, and for 98% out of fully ionized nuclei. Of these nuclei, about 87% are protons, 12% are alpha particles and 1% consists of heavier cores, or HZEs [13, 33, 43, 44, 45]. Energies in the range of hundreds of MeV, up to 100 GeV per nucleon are often reported for these particles [13, 33, 44, 45, 46, 47, 48].

Within interplanetary space, the radiation environment consists of both solar and GCR sources. Solar contributions originate from solar winds and Solar Particle Event (SPE) such as solar flares and Coronal Mass Ejections (CME). The particle spectrum again includes electrons, protons, alpha particles and HZEs. Electrons possess relatively low energies [49]. For the solar protons, energy levels on the order of tens to hundreds of

MeV are often mentioned [13, 33, 34, 43, 44]. Roughly following the 11 year solar cycle, solar maximum years with a strong interplanetary magnetic field experience a reduced influx of GCR but greater solar activity. Conversely, solar minimum years see less solar activity, but a greater influx of GCR particles The influx of GCR into interplanetary space is strongly modulated by the interplanetary solar magnetic field and the and the roughly eleven year solar cycle [13, 43, 46, 47, 48, 50, 51, 52, 53].

In the NEE, the geomagnetic field in turn modulates the influx of particles from interplanetary space. This field also causes trapped particle distributions, which form the radiation belts known as Van Allen belts found around Earth [13, 43, 54]. Particle density distributions for Protons and Electrons are presented in Figure 3.2.

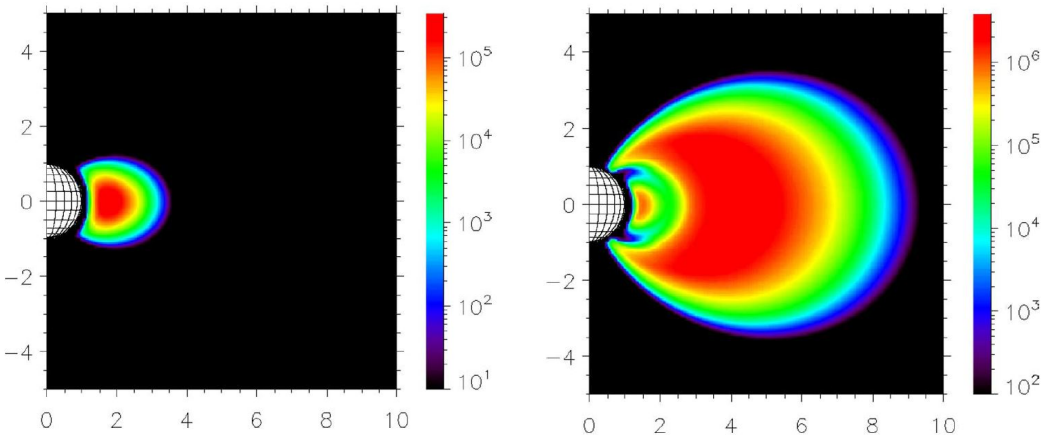


**(a)** Schematic of the omnidirectional >10 MeV proton flux determined using the AP-8 MIN model, obtained from Bourdarie and Xapsos [43].

**(b)** Schematic of the omnidirectional >1 MeV electron flux determined using the AE-8 MAX model, obtained from Bourdarie and Xapsos [43].

**Figure 3.2:** Omnidirectional particle fluxes $[cm^{-2}s^{-1}]$ in the NEE. Axes are in Earth radii.

For information on the available space radiation models or simulations, the reader is referred to [43] and [55] respectively.

### Radiation Effects

The effects different types of particle radiation have varies with both their flux and energy level. For GCR particles, the flux is relatively low [43]. However, because of their high energy they have great penetrative capabilities. Reaching into spacecraft, their ability to create highly localised damage to electronics or human cells, with potentially disastrous consequences, forms a problem. The health effects of GCR form one of the main factors prohibiting long duration manned missions [33, 43, 44, 51, 56, 57, 58, 59, 60]. PE-based materials, such as Dyneema®, form the best structural shielding against this type of radiation due to their large number of atoms per unit mass and small constituent atoms [33, 56, 57, 61].

When assessing the effects space radiation has on spacecraft materials, both for Low Earth Orbit Missions, and for interplanetary missions, proton radiation becomes interesting. In the near-Earth environment, this is due to the presence of the proton dominated inner Van Allen belt. In interplanetary space, this is due to the fact that both solar and GCR protons combine relatively high energies, when compared to electrons, with a relatively high flux, when compared to alpha particles and HZEs [43].

In polymers, ionizing radiation generally has the effect of breaking atomic bonds. Depending on how the resulting radicals react, either chain scission, crosslinking, or reconnection can occur. Chain scission and crosslinking in turn affect the molecular structure. For fibres that depend on their molecular structure and long molecules for their tensile properties, this can be detrimental. The effects of gamma [62] and electron [63, 64] radiation on the tensile properties of UHMWPE fibres have been investigated in the past. Material strength was found to decrease with increased radiation dose. The presence of oxygen during or after ageing accelerates this process [64, 65, 66]. However, no publications on the effects of proton irradiation on the tensile behaviour of UHMWPE-based fibres have been found. Ballistic testing on proton radiation aged UHMWPE-based composites have also not been reported. These data would be valuable in assessing the compatibility of Dyneema® with the space radiation environment.

## 3.6 Background Information on Impact Simulations for Orthotropic Materials

Numerical impact simulation tools, if used correctly, can form valuable contributions to both research and design projects. They can offer insights into the physical processes occurring during impact events, at time resolutions that are difficult to obtain from experiments. During design work, they can be used for preliminary sizing of structures, reducing the number of tests eventually required. Or they can serve to extrapolate known material behaviour to configurations or physical regimes where testing becomes impractical.

The process of the development for a nonlinear orthotropic hypervelocity impact material model for the Kevlar®-epoxy material used aboard the Columbus module of the ISS is presented in publications by Hayhurst et al. [67], Clegg et al. [68] and Riedel et al. [69]. The model presented in [68] will be referred to as the Kevlar Fibre Reinforced Polymer (KFRP) model from this point onwards. The model is presented in and presented in Table A.4 in Appendix A. Wicklein et al. [70] used a comparable approach to create a hypervelocity impact model for CFRP.

Impact modelling in UHMWPE-based composites has recently been spearheaded in Grujicic et al. [71], Chocron et al. [72], Lässig et al. [8] and Nguyen et al. [15]. Grujicic et al. [72] proposed a multi-scale model where processes on the fibre-matrix interface behaviour were taken into account. Chocron et al. [72] went a step larger, and modelled their composite material by lumping individual fibres and their surrounding matrix into

discrete strips with element and matrix properties. With increased levels of detail also come increased computational costs. Lässig et al. performed extensive material [8] and shock wave response [17] and implemented these data into a model where the material was represented using homogeneous Lagrangian elements with orthotropic properties. Nguyen et al. [15, 73] subsequently noted that a side-effect of the use of these orthotropic elements, was that relatively low through-thickness tensile strength values caused premature material failure and artificially reduced the through-thickness shear strength of the material. This problem was addressed by disabling through-thickness failure of the material and replacing the strain-based erosion model with an in-plane damage-based erosion model. This corresponds to the way in which projectile deceleration occurs in ballistic impacts, as described in Section 3.2.

Both models presented by Lässig et al. [8, 17] and Nguyen et al. [15, 73] use Lagrangian elements for discretisation. An inherent limitation of element-based formulations for impacts is that they depend on the artificial erosion of excessively deformed elements for their stability, constituting a removal of energy and matter. Moreover, the need for shared nodes between elements prohibits the fragmentation of impactor and target at impacts in the hypervelocity range. Therefore, simulation of impacts in spacecraft structures sometimes use SPH discretisation, as seen in the orthotropic material for the KFRP [68, 69] and CFRP [70] models mentioned above. The ability to capture damage propagation behaviour is why this thesis aims to extend the available Dyneema modelling capabilities available to SHP based simulations.

## 3.7 Literature Review Conclusions

Dyneema® is a fibre made from UHMWPE. High degrees of molecular orientation and crystallinity cause loads to be carried by intra-molecular bonds, resulting in very high specific strength and stiffness values. These material properties subsequently translate into very good ballistic protection properties, as long as membrane behaviour is allowed and impact velocities are in the ballistic velocity range. If impact velocities enter the hypervelocity impact range, shock wave phenomena become increasingly important, which can be captured using Hugoniot equations and Equations Of State.

For space applications, the Stuffed Whipple Shield is a shielding configuration, which offers high protection for low volume usage. Use of ballistic materials, such as Dyneema® would be most suitable to the stuffing layer in this configuration. For the outer bumper, a denser material is recommended from a ballistic protection point of view. Depending on the mission profile, the compatibility of several factors from the space environment require further attention. For use in regions where AO is present, such as in Low Earth Orbit (LEO), further comparative analysis of strength retention with Kevlar® is required, and an assessment of the accessibility of AO to the Stuffing layer should be made. Thermal analysis based on various mission profiles spacecraft configurations should yield representative temperature ranges for the stuffing layer. Elevated temperatures are known to cause strength and stiffness loss in UHWMPE fibres. However no

data on space representative testing were found. Vacuum thermal ageing and thermal cycling tests are recommended to assess property retention of Dyneema® fibres under those circumstances. Proton radiation ageing experiments should be performed to assess compatibility with the space radiation environment.

Numerical simulation of hypervelocity impacts is possible using hydrocode computer models. For composite materials intended for spacecraft, SPH discretisation is the recommend modelling approach. For Dyneema-based composites, so far, only finite element-based approaches have been used.

# Chapter 4

# Numerical Model Components

In this chapter, the outline of the numerical modelling tools used for this project, and their implications are presented. This is separated from the presentation of the eventual proposed numerical material models for the Dyneema® HB26 ballistic composite, which will follow in Chapter 7. The reason for this separation is that fundamental understanding of the material model is key to explaining challenges encountered in this project, and the steps taken throughout it. Note that capitalisation of letters is often used in this chapter (and subsequent chapters) to indicate specific material sub models. Examples are the Material Stress model which is a specific failure model, rather than a generic model for material stress or the Maximum velocity setting rather than a generic maximum velocity).

## 4.1 Orthotropic Material Modelling Components

In this Section, the material model components used for the modelling of composite materials are presented. The use of these models is not limited to the material models presented and proposed in this report. They are also used by Clegg et al. [68], Riedel et al. [69], Wicklein et al. [70], Lässig et al. [8] and Nguyen et al. [15]. This discussion also covers the main reasons for choosing to use ANSYS® Autodyn® as software for this project, as presented in Subsection 4.1.1.

### 4.1.1 Stress-Strain Model

For most conventional hydrocodes volumetric and deviatoric stress tensor components are separated, as done in Equation 4-1 [7]. In this Equation $s_{ij}$ is the deviatoric component of the stress tensor, whilst $p$ is the hydrostatic pressure, forming the volumetric component. This allows for independent treatment of the thermodynamic and load carrying behaviour of the material.

$$\sigma_{ij} = s_{ij} - p\delta_{ij} \tag{4-1}$$

For anisotropic materials, though, this is not accurate. Different stiffnesses in different material directions, as illustrated in Equation 4-2, mean hydrostatic pressures do not result in uniform strains.

$$\begin{bmatrix}\sigma_{11}\\ \sigma_{22}\\ \sigma_{33}\\ \sigma_{23}\\ \sigma_{31}\\ \sigma_{12}\end{bmatrix} = \begin{bmatrix}C_{11} & C_{12} & C_{13} & 0 & 0 & 0\\ C_{12} & C_{22} & C_{23} & 0 & 0 & 0\\ C_{13} & C_{23} & C_{33} & 0 & 0 & 0\\ 0 & 0 & 0 & C_{44} & 0 & 0\\ 0 & 0 & 0 & 0 & C_{55} & 0\\ 0 & 0 & 0 & 0 & 0 & C_{66}\end{bmatrix} \begin{bmatrix}\varepsilon_{11}\\ \varepsilon_{22}\\ \varepsilon_{33}\\ 2\varepsilon_{23}\\ 2\varepsilon_{31}\\ 2\varepsilon_{12}\end{bmatrix} \tag{4-2}$$

Hydrostatic stresses influence deviatoric strain components and the other way around. One way to address this matter was put forward by Anderson et al. [74]. In this paper it was proposed to separate the total strain tensor into a deviatoric and volumetric component. The volumetric component is determined based on the average of the normal strains and the deviatoric strain vector is set to be the difference between the total and volumetric strain tensor.

$$\varepsilon^{vol} = \frac{V}{V_0} - 1 = \frac{\rho_0}{\rho} - 1 \tag{4-3}$$

$$\varepsilon_{ij}^{dev} = \varepsilon_{ij} - \frac{1}{3}\varepsilon^{vol}\delta_{ij} \tag{4-4}$$

$$\begin{bmatrix}\varepsilon_{11}\\ \varepsilon_{22}\\ \varepsilon_{33}\\ 2\varepsilon_{23}\\ 2\varepsilon_{31}\\ 2\varepsilon_{12}\end{bmatrix} = \begin{bmatrix}\varepsilon_{11}^{dev} + \frac{1}{3}\varepsilon^{vol}\\ \varepsilon_{22}^{dev} + \frac{1}{3}\varepsilon^{vol}\\ \varepsilon_{33}^{dev} + \frac{1}{3}\varepsilon^{vol}\\ 2\varepsilon_{23}\\ 2\varepsilon_{31}\\ 2\varepsilon_{12}\end{bmatrix} \tag{4-5}$$

Let material pressure $p$ be defined as presented in Equation 4-6.

$$p = -\frac{1}{3}(\sigma_{11} + \sigma_{22} + \sigma_{33}) \tag{4-6}$$

Substituting the strain vector as defined in Equation 4-5 into Equation 4-2 and inserting the obtained normal stresses into Equation 4-6 yields Equation 4-7.

$$\begin{aligned} p = &-\frac{1}{9}(C_{11} + C_{22} + C_{33} + 2C_{12} + 2C_{23} + 2C_{31})\varepsilon^{vol} \\ &-\frac{1}{3}((C_{11} + C_{12} + C_{31})\varepsilon_{11}^{dev} + (C_{22} + C_{12} + C_{23})\varepsilon_{22}^{dev} + (C_{33} + C_{23} + C_{31})\varepsilon_{33}^{dev}) \end{aligned} \tag{4-7}$$

The material pressure state is therefore effectively separated into a volumetric pressure term, and a deviatoric term dependent on the material deformation. Replacing the volumetric pressure term by a pressure value as obtained from an EOS, results in Equation 4-8.

$$\begin{aligned} p = &-p(\varepsilon^{vol}, e) \\ &-\frac{1}{3}((C_{11}+C_{12}+C_{31})\varepsilon_{11}^{dev} + (C_{22}+C_{12}+C_{23})\varepsilon_{22}^{dev} + (C_{33}+C_{23}+C_{31})\varepsilon_{33}^{dev}) \end{aligned} \tag{4-8}$$

This coupling of the volumetric shock response and deviatoric strain contributions is implemented in ANSYS® Autodyn®. The author is not aware of other commercially available software packages that have this same feature. The importance of shock wave behaviour to hypervelocity impact simulations drove software selection in the early stages of the project, following the example set by other authors [8, 15, 68, 70]. Hence the choice for ANSYS® Autodyn® as the simulation tool for this project.

### 4.1.2 Equation of State

As explained in Subsection 4.1.1, the coupling of the EOS with the stress-strain model is of paramount importance to the modelling of hypervelocity impacts in composite materials. Though this coupling is implemented in ANSYS® Autodyn®, this has only been done for the Mie-Grüneisen EOS. The available formulations are the Shock and Polynomial types presented in Section 3.3.

### 4.1.3 Strength Models

Two distinct strength models have been used in this work. The first is the Orthotropic Yield criterion proposed by Chen et al. [75] and the second is the Von Mises yield criterion.

#### Orthotropic Yield Criterion

Chen et al. [75] proposed a yield model that can be used to capture non-linear, irreversible hardening of orthotropic materials. The model consists of a yield surface related to the local stress state as presented in Equation 4-9.

$$\begin{aligned} f(\sigma_{ij}) = &\, a_{11}\sigma_{11}^2 + a_{22}\sigma_{22}^2 + a_{33}\sigma_{33}^2 \\ &+ 2a_{12}\sigma_{11}\sigma_{22} + 2a_{23}\sigma_{22}\sigma_{33} + 2a_{31}\sigma_{33}\sigma_{11} \\ &+ a_{44}\sigma_{23}^2 + a_{55}\sigma_{31}^2 + a_{66}\sigma_{12}^2 = k \end{aligned} \tag{4-9}$$

The $\sigma$ terms are the stresses in the main material directions and $k$ is the current yield surface. By replacing $k$ with a ten point piecewise linear master effective stress ($\bar{\sigma}$) plastic strain ($\bar{\varepsilon}^p$) curve, hardening can be captured. The various $a$ terms define the hardening behaviour in the different material directions. This is done by setting the individual $a$ parameters such that they map a desired reference stress-plastic strain curve for their corresponding stress value onto the master effective stress-plastic strain curve. In normal direction, this mapping is performed using Equation 4-10. For shear data, Equation 4-11 is used.

$$\bar{\sigma} = \sigma_{ii}\sqrt{\frac{3a_{ii}}{2}} \quad \bar{\varepsilon}^p = \varepsilon^p_{ii}\sqrt{\frac{2}{3a_{ii}}} \tag{4-10}$$

$$\bar{\sigma} = \sigma_{ij}\sqrt{3a_{ij}} \quad \bar{\varepsilon}^p = \varepsilon^p_{ij}\sqrt{\frac{1}{3a_{ij}}} \tag{4-11}$$

The desired reference curves generally consist of experimental data. If one chooses to base the $\bar{\sigma}$-$\bar{\varepsilon}^p$ curve on one such set of reference data, the corresponding $a$ parameter can be set to 1. Through manipulation of the shape of the $\bar{\sigma}$-$\bar{\varepsilon}^p$ curve and the various $a$ parameters, this model allows for some degree of control over the yielding behaviour in all individual normal and shear directions. How well the various resulting simulated stress-strain curves match with their reference data sets, depends on how well one can match the $\bar{\sigma}$-$\bar{\varepsilon}^p$ curve to the various input datasets. Behaviour such as softening, for example, cannot be captured, since Autodyn® requires the master curve to consist of ten monotonically increasing stress and strain values.

Because of the nature of the model, it is required that the $a$ parameters cause Equation 4-9 to create a real, closed surface. To ensure this, three constraints are checked by Autodyn®. First, the condition defined in Equation 4-12 must hold. Second, the determinant from Matrix $E$ degined in Equation 4-12 must be smaller than zero. Third, all non-zero eigenvalues of Matrix $e$, defined in Equation 4-14 are required to have the same sign.

$$a_{11},\ a_{22},\ a_{33},\ a_{44},\ a_{55},\ a_{66} > 0 \tag{4-12}$$

$$E = \begin{bmatrix} a_{11} & a_{12} & a_{13} & 0 \\ a_{12} & a_{22} & a_{23} & 0 \\ a_{13} & a_{23} & a_{33} & 0 \\ 0 & 0 & 0 & -k \end{bmatrix} \tag{4-13}$$

$$e = \begin{bmatrix} a_{11} & a_{12} & a_{13} \\ a_{12} & a_{22} & a_{23} \\ a_{13} & a_{23} & a_{33} \end{bmatrix} \tag{4-14}$$

### Von Mises Criterion

The Von Mises yield criterion is used whenever the Orthotropic Yield criterion cannot be used. This is either when the effects of simplifying the Orthotropic Yield criterion itself is investigated, or when the effect of simplifying the Orthotropic softening failure model is investigated.

In the former case this is because the Ortho EOS setting can only be used in combination with either the Elastic, Von Mises or Orthotropic Yield criterion. For the latter, this is required because the Orthotropic Yield criterion cannot be used with other failure models than the Orthotropic softening model.

### 4.1.4 Failure Models

Two district failure models have been used in this work. The first is the Orthotropic Softening criterion. The second is the Material Stress model.

#### Orthotropic Softening Model

In the Orthotropic Softening model, as more elaborately explained in [76], failure is initiated at the general combined stress criterion presented in Equation 4-15. One such boundary exists for all three main direction ($ii$ is 11, 22 and 33).

$$e_{ii,f} = \left(\frac{\sigma_{ii}}{S_{ii}(1-D_{ii})}\right)^2 + \left(\frac{\sigma_{ij}}{S_{ij}(1-D_{ij})}\right)^2 + \left(\frac{\sigma_{ik}}{S_{ik}(1-D_{ik})}\right)^2 \geq 1 \quad for\ i,j,k = 1,2,3 \tag{4-15}$$

In this equation $S$ are the respective ultimate stress values. The damage parameters ($D$) vary from 0 to 1 and are determined by Equation 4-16.

$$D_{ij} = \frac{LS_{ij}\varepsilon^{cr}}{2G_{ij}} \quad for\ i,j,k = 1,2,3 \tag{4-16}$$

In Equation 4-16 $L$ is the characteristic cell dimension, $\varepsilon^{cr}$ is the crack strain and $G_{ij}$ is the relevant fracture toughness. So failure is initiated once a stress reaches its corresponding ultimate value and complete once a certain $D$ parameter reaches 1. The values of $D$ are updated every time step, denoted as $n$. Coupling of damage creation in different directions is enabled through Equation 4-17 and controlled by the damage coupling coefficient $C$, which can be set to a value between 0 and 1.

$$D_{ij}^{n+1} = D_{ij}^{n} + \Delta D_{ij}^{n} + C(D_{ik}^{n} + D_{il}^{n}) \quad for\ i,j = 1,2,3\ k,l = 1,2,3 \neq j \tag{4-17}$$

#### Material Stress Model

In the Material Stress model, failure is initiated as soon as any of the principal material stresses exceeds its allocated ultimate value [14]. Post failure options can be set to either Isotropic or Orthotropic. Under the Isotropic setting, failed material will only be able to carry bulk compressive stresses. Under the Orthotropic setting, various combinations for combined failure can be selected. All individual failure directions have the option to cause bulk failure. For failure in normal directions ($ii$), failure can also be either limited to the $ii$ direction, or can cause failure in the $ij$ or $ik$ shear directions. For failure in shear directions, the only other options are to have it cause failure in one of the three normal directions.

## 4.2 Isotropic Material Modelling Components

In this Section, the material sub-models used for the modelling of metallic components are presented.

### 4.2.1 Equation of State

For all metallic materials, the shock formulation of the Mie-Grüneisen EOS is used. This choice is made because Autodyn® has quite an extensive material library and all considered aluminium alloys had this EOS implemented.

### 4.2.2 Strength Model

For all metallic materials, Steinberg-Guinan strength models are used. The reason for this choice is twofold. First, all considered aluminium alloys from the Autodyn® material library have this model implemented. Second, the Steinberg-Guinan strength model is very suitable to high strain rates [7, 77]. It considers that for metals, at high strain rates of $\dot{\varepsilon} > 10^5\ s^{-1}$, material response becomes strain rate independent. With typical hypervelocity impact problems involving strain rates on the order of $\dot{\varepsilon} > 10^6\ s^{-1}$, this model holds validity. This is in contrast to observations with the Johnson-Cook model, whose logarithmic strain rate dependence causes problems at rates of $\dot{\varepsilon} > 10^4\ s^{-1}$ [7].

### 4.2.3 Failure Model

As failure model, a minimum hydrostatic tension model is used. This simple model follows the condition presented in Equation 4-18. If the tensile stress in the material, caused by reflected shock waves, becomes too large, material failure occurs [7].

$$p \leq p_{min} \tag{4-18}$$

A model such as the Grady Spall model could have also been applied for this purpose. This was decided against for two reasons. First, Leus et al. [78] compared Autodyn® simulations using both the Hydrostatic Pressure and Grady Spall failure modelling explosive fragmentation in Al 6061-T6 and found the Hydrostatic pressure model yielded a better match in fragment mass distribution predictions. This is only a single case study, and should not be taken as a rule. However, a second reason to opt for the Hydrostatic Pressure is a comparatively simple model. The Grady Spall model computes the local spall strength for every time step, which uses computational resources [77]. Therefore the simpler Hydrostatic Pressure failure model was selected.

## 4.3 Smoothed Particle Hydrodynamics Discretisation

As mentioned in Chapter 3, an inherent limitation of element-based impact simulations is the dependence on a material grid. This dependence has two main drawbacks when simulating impacts in the hypervelocity regime. First, the need for shared nodes in the geometric description prevents models from accurately capturing disintegration processes. Elements can generally only become separated from their bulk geometry when all surrounding elements have been eroded away. This introduces the second limitation. Hypervelocity impacts tend to bring about significant local deformations in a structure. The elements comprising this structure will, as a consequence, become severely deformed. To prevent computational problems, these deformed elements are removed through erosion. This removes mass, and thus momentum and energy from the system. These two factors, mean that for hypervelocity impact simulations, a mesh free discretisation method is preferred. One such method is geometry discretisation using Smoothed Particle Hydrodynamics.

When using smoothed particle hydrodynamics, an object is discretized into individual interpolation points, known as particles. Material properties at the location of these integration points are determined based on summation of contributions of all $n$ neighbouring particles according to Equation 4-19.

$$f(\mathbf{x}) = \sum_{i=1}^{n} f(\mathbf{x}_i) W(|\mathbf{x} - \mathbf{x}_i|) \frac{m_i}{\rho_i} \tag{4-19}$$

The weighting function ($W$) determines the controls the influence neighbouring particles have on the current interpolation point. Several types of weighting functions are available. In Autodyn® the cubic B spline is used. The value of the weighting function is in turn determined based on the distance between the current point and the neighbouring particle with index $i$. This distance is normalised based on the smoothing length $h$. The support domain of a weighting function is generally defined as an integral multiple of $h$ (usually $2h$). Outside this radius, $W$ is set to 0. Autodyn® places nodes at $1h$ from each other during model creation. This is generally referred to as the particle size. Smoothing length and particle size are therefore used interchangeably in this report.

The SPH method does have difficulties of its own. A common problem is that of tensile instabilities. This problem manifests itself in small perturbations resulting in excessive scattering and cluttering of particles. Swegle et al. [79] formulated the condition in Equation 4-20 for instability. Note that the instability can also arise under compression, when condition 4-20 is met. So the phenomenon was found to be independent of artificial viscosity, but rather caused by the shape of the weighting function and local stress state. Another consequence of the limited support domain, is that particles can escape the sphere of influence of their neighbouring particles. For a more detailed explanation of the theory behind SPH discretisation, the reader is referred to [7, 80, 81].

$$W''\sigma > 0 \tag{4-20}$$

## 4.4 2D Axial Symmetric Simulations

Autodyn® offers several different options for symmetry considerations. The first subdivision is that into Autodyn-3D and Autodyn-2D.

In Autodyn-3D, one can choose to model the complete structure as a 3D model, without symmetry considerations. A 3D model can also be generated with up to three mutually perpendicular planes of symmetry.

Autodyn-2D offers two distinct settings: planar and axial symmetry. For planar symmetry, the 2D geometry sketch generated in the $xy$-plane will be extrapolated into the plane perpendicular the sketch plane. For axial geometry, the 2D geometry sketch generated in the $xy$-plane will be rotated around the $x$-axis.

The planar symmetry setting will be used in this project for the IFPI experiments, as will be detailed in Subsection 7.1.3. For SPH-based impact simulations, axial geometry will be assumed, as also seen in [68]. The reason for this is simple. The Ansys® Autodyn® R16.2 Academic version used for this project, generated a warning at the moment more than $500,000$ particles were generated. Assume two planes of symmetry for a target plate with 200 $mm$ x 200 $mm$ in-plane dimensions, and a depth of about 15 $mm$ [8], and a particle diameter of about 0.25 $mm$ [68]. Filling only the quarter target plate will already require $9,600,000$ particles. Attempting to proceed caused the Graphical User Interface to crash on several occasions. For 3D calculations, either significant computational resources, or more elaborate discretisation will be required. Combinations of Lagrangian elements with SPH particles, as illustrated by Wicklein et al. [70] could be used for this purpose. This was, however, deemed beyond the scope of this thesis.

Note that for all impact simulation results presented in this report, cross sections of the debris could are presented. Material originating from the target plate and impactor can therefore be distinguished. This is in contrast to experimental footage for HVI into Dyneema® targets presented in this report, which are always side views of total debris clouds. For single target impact simulations, the target will always be represented using blue particles, whilst the impactor is represented using green particles. Legends are provided in every image, but may be illegible because of their size, which is not scalable in Autodyn®.

## 4.5 Reference Frames and Boundary Conditions

For all numerical simulations, the $x$-, $y$- and $z$-directions will be used to indicate the global simulation reference frame. The 1-, 2- and 3-directions will be used to indicate the material reference frame. The through-thickness direction of the laminate is defined as 11. For 3D simulations, this corresponds to the $z$-direction in the global reference frame. For 2D simulations, the 11 direction corresponds to the global $x$-direction. For all figures in this report, the impact direction is from left to right, which constitutes a positive $x$-velocity.

The following point will be reiterated later, but for clarity it will also be explicitly expressed here. Unless explicitly stated otherwise, all composite targets were modelled with a boundary condition preventing movement in impact direction along the outer most region of particles. All other directions were left unconstrained to capture target slip. For metallic targets, the constraint prevented movement in all directions since target plate slip were found.

For all impacts into composite target models, the impactor diameter was kept at 6.0 $mm$. To suppress excessive spallation for SPH based simulations of composite materials, the Maximum velocity was set to approximately 1.5 times the impactor velocity used for that case. This artificially limited the maximum velocity nodes could achieve during simulations, which prevented unbound energy growth in individual particles. For the simpler aluminium on aluminium impact cases, it was found this was not necessary.

# Chapter 5

# Metal Component Model Validation and Particle Density Refinement

In this chapter, simulation of hypervelocity impacts of aluminium impactors into aluminium plates is covered. This analysis serves two purposes. First, Aluminium bumpers are used as outer and inner bumper in SWS like the one used on the Columbus module of the ISS. They will therefore also be used in the simulation in Chapter 12. Second, modelling of metallic structures, in general, is more straight forward than the modelling of equivalent processes in composite materials. Autodyn® also has a sizeable material library, including various aluminium alloys. Therefore modelling impacts in aluminium structures, using existing material models, using SPH discretisation, was considered a good starting point.

## 5.1 Aluminium Models

In the Columbus module, the outer bumper is 2.5 $mm$ thick Al 6061-T6 and the inner bumper is 4.8 $mm$ Al 2219-T851 [82]. ESA guidelines state that for conversion between damage and impactor diameter in the NEE, an average density of 2.8 $g \cdot cm^{-3}$ should be assumed [20], which corresponds to aluminium. Hence the role of aluminium as a common impactor material used for HVI experiments [21, 24, 29, 83].

Impact experiments of aluminium spheres into aluminium plates performed by Piekutowski [83] are used as validation material in this chapter. In this study Al 2017-T4 impactors of various size were used to impact target plates of different alloys, though most were Al 6061-T6, at various velocities. It was observed that target plate alloy had limited influence on debris cloud velocity profile. Therefore, in this chapter, target plates are modelled as Al 6061-T6. Al 2017-T4 is not available in Autodyn®. The choice was made to use Al 2024-T4 for impactors. Since both alloys are of the Al 20XX series, and both have the T4 temper, this was the closest available alternative.

For simulations in Dyneema® and Kevlar® in subsequent chapters, Al 1100-O impactors are used, in line Lässig et al. [8]. For SWS simulations in Chapter 12, Al 6061-T6 was used for the outer bumper. Absent an available model for Al 2219-T851, Al 2024-T4 was used to model the inner wall. Impactors were modelled using Al 1100-O.

All aluminium models provided by Autodyn® contained a Mie-Grüneisen EOS with Shock sub-type and a Steinberg Guinan strength model. Default material strength models were not provided and had to be manually implemented.

## 5.2 Spall Strength Sensitivity

In this section, the scatter and strain rate dependence of spall strength values found in literature are discussed. Model sensitivity to spall strength variation is also investigated.

### 5.2.1 Strain Rate Dependence

As discussed in Subsection 4.2.3, the hydrostatic pressure failure criterion was implemented. The spall strength, though, is strain rate dependent [84, 85]. Ek and Asay [84] reported a value of 1.22 $GPa$ at a rate of $0.31 \cdot 10^6$ $s^{-1}$. However, achievable experimental strain rates are limited.

Grady [85] proposed a strain rate dependent spall strength model, with either brittle or ductile failure regimes based on the strain rate. Looking at the validation case Grady presents for Al 6061-T6 (including the data from Ek and Asay [84]), it can be seen his model systematically over-predicts experimental data. By representing this curve on a log-log scale the extent of the mismatch was somewhat masked.

Hayhurst et al. [67] used the model proposed by Grady, and settles on fixed strength values for hypervelocity impact simulations of 1.0 $GPa$ for Al 1100, 2.5 $GPa$ for Al 2024 and 2.6 $GPa$ for Al 6061. Because of the reported overestimation of the Grady model, a sensitivity study into the used spall strength value was performed in this project.

### 5.2.2 Strength Variation

In his experiments Piekutowski [83] used various combinations of impactor diameters and velocities, and target plate materials and thicknesses. From the subsequent debris cloud, he analysed the internal structure, and presented normalised axial ($x$-direction) and diametric ($y$-direction) velocity components for the points defined in Figure 5.1. In this work, radial velocity will be used, which is half the diametric velocity reported by Piekutowski [83].

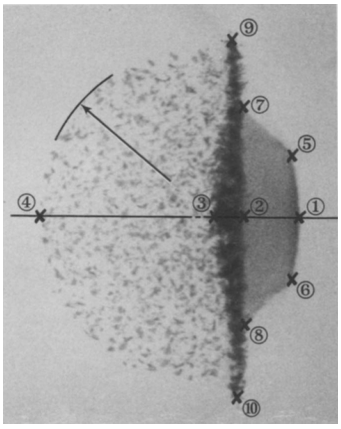


**Figure 5.1:** Numbering of debris cloud features used for velocity profile analysis [83].

Impact experiments from Piekutowski [83] were simulated using 9.53 $mm$ diameter impactors and plates with 0.8 $mm$ and 2.225 $mm$ thickness. These thicknesses were chosen because they represent the configuration with the most complex internal debris cloud geometry and and the plate thickness closest to that of the Columbus module from the available dataset [83]. Four sets of strength values were used. The first three used 1.0 $GPa$, 1.5 $GPa$, 2.0 $GPa$ for both Al 2024-T4 and Al 6061-T6. The fourth used 2.5 GPa for Al 2024-T4 and 2.6 $GPa$ for Al 6061-T6, in line with Hayhurst et al. [67]. Absent reported in-plane dimensions of the target plates, a size of 200 $mm$ x 200 $mm$ was assumed.

This strength variation study was performed in parallel with the particle density refinement study. To account for this, the choice was made to use very fine particle distributions. Resolutions of 20 and 22 particles through the thickness were selected for the 0.8 $mm$ and 2.225 $mm$ targets, resulting in smoothing lengths of 0.016 and 0.1 $mm$ respectively, which is significantly finer than the 0.25 $mm$ used by Clegg et al. [68]. Absent reports of slipping of the target plates during impact, the boundary conditions were set to prevent the top row of particles in the target plate in both $x$- and $y$-direction to simulate plate clamping. Impact velocities were set at 6.68 $km/s$ and 6.64 $km/s$ respectively, and normalisation was performed with respect to an impactor velocity of 6.7 $km/s$ as done by Piekutowski [83]. Simulation results for the 1.0 $GPa$ and 2.5/2.6 $GPa$ strength settings are presented side-by-side with experimental validation footage from Piekutowski [83] for the the 0.8 $mm$ and 2.225 $mm$ sheet thickness cases in Figure 5.2 and 5.3 respectively.

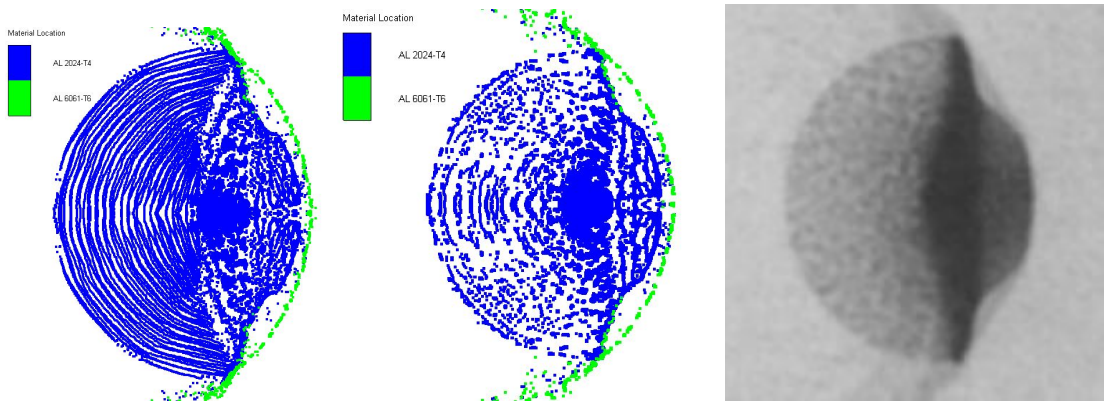


**(a)** $P_{min} = 1.0\ GPa$. **(b)** $P_{min} = 2.5/2.6\ GPa$. **(c)** Experimental [83].

**Figure 5.2:** Simulated debris clouds for different material strength values at approximately $t = 6.5 \cdot 10^{-3}\ ms$ and experimental validation footage [83] at approximately 4 cm post-impact using a 0.800 $mm$ thick target plate.

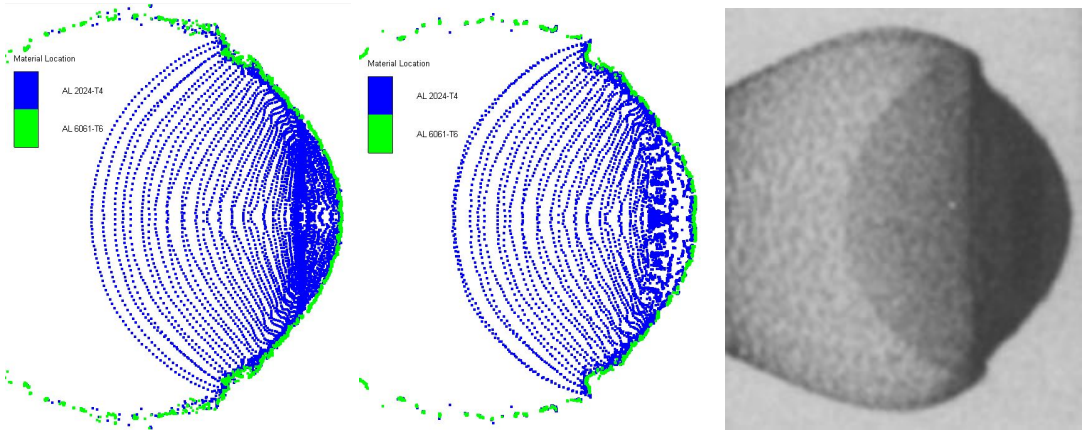


**(a)** $P_{min} = 1.0\ GPa$. **(b)** $P_{min} = 2.5/2.6\ GPa$. **(c)** Experimental [83].

**Figure 5.3:** Simulated debris clouds for different material strength values at approximately $t = 7.5 \cdot 10^{-3}\ ms$ and experimental validation footage [83] at approximately $4$ cm post-impact using a $2.225\ mm$ thick target plate.

Table 5.1 and 5.2 present the resulting normalised velocity components. Simulated velocity components were rounded off to their nearest multiple of 50 $m/s$. The $\Delta$ term represents the maximal difference between different parts of the dataset. The subscript $I$ denotes the internal difference between the four different sets of strength values. The subscript $E$ represents the maximal difference between the four sets of used strength values and experimental data from Piekutowski [83]. The percentage differences are given with respect to the normalisation velocity. From both Table 5.1 and 5.2 it can be seen that throughout the range of used strength values, the difference in obtained velocities is below 5%.

**Table 5.1:** Normalised axial and radial debris cloud velocity components for $9.53\ mm$ diameter impactors into $0.800\ mm$ thick target plates at $t = 6.5 \cdot 10^{-3}\ ms$ after impact for various material strength values. Velocities normalised with respect to $V_0 = 6.7\ km/s$.

| Axial | 1.0 $GPa$ | 1.5 $GPa$ | 2.0 $GPa$ | 2.5/2.6 $GPa$ | $\Delta_I$ % | Experimental | $\Delta_E$ % |
|---|---|---|---|---|---|---|---|
| Point 1 | 0.97 | 0.97 | 0.97 | 0.98 | 1 | 0.98 | 1 |
| Point 2 | 0.96 | 0.95 | 0.96 | 0.96 | 1 | 0.96 | 1 |
| Point 4 | 0.70 | 0.70 | 0.71 | 0.72 | 2 | 0.73 | 3 |
| Point 5, 6 | 0.96 | 0.95 | 0.95 | 0.96 | 1 | 0.98 | 3 |
| Point 7, 8 | 0.94 | 0.93 | 0.94 | 0.93 | 1 | 0.96 | 3 |
| Point 9, 10 | 0.93 | 0.92 | 0.93 | 0.93 | 1 | 0.92 | 1 |
| Radial | 1.0 $GPa$ | 1.5 $GPa$ | 2.0 $GPa$ | 2.5/2.6 $GPa$ | $\Delta_I$ % | Experimental | $\Delta_E$ % |
| Point 5, 6 | 0.07 | 0.07 | 0.07 | 0.07 | 0 | 0.05 | 2 |
| Point 7, 8 | 0.08 | 0.08 | 0.08 | 0.08 | 0 | 0.07 | 1 |
| Point 9, 10 | 0.19 | 0.18 | 0.17 | 0.16 | 3 | 0.18 | 2 |

**Table 5.2:** Normalised axial and radial debris cloud velocity components for $9.53\ mm$ diameter impactors into $2.225\ mm$ thick target plates at $t = 7.5 \cdot 10^{-3}\ ms$ after impact for various material strength values. Velocities normalised with respect to $V_0 = 6.7\ km/s$.

| Axial | 1.0 $GPa$ | 1.5 $GPa$ | 2.0 $GPa$ | 2.5/2.6 $GPa$ | $\Delta_I$ % | Experimental | $\Delta_E$ % |
|---|---|---|---|---|---|---|---|
| Point 1 | 0.90 | 0.90 | 0.87 | 0.87 | 2 | 0.90 | 3 |
| Point 2 | 0.90 | 0.90 | 0.90 | 0.90 | 0 | 0.89 | 1 |
| Point 4 | 0.52 | 0.53 | 0.54 | 0.54 | 2 | 0.53 | 1 |
| Point 7, 8 | 0.86 | 0.85 | 0.83 | 0.84 | 3 | 0.89 | 6 |
| Radial | 1.0 $GPa$ | 1.5 $GPa$ | 2.0 $GPa$ | 2.5/2.6 $GPa$ | $\Delta_I$ % | Experimental | $\Delta_E$ % |
| Point 7,8 | 0.09 | 0.10 | 0.12 | 0.10 | 3 | 0.04 | 8 |

Discrepancies with the experimental data are generally also below 5%, except for point 7 and 8 for the $2.225\ mm$ thick plate. This larger discrepancy for the latter case, can partially be attributed to the fact that for thick plates, the idealised debris cloud geometry becomes distorted, as can be seen by comparing Figure 5.1 and 5.3. Piekutowski therefore concludes that points 5 and 6, and 7 and 8 are no longer distinguishable. As a consequence, he provides only axial and radial velocity values for point 7 and 8. Given the distorted shape of the debris cloud for high thickness over impactor diameter ratios, compared to the idealised case, it becomes increasingly difficult to ensure the same location on the debris cloud contour is selected as used by Piekutowski [83]. Given the fact the simulated values for the axial velocity from Table 5.2 are consistently lower than the reported values, and radial velocities are consistently higher, it stands to reason Piekutowski used a point closer to the leading edge of the debris cloud than was assumed in this report. Let it also be noted that velocity data can only be extracted from particles, and that these particles have to be manually selected in Autodyn®. Reading errors, or variations in velocity vectors belonging to neighbouring particles also contribute to simulation scatter.

Lower strength values mostly manifest themselves in the form of more finely distributed debris clouds. Zooming in on the courser clouds belonging to higher modelling strengths, shows this clumping together is caused by groups of un-failed material, keeping groups of failed particles together. Since the distribution of the debris cloud is not affected by different strength values, the strength properties proposed by Hayhurst et al. [67] can be used for 2024-T4, Al 6061-T6 and Al 1100-O. The low scatter in debris cloud velocity components observed under variation of the material strength, is also supported by the observation by Swift and Hopkins [19], reported in Subsection 3.4.1, that the effectiveness and fragmentation behaviour of bumper shields is not dominated by material strength.

## 5.3 Particle Density Refinement Study

To determine minimum particle density requirements for simulation of aluminium outer bumper shields and impactors, a particle density refinements study was performed. Fol-

lowing the argumentation from Subsection 5.2.2, the 0.8 and 2.225 bumper thickness configurations are used, and strength values are set to 2.5 $GPa$ for Al 2024-T4 and 2.6 $GPa$ for Al 6061-T6.

For the 0.8 $mm$ thick target configuration, smoothing lengths of 0.4 $mm$, 0.2 $mm$, 0.16 $mm$, 0.1 $mm$, 0.08 $mm$ and 0.05 $mm$ are used. For the 2.225 $mm$ thick target configuration, smoothing lengths of 0.5 $mm$, 0.2 $mm$, 0.1 $mm$, 0.075 $mm$ and 0.05 $mm$ are used. Impact velocities were again set at 6.68 $km/s$ and 6.64 $km/s$ respectively, and normalisation was performed with respect to an impactor velocity of 6.7 $km/s$ [83]. Simulation results for various smoothing lengths are presented side-by-side for the the 0.8 $mm$ and 2.225 $mm$ sheet thickness cases in Figure 5.4 and 5.5 respectively.

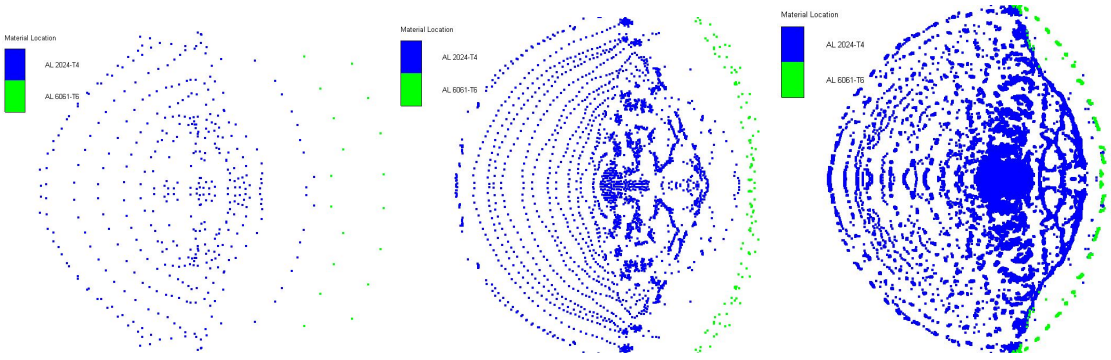


**(a)** $h = 0.4\ mm.$ **(b)** $h = 0.16\ mm.$ **(c)** $h = 0.05\ mm.$

**Figure 5.4:** Simulated debris clouds for various smoothing length values $t = 6.5 \cdot 10^{-3}\ ms$ post-impact using a $0.800\ mm$ thick target plate.

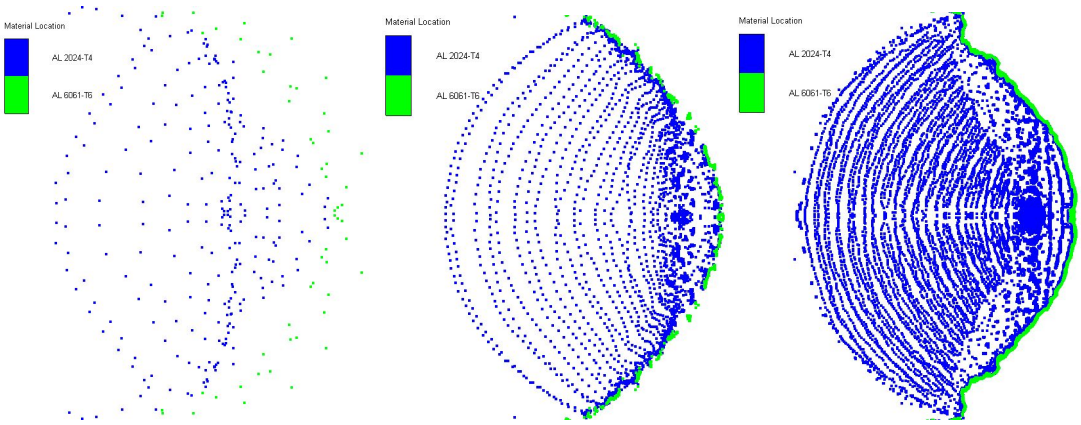


**(a)** $h = 0.5\ mm.$ **(b)** $h = 0.15\ mm.$ **(c)** $h = 0.05\ mm.$

**Figure 5.5:** Simulated debris clouds for various smoothing length values $t = 7.5 \cdot 10^{-3}\ ms$ post-impact using a $2.225\ mm$ thick target plate.

**Table 5.3:** Normalised axial and radial debris cloud velocity components for $9.53\ mm$ diameter impactors into $0.800\ mm$ target plates at $t = 6.5{\cdot}10^{-3}\ ms$ after impact for various particle smoothing length values. Velocities normalised with respect to $V_0 = 6.7\ km/s$.

| Axial | $h = 0.4\ mm$ | $h = 0.2\ mm$ | $h = 0.16\ mm$ | $h = 0.1\ mm$ | h=0.05 $mm$ | Experimental |
|---|---|---|---|---|---|---|
| Point 1 | 0.97 | 0.97 | 0.98 | 0.97 | 0.98 | 0.98 |
| Point 2 | 0.96 | 0.96 | 0.95 | 0.95 | 0.96 | 0.96 |
| Point 4 | 0.76 | 0.75 | 0.75 | 0.73 | 0.72 | 0.73 |
| Point 5, 6 | 0.98 | 0.97 | 0.97 | 0.95 | 0.96 | 0.98 |
| Point 7,8 | 0.94 | 0.96 | 0.95 | 0.93 | 0.94 | 0.96 |
| Point 9, 10 | 0.92 | 0.94 | 0.93 | 0.93 | 0.93 | 0.92 |
| Radial | h=0.4 $mm$ | h=0.2 $mm$ | h=0.16 $mm$ | h=0.1 $mm$ | h=0.05 $mm$ | Experimental |
| Point 5, 6 | 0.01 | 0.02 | 0.05 | 0.07 | 0.07 | 0.05 |
| Point 7,8 | 0.06 | 0.04 | 0.07 | 0.09 | 0.08 | 0.07 |
| Point 9, 10 | 0.17 | 0.16 | 0.17 | 0.17 | 0.17 | 0.18 |

**Table 5.4:** Normalised axial and radial debris cloud velocity components for $9.53\ mm$ diameter impactors into $2.225\ mm$ target plates at $t = 7.5{\cdot}10^{-3}\ ms$ after impact for various particle smoothing length values. Velocities normalised with respect to $V_0 = 6.7\ km/s$.

| Axial | $h = 0.5\ mm$ | $h = 0.2\ mm$ | $h = 0.15\ mm$ | $h = 0.1\ mm$ | h=0.05 $mm$ | Experimental |
|---|---|---|---|---|---|---|
| Point 1 | 0.96 | 0.90 | 0.90 | 0.87 | 0.89 | 0.90 |
| Point 2 | 0.87 | 0.90 | 0.88 | 0.90 | 0.90 | 0.89 |
| Point 4 | 0.63 | 0.57 | 0.55 | 0.54 | 0.52 | 0.53 |
| Point 7, 8 | 0.85 | 0.87 | 0.86 | 0.85 | 0.84 | 0.89 |
| Radial | h=0.5 $mm$ | h=0.2 $mm$ | h=0.15 $mm$ | h=0.1 $mm$ | h=0.05 $mm$ | Experimental |
| Point 7, 8 | 0.10 | 0.10 | 0.09 | 0.10 | 0.11 | 0.04 |

In Figure 5.4 and 5.5, it can be seen that over the full considered ranges the rough shape of the internal structure of the debris cloud is represented quite well. From Table 5.3 it can be observed that for all used smoothing length values the axial velocity components of the debris cloud agree with experimental values within a margin of 4% of the reference impact velocity. For the radial velocity, the relatively large discrepancy between experimental and simulated components at point 5 and 6 can be seen to last up to a smoothing length of $0.16\ mm$. From Table 5.4, it can be observed that discrepancies in the axial residual velocity of point 1 and 4 have dropped to within a 5% margin starting from a smoothing length of $0.2\ mm$. The discrepancy between the simulated and experimental radial velocity of point 7 and 8 appears to be particle size independent and is explained in the same way as in Subsection 5.2.2.

Note that the drawbacks of a particle based discretisation scheme mentioned in Subsection 5.2.2 become more pronounced when particle density is reduced. For very course particle distributions, obtaining the velocities at specific points in the debris cloud be-

comes difficult. The cloud features become more difficult to discern and it may well be there are fewer or no particles at or around the site of interest. As can be seen from Figure 5.4 and 5.5, the debris clouds become geometrically well defined for smoothing lengths of about 0.15 $mm$ and finer. This is mostly caused by the resolution in the impactor. The variations in normalised residual velocity values seen in both tables are partially caused by difficulties in obtaining velocity data from exact locations in the debris cloud within Autodyn®. Care was taken to extract information consistently from locations as used by Piekutowski [83]. However, lumping of nodes as illustrated in Figure 5.4b occasionally made obtaining data from the desired location impossible. Variations in velocity vectors for adjacent groups of particles also meant errors were introduced by the manual extraction process.

So reasonable approximation of the debris cloud shape encountered over the whole range of considered smoothing lengths, as illustrated in Figure 5.4 and Figure 5.5. Combining this with the provided explanation for the encountered variation in obtained residual velocity data for different smoothing lengths, it was decided tabulated data were the most appropriate way to present results. For both considered cases, the debris clouds became geometrically well defined for smoothing lengths of about 0.15 $mm$ and finer. Therefore a particle size of at most 0.15 $mm$ was set for metallic components considered throughout this project.

# Chapter 6

# Initial Dyneema® Model Formulation and Encountered Discrepancies

In this chapter, initial hypervelocity impact simulations using an existing Dyneema® HB26 material model, combined with an SPH discretisation, are presented. The discrepancies between the material response predicted by these models and those observed during experimental tests gave rise to the need to re-evaluate the used model, and identify their cause. The investigation into the root cause of the failure of the model to reproduce validation data represents a significant part of this chapter. Its conclusions signalled the need for the modification of the existing material models presented subsequent chapters, which formed the main focus of this project.

## 6.1 Validation Cases

The validation cases used in this project were those provided by the hypervelocity impact test campaign reported by Lässig et al. [8]. High speed footage from this campaign was also kindly provided by the Fraunhofer Institute for High-Speed Dynamics of the Ernst-Mach-Institut. The experimental set-up used by Lässig et al. [8] consisted of Dyneema® HB26 target samples with in-plane dimensions of 200 $mm$ x 200 $mm$ and an AD of 15 kg/m$^2$. This equates to a thickness of 15 $mm$. No thickness variation was applied. The impactor consisted of an aluminium sphere with a diameter of 6.0 $mm$, which Lässig et al. modelled using Al 1100-O. Impact velocities and residual velocities were as described in Table 6.1. During the high fragmentation impacts at 5370 $m/s$ and 6591 $m/s$, substantial disintegration of the aluminium impactor occurred, and identification of Dyneema® and aluminium fragments in the debris cloud was not possible. Therefore the residual velocity represents the peak velocity found in the resulting debris cloud.

Note that Table 6.1 indicates no repetition tests were performed for cases where penetration was observed. This means no information is available on experimental scatter for equal initial conditions.

**Table 6.1:** Experimental impact and residual velocities in $m/s$ from Lässig et al. [8].

| | | | | | | | |
|---|---|---|---|---|---|---|---|
| $V_0$ Experimental | 2052 | 2438 | 2453 | 3100 | 3532 | 5370 | 6591 |
| $V_{res}$ Experimental | 0 | 0 | 0 | 679 | 958 | 1730 | 2457 |

These experimental data were used for model validation by both Lässig et al. [8] and Nguyen et al. [15]. The work discussed in this report is a continuation of the results presented by these authors. One of the main contributions of this project is the extension of this modelling capability into the SPH discretisation realm. Where possible, values used in the latest model iteration, published by Nguyen et al. [15] are maintained.

## 6.2 Initial Model Iteration

The latest iteration of the model, published by Nguyen et al. [15], was intended for use with an element-based discretisation. One of the main features of this model is that rather than making use of a strain-based erosion criterion, a custom, in-plane damage based-criterion was used. This was done to better capture the membrane-like response of fibre based ballistic composites in the ballistic impact regime. In strain based erosion criteria, premature through-thickness failure was found to artificially reduce the effective strain value controlling the erosion initiation. To stop this failure from occurring, through-thickness strength in the Orthotropic Softening model was set to infinite and damage coupling was disabled. Erosion was initiated when either one of the in-plane damage parameters $D_{22}$ or $D_{33}$ reached 1. To make this model suitable for use in-combination with SPH discretisation, material strength in through-thickness direction had to be set in line with the spall strength of Dyneema® HB26. These data were not available. Therefore, it was decided to take the spall strength reported for KFRP of 45 $MPa$ as substitute value [68]. This assumption was also made by Grujicic et al. [86]. Note that reported spall strength can vary substantially for fibre reinforced composites, with the CFRP model by Wicklein et al. [70] using a value of 245.7 $MPa$. The damage coupling coefficient $C$ was set to a value of 0.5, in line with Lässig et al. [8]. The resulting model, using an Orthotropic Shock EOS, Orthotropic Yield failure model and Orthotropic Softening strength model, is labelled DM0, Dyneema Model (DM), and presented in Table A.1 in Appendix A.

As initial step, DM0 was used to simulate the impact cases with $V_0 = 3100\ m/s$ and $V_0 = 6591\ m/s$. These simulations were performed using axial symmetry 2D settings. The velocities were selected because they constitute the lowest velocity at which penetration was encountered and the highest available impact velocity respectively. Since at this point no mesh refinement study had been performed, a smoothing length of 0.1 $mm$, was used again. The top row of particles in the DM0 target plate were constrained using a boundary condition that prevented movement in the $x$-direction, but allowed movement in the $y$-direction, to account for slipping of the target plate in the clamps observed during experiments [8].

For both simulated cases a mismatch with experimental data was encountered. The impactor failed to penetrate, and was expelled back out of the target plate with negative velocity. This was followed by excessive spallation at the back face of the DM0 target. This is illustrated in Figure 6.1 and 6.2. From left to right, these figures present experimental footage, an overall representation of simulation results, and an enlarged detail

of the impactor site. The latter is included to further clarify the backwards expulsion of the impactor.

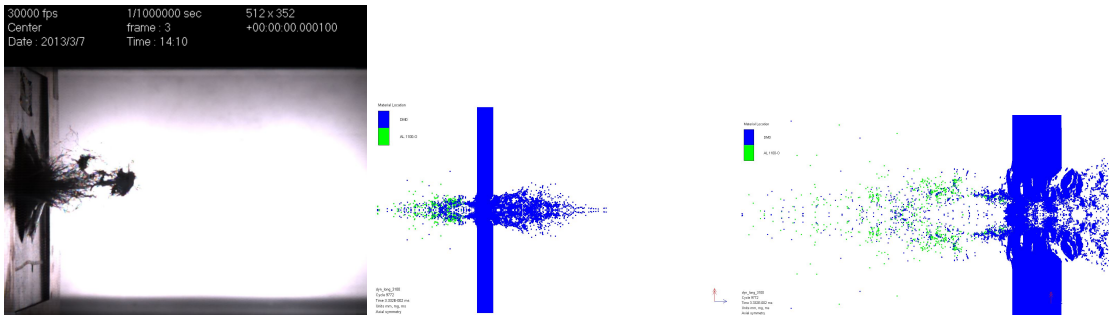


**(a)** Experimental [8]. **(b)** Simulation still-shot. **(c)** Impact site enlarged.

**Figure 6.1:** Experimental and simulated impact results from model DM0 for an impact velocity of 3100 $m/s$. Experimental footage is taken at $t = 1.0 \cdot 10^{-1}$ $ms$ after impact. Numerical data are from $t = 0.33 \cdot 10^{-1}$ $ms$ after impact.

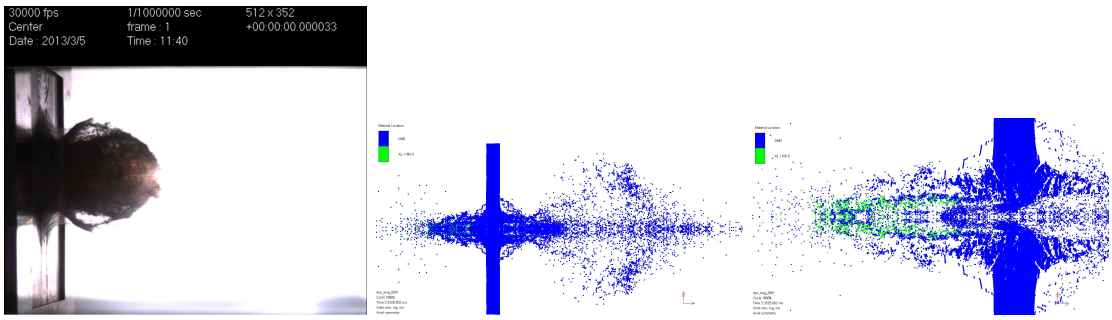


**(a)** Experimental [8]. **(b)** Simulation still-shot. **(c)** Impact site enlarged.

**Figure 6.2:** Experimental and simulated impact results from model DM0 for an impact velocity of 6591 $m/s$ at $t = 0.33 \cdot 10^{-1}$ $ms$ after impact.

For Figure 6.1, simulated and experimental data are not taken at the same time with respect to impact. Experimental footage is taken at $t = 1.0 \cdot 10^{-1}$ $ms$. At this point the debris propagation trend can be clearly seen. The impactor punched through the target plate, with relatively limited fragmentation. The simulated cloud presented is as taken at a time of $t = 0.33 \cdot 10^{-1}$ $ms$. Simulations were stopped some time after impactor reversal was observed and to preserve computational resources. At $t = 0.33 \cdot 10^{-1}$ $ms$ the impactor can already be seen to have moved back out of the target plate without penetration.

## 6.3 Identification of the Discrepancy Cause

As was described in Section 6.2, the initial simulations performed using DM0 resulted in results that did not match validation data. Several hypotheses for the observed phenomena were formulated. These were be grouped into three main categories. The cause of the discrepancy was expected to either be found in the modelling approach, the model implementation or the material model itself.

### 6.3.1 Reflection on the Modelling Approach

The first potential cause for the observed discrepancy would be in the modelling approach. This refers to the use of the Axial Symmetry modelling setting. This could cause discrepancies in two ways. First, axial rotation of the 2D model results in a circular target plate, rather than a square one. Second, numerical assumptions are made by Autodyn® during the evaluation of the 2D model.

The first hypothesis was dismissed as a likely cause for two main reasons. First, the absence of the corners of the plate were also not found to be a problem for the metallic model simulations discussed in Chapter 5. Second, 3D simulations were performed both on Lagrangian models, as will be discusses in Section 9.3, and on SPH based models. For the latter, it was attempted to simulate impacts at 3532 $m/s$, 5370 $m/s$ and 6591 $m/s$. Particle smoothing length was set to 0.25 $mm$, conform [68]. A double symmetry plane was also implemented, so only a quarter of the model had to be generated.

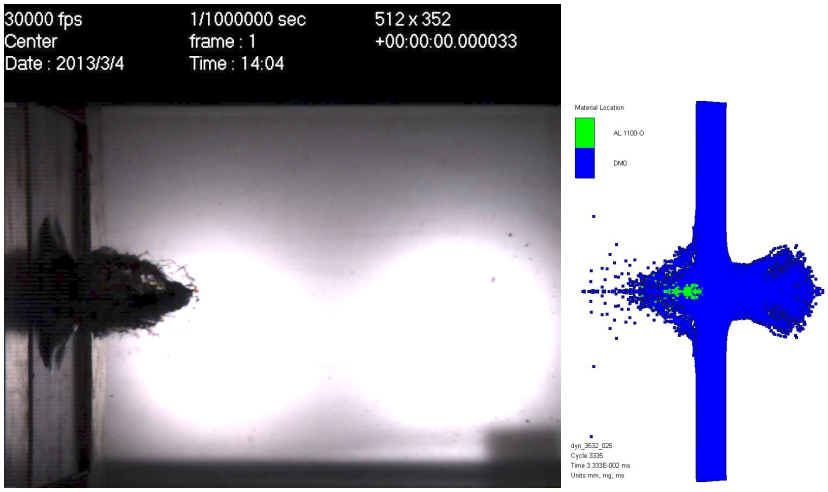


**(a)** Experimental [8]. **(b)** 3D Simulation.

**Figure 6.3:** Experimental and 3D-simulated impact results from model DM0 for an impact velocity of 3532 $m/s$ at $t = 0.33 \cdot 10^{-1}$ $ms$ after impact.

From Figure 6.3 and 6.4 (and Figure 9.16) it can be seen that the corners of the material hardly, if at al, deformed during the impact. Most deformation is, as expected, occurring

along a cross across the plane following the fibre directions. The 3D models using SPH discretisation were also found to be computationally very demanding. This manifested itself in a lagging Graphical User Interface (GUI), very long computational times, and frequent crashes. No boundary conditions were implemented, because giving the command to do so resulted in systematic crashing. 3D simulations were generally terminated after several days, by which time the in-simulation termination time of $t = 1.0 \cdot 10^{-1}\ ms$ was not yet reached. 2D simulations seldom took more than 36 hours to reach this point.

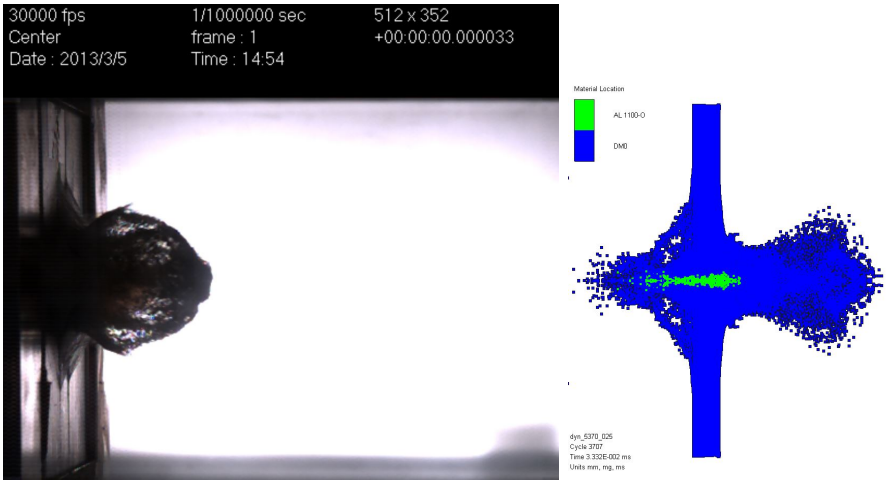


**(a)** Experimental [8]. **(b)** 3D Simulation.

**Figure 6.4:** Experimental and 3D-simulated impact results from model DM0 for an impact velocity of 5370 $m/s$ at $t = 0.33 \cdot 10^{-1}\ ms$ after impact.

The second hypothesis was dismissed as likely cause for the observed discrepancy for two reasons. First, the two completed 3D simulations using SPH discretisation, also displayed a failure to adequately capture the physical reality. It has not proven to be possible to ascertain exactly how Autodyn-2D extrapolates a 2D model to a physical impact model from either the ANSYS® Mechanical User Manual [87], Autodyn® User Manual [77] or the Autodyn® Composite Modelling manual [14]. It was, however, found that Clegg et al. [68] also used the axial symmetric model setting. Clegg is affiliated with Century Dynamics Ltd and ANSYS®, Inc. which are the companies that respectively created and own Autodyn®. Therefore, it was assumed Autodyn® 2D axial symmetry is suitable for simulation of composites under hypervelocity impact.

### 6.3.2 Reflection on the Model Implementation

The second possibility explored is that the way the model is implemented causes the observed discrepancy. With this, it is meant that the selected particle smoothing length would cause the problem. Since the used smoothing length of 0.1 $mm$, is far lower than the 0.25 $mm$, reported by Clegg et al. [68] and 0.2 $mm$, by Riedel et al. [69].

The particle resolution of 150 particles through-thickness is also far higher than the 29 particles through-thickness reported by Riedel et al. [69]. Therefore it is unlikely the mesh is too course to generate consistent results. It was, however, investigated whether the mesh was perhaps too fine, by repeating the $V_0 = 6591\ m/s$ simulation using a smoothing length of 0.20 $mm$. No notable change in perforation behaviour was observed, as demonstrated in Figure 6.5a.

Alternatively, it was considered whether target thickness might have caused part of the problem. Riedel et al. [69], for example, referred to KFRP targets with a nominal thickness of 5.7 $mm$. Converting this to an equal AD Dyneema® HB26 resulted in a target with a thickness of approximately 9.6 $mm$. Simulating a $V_0 = 6591\ m/s$ impact on a 9.6 $mm$, thick target with $h = 0.10\ mm$, also resulted in barely any perforation, with the maximal impactor debris residual velocity of around 360 $m/s$. The simulation results are presented in Figure 6.5b.

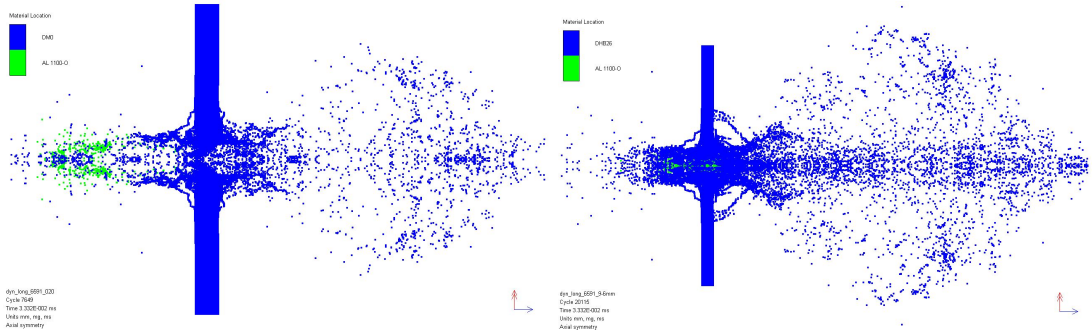

**(a)** $AD = 15\ kg/m^2$, $h = 0.2\ mm$. **(b)** $AD = 9.6\ kg/m^2$, $h = 0.1\ mm$.

**Figure 6.5:** Simulated impact results from model DM0 for an impact velocity of 6591 $m/s$ at $t = 0.33 \cdot 10^{-1}\ ms$ after impact using varying smoothing length and target thickness.

### 6.3.3 Reflection on the Material Model

With the modelling approach and model implementation considered, the most likely cause for the observed discrepancy is the material model itself. The DM0 model consists of three main components: The Orthotropic Shock EOS, Orthotropic Yield failure model and Orthotropic Softening strength model.

#### The Orthotropic Softening Strength Model

First, the influence of the Orthotropic Softening model on numerical results was assessed. Systematic variation of input parameters was performed to ascertain whether sensitivity to any particular parameter was the cause of the observed discrepancy between simulations and experiments. The following variations were used as test cases:

1. Through-thickness tensile strength was changed from 45 $MPa$ to as 1.07 $MPa$ used by Lässig et al. [8]. This value was based on low strain rate tensile testing.

2. Through-thickness shear strength (12- and 31-directions) was reduced from 575 $MPa$ to a value of 156 $MPa$, based on Split Hopkinson Bar (SHB) shear experiments by Ruiz-Ripoll et al. [88]. This latter value constitutes a dynamic loading value, whilst the former was based on an a principal-stress failure relationship between tensile strength and through-thickness shear strength [15].

3. General target strength was reduced by half. This applied to all six tensile and shear failure strength values. Additionally, the fracture energy in the three shear directions was reduced from $1.46 \cdot 10^3$ $J/m^2$ to 1.46 $J/m^2$. The former is the value as reported by Nguyen et al. [15] and Clegg et al. [68] and the latter is the value reported by Lässig et al. [8] and Grujicic et al. [86]. It may well be this difference is based on a typo, but this way, the effect of using the lower value can be included in considerations.

In addition, two other modifications in the modelling approach were considered that are included in this subsubsection for brevity. These two being:

1. Impactor strength was increased from 1.0 $GPa$ for AL 1100-O to 2.0 $GPa$.

2. Artificial viscosity was included. The default setting for the linear viscosity term was set to 2.5, which is reported to be at the extreme of the typically used range [89]. Quadratic viscosity was kept at the default setting of 1.0.

Five cases, each with one of the model perturbations described above, were simulated using an impactor velocity of 6591 $m/s$. The smoothing length was kept at 0.1 $mm$. For all these cases, it was found that the impactor did not penetrate. The impactor was expelled back out the way it came in, followed by excessive spallation of the target plate. To illustrate this, two example simulation results are presented in Figure 6.6. Figure 6.6a presents results for the case with the reduced strength and toughness values in DM0. Figure 6.6b presents results from the case with the impactor strength at $P_{min} = 2.0$ $GPa$. This set of variations indicates that the cause of the discrepancy is not the implementation of the Orthotropic Softening model.

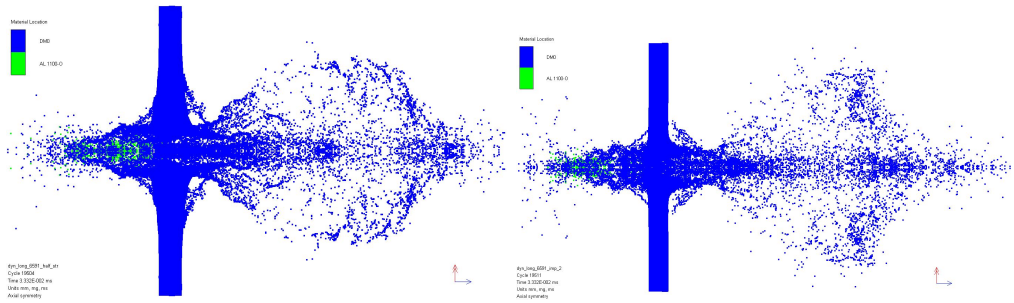

**(a)** Strength values DM0 halved. **(b)** Impactor $P_{min} = 2.0$ $GPa$.

**Figure 6.6:** Simulated impact results from model DM0 for an impact velocity of 6591 $m/s$ at $t = 0.33 \cdot 10^{-1}$ $ms$ after impact for varying target and impactor strengths.

### The Orthotropic Yield Failure Model

Second, the influence of the Orthotropic Yield model was assessed. The input for this model consists of 30 individual parameters. Therefore it was decided that individual variation of parameters was not an efficient way to characterise model response. Instead, it was decided to change the Orthotropic Yield model for a simpler model. In combination with the Orthotropic EOS, Autodyn® allows only three failure models to be used, namely the Elastic, Von Mises or Orthotropic Yield models. Therefore the Von Mises Model was selected as alternative model. Using the Orthotropic Softening model in combination with anything but the Orthotropic Yield model resulted in crashing of the simulation upon initiation, so this model also had to be replaced. The Material Stress Model is the closest available equivalent to the Orthotropic Softening model, allowing for one-to-one copying of the strength values used in DM0. Keeping post failure at the default Isotropic setting resulted in IM1, Intermediate Model (IM). This model is presented in Table A.2 in Appendix A.

Simulating an impact at $V_0 = 3100\ m/s$ and $V_0 = 6591\ m/s$ using $h = 0.15\ mm$, resulted in penetration of the plate by the impactor, as presented in Figure 6.7. Simulation of impacts at various different impact velocities yielded residual velocities as presented in Table 6.2. Systematic overestimation of residual velocities at impact velocities below 5370 $m/s$ can be observed. The results from this model variation suggest a part of the Orthotropic Yield model was causing the observed discrepancy.

**Table 6.2:** Impact and residual velocities in $m/s$ for both experimental [8] and numerical test cases using model IM1.

| $V_0$ | 2052 | 2438 | 3100 | 3532 | 5370 | 6591 |
|---|---|---|---|---|---|---|
| $V_{res}$ Experimental | 0 | 0 | 679 | 958 | 1730 | 2457 |
| $V_{res}$ IM1 | 700 | 850 | 1100 | 1250 | 1900 | 2300 |

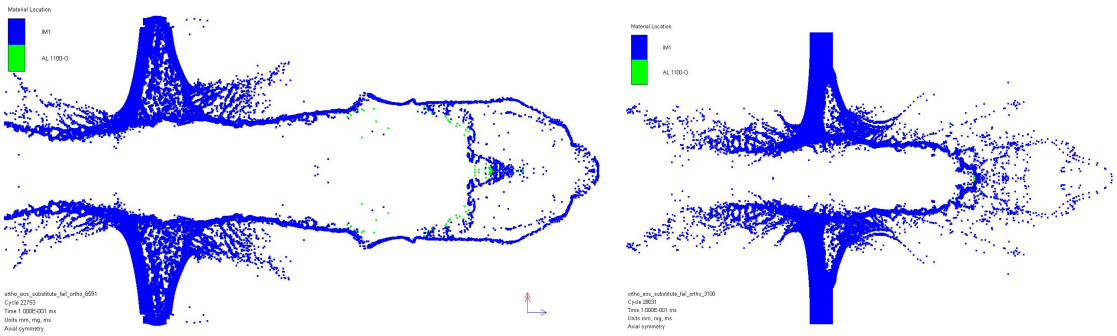

**(a)** $V_0 = 6591\ m/s$. **(b)** $V_0 = 3100\ m/s$.

**Figure 6.7:** Simulated impact results using model IM1 at $t = 1.0 \cdot 10^{-1}\ ms$ after impact.

### 6.3.4 Through-Thickness Material Response

Unit tests were simulated on DM0 unit cubes, as described in [15]. These tests are meant to verify compliance between the defined material model and material characterisation experiments that act as model input. For these tests, three-dimensional cubes were generated with unit edge lengths. These cubes were meshed using a single unstructured Lagrangian element. Depending on the loading condition tested, one of the eight corner nodes was given a pinned boundary condition ($V_x = V_y = V_z = 0\ m/s$). Three other nodes, which form one side of the unit cube in combination with the first node, are only prevented from displacing in the loading direction of the cube, to allow for Poisson contraction. The four nodes in the opposing plane are given constant unit velocity boundary conditions in the relevant loading direction to simulate sample straining.

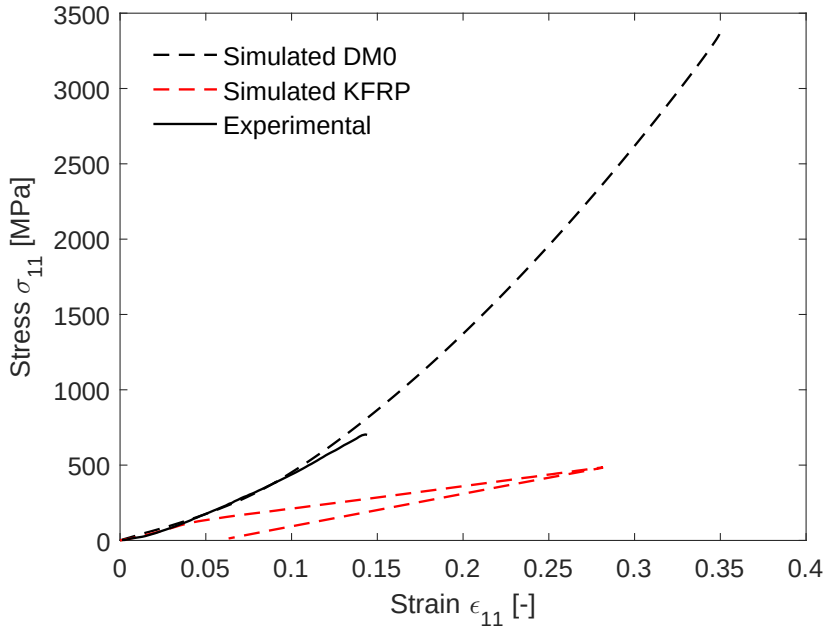


**Figure 6.8:** Comparison of through-thickness compressive unit tests on the DM0 and KFRP [68] models to experimental data from Chocron et al. [72], as used by Nguyen et al. [15].

Simulating a through-thickness unit test, it was observed that the proposed master effective stress strain curve and $a$ parameters proposed by Nguyen et al. [8] allow the model to accurately follow the used input stress-strain curve from Chocron et al. [72], as presented in Figure 6.8. However, one notable discrepancy was observed. Where the experimental curve stops at a value of approximately 700 $MPa$ [72], the numerical curve does not exhibit failure until a stress of 3.4 $GPa$. For a material model with a Lagrangian finite element formulation, this is not necessarily a problem. The Orthotropic Softening model can allow for effective failure once in-plane stresses become too large and strain-based erosion can remove elements that have become too deformed as a consequence.

For the model presented by Nguyen et al. [15] this becomes even less of a problem, since out-of-plane failure of elements has actively been disabled. However, for an SPH based formulation, this explains the observed problem of stagnation of the impactor during penetration, followed by excessive spallation at the rear of the target plate. The compressive response of the DM0 model was then compared to one from a unit test on the KFRP material model proposed by Clegg et al. [68], as presented in Figure 6.8. This model was designed for use in combination with an SPH based discretisation. The KFRP model displays a relatively low through-thickness compressive strength, when compared to the DM0 model. Therefore it was concluded that over-prediction of the through-thickness compressive strength by the Orthotropic Yield model parameter set derived by Nguyen et al. [15] is the cause of the discrepancy between the experimental data and the simulation results.

# Chapter 7

# Proposed Dyneema® Model Formulations

As discussed in Subsection 6.3.4, the through-thickness compressive material response is suspected to be the main factor preventing accurate capturing of projectile penetration in the DM0 model. A fundamental problem here is that this compressive strength cannot be numerically limited by means of a single parameter within the used Autodyn® material modelling components. The through-thickness strength defined in the material model explicitly refers to the material tensile strength. Knowing this, two solution approaches were formulated to remedy the observed discrepancy between experimental and numerical results. The first was to repair the DM0 model, keeping the same sub-models in place, but reworking the Orthotropic Yield model to produce a better fit for the through-thickness compressive data. The second was to create a model using different sub-models, that can still reflect the orthotropic character of the actual Dyneema composite, using the lessons learned from the IM1 model. Both approaches were explored and will be presented in this chapter. As naming convention, the model that will result from the former solution method will be referred to as DM1. The model resulting from the latter solution method will be referred to as DM2.

## 7.1 Formulation of DM1

For model DM1, an Orthotropic Shock EOS, Orthotropic Yield failure model and Orthotropic Softening strength model are used. In this section, the approach followed to redefine the input parameters for this model is presented and notable observations are reported.

### 7.1.1 The Orthotropic Softening Strength Model

The Orthotropic Softening model, as used by Nguyen et al. [15] is kept mostly unaltered from its implementation in DM0. Through-thickness shear strength was set to 156 $MPa$, in line with findings from Ruiz-Ripoll et al. [88]. Note that this publication has been retracted for reasons not affecting data validity. The document has been received directly from Dr. ing. Lässig [90]. It was later agreed with Dr. Nguyen [91] not to present any figures or data from the work in this report, other than reported failure stress and strain data.

Through-thickness tensile strength was set at 45 $MPa$. In-plane shear strength was set to 55 $MPa$, the reason for which will be more clearly explained in Subsection 7.1.2

### 7.1.2 The Orthotropic Yield Failure Model

Reworking the input parameters for the Orthotropic Yield model proved to be a critical step. This subsection, will focus on the eventual formulation that was proposed for use in DM1. The significant sensitivity of the model to changes in the Orthotropic Shock EOS, and to cross-coupling within different terms of the Orthotropic Yield model itself will be further discussed in Chapter 11. Values that were not specified here, are as taken from Nguyen et al. [15], with original references added for each value in Table 7.1.

#### Master Curve Formulation

As explained in Section 4.1.3, the Orthotropic Yield model requires a ten-point master effective stress versus plastic strain curve to be defined. Both Lässig et al. [8] and Nguyen et al. [15] opted to base these curves on in-plane shear test data. These data showed significant nonlinearity in their hardening behaviour. After transformation, this non-linearity is preserved in the master curve. This non-linear curve can be used to capture similar non-linearities in other material directions. A combination of the various $a$ parameters and material strengths can be used to ensure the different model responses fit input data, as demonstrated by both Lässig et al. [8] and Nguyen et al. [15].

Since no single strength parameter is available to cut the compressive stress-strain curve off at the desired value, the master curve had to be redefined. Neither Clegg et al. [68] nor Wicklein et al. [70] reported having a problem with excessive compressive strengths. Consulting these papers showed that for both, in-plane tensile data were used as input for the master curve. Following this example resulted in the curve presented in Table 7.1. The $a_{22}$ and $a_{33}$ parameters were set to 1.0. The corresponding validation unit test case is presented in Figure 7.1.

This choice of master curve immediately introduced a new problem. As can be seen from Figure 7.2, the in-plane test data used are nearly perfectly linear. As such, the non-linearities in input shear data presented in Figure 7.2 and cannot be accurately followed. Even though the Orthotropic Yield model allows for a significant degree of capturing anisotropic behaviour and coupling responses in different material directions, some kind of compromise will almost always be required. It is possible that a master curve can be defined that allows both the non-linear hardening under shear loading and timely through-thickness compressive failure to be captured. Defining such a curve was deemed beyond the scope of this project.

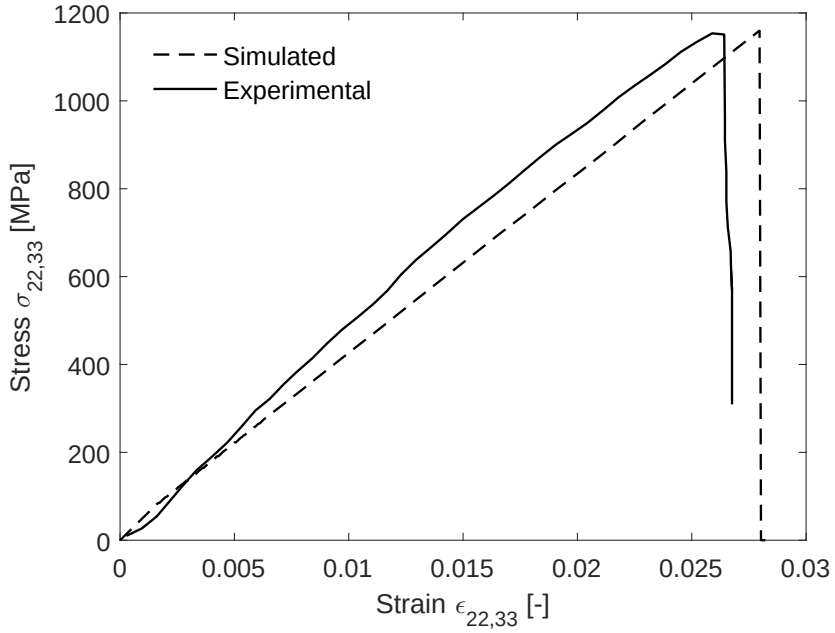


**Figure 7.1:** In-plane tensile verification unit test for DM1 using experimental data from Heisserer [92].

### In-Plane Shear Hardening Behaviour

With the master curve defined, the individual $a$ parameters were set. For in-plane shear strength, it has been observed that ultimate strength strongly depends on sample width. Lässig et al. found values ranging from 35 $MPa$ [73] to 55 $MPa$ [93] for 20 $mm$ wide samples, whilst Heisserer [92] values ranging up to 120 $MPa$ 80 $mm$ wide samples. Here the choice was made to fit the in-plane shear response of the material model to the same experimental data used by Nguyen et al. [15], taken from Lässig [93]. The Maximum Shear Stress 23 was set to 55 $MPa$, and $a_{44}$ was chosen to match the observed failure strain. The verification unit test is presented in Figure 7.2.

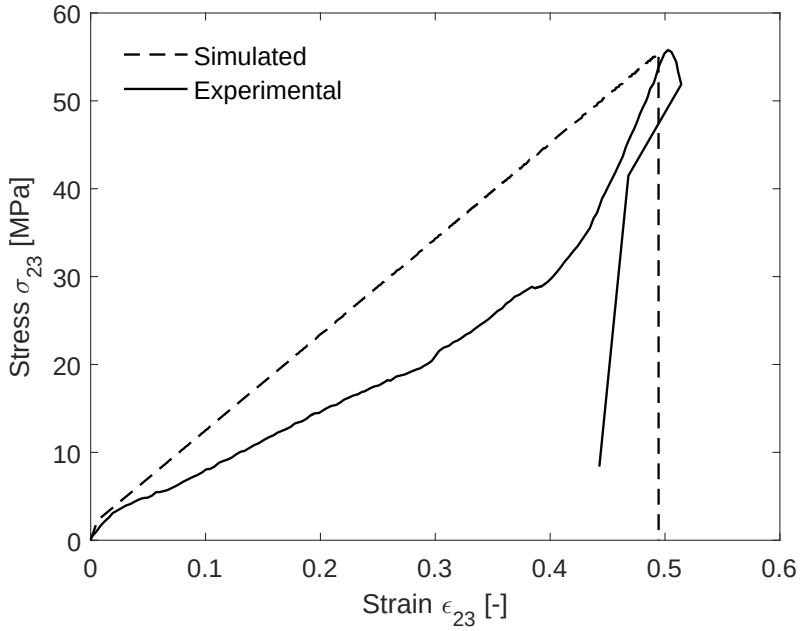


**Figure 7.2:** In-plane shear verification unit test for DM1 using experimental data from Lässig [93].

### Through-Thickness Shear Hardening Behaviour

For through-thickness shearing, the experimental shear test data provided by Lässig et al. [8] and used Nguyen et al. [15] were used. These data did not extend up to failure. Nguyen et al. [15] extrapolated the data to an expected failure point, as indicated in Figure 7.3. In this work, ultimate strain for the DM1 model was chosen to match the intersection point with the simulated curve generated using the model proposed by Nguyen et al. [15]. The $a_{55}$ and $a_{66}$ parameters were set accordingly. This is illustrated in Figure 7.3, where the ultimate strain for DM1 can be seen to occur at the intersection between the stress-strain curves for DM1 and the one generated using the model from Nguyen et al. [15]. In the unit tests used to determine the simulated material curves, Lagrangian elements were used. The maximum stress reached during these tests is limited by the used spall strength, as noted by Nguyen et al. [73]. The values for the $a_{55}$ and $a_{66}$ parameters are therefore selected using the assumption that a similar interaction holds for SPH based simulations. By varying through-thickness shear strengths in simulations, it has been observed that this assumption does not fully hold for the SPH discretisation. The effects, appear to be limited, but more investigations on this topic are needed.

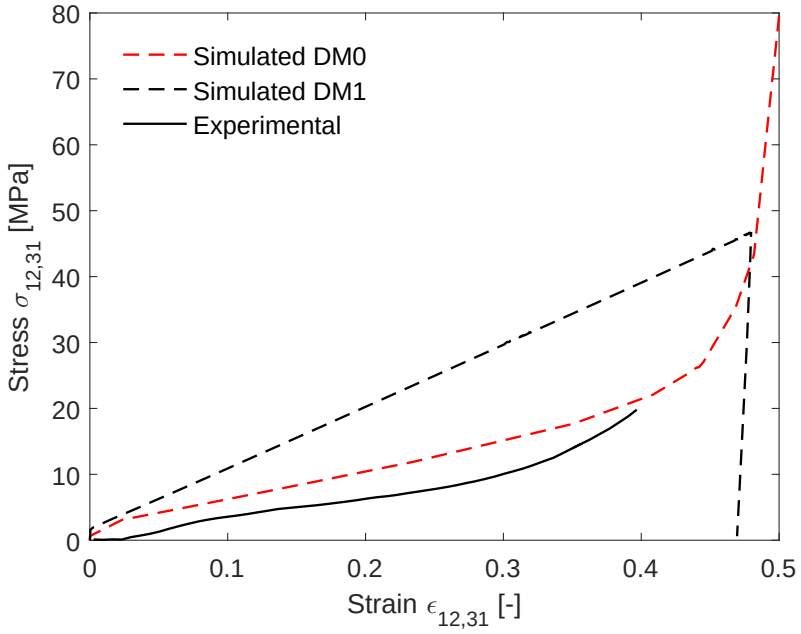


**Figure 7.3:** Through-thickness shear verification unit test for DM1 using experimental data from Lässig et al. [15].

#### Combined Loading Terms

Absent combined loading data or plastic poisson ratios, accurate determination of the $a_{12}$, $a_{23}$ and $a_{31}$ terms is not possible. They have been set to 0, in line with both Lässig et al. [8] and Nguyen et al. [15].

### 7.1.3 Through-Thickness Material Yielding and the Orthotropic Shock EOS

In this subsection the values used for the $a_{11}$ parameter of the Orthotropic Yield model and the input parameters for the Orthotropic Shock EOS are presented. The reason for this grouping is because of a coupling between these two parameters and the respective material properties they represent.

#### Input Parameters for the Orthotropic Shock EOS

The linear formulation of the Orthotropic Shock EOS, used by Nguyen et al. [15], was adopted for this work. Since Hazell et al. [16] demonstrated that the in-fibre direction shock response of UHMWPE composites are comparable to that of polyethylene, the off-Hugoniot material response were also assumed to be similar. Under this assumption, a Grüneisen coefficient of 1.64 could be adopted [94].

In its linearised form, presented in Equation 3-6, only the first $S_1$ coefficient from Equation 3-5 is used to relate the shock particle velocity to the shock wave velocity. The $S_1$ parameter has then to be set to match simulation results to those from IFPI experiments from Lässig et al. [8, 17]. The projectile was modelled in ANSYS® Autodyn® 2D with symmetry set to planar. As presented in Figure 7.4, a 5.0 $mm$ C45 steel base was joined to a 6.0 $mm$ thick UHMWPE plate, which together were fired into a 2.0 $mm$ thick C45 steel plate. The C45 steel was modelled using material parameters from Rohr et al. [95], as presented in Table A.5 in Appendix A.

Discretisation was performed using a structured mesh of Lagrangian elements. One element was used in $y$-direction, and an element size of 0.10 $mm$ was used in $x$-direction, conform [68]. A gauge point was added to the last element in the witness plate to obtain the velocity response after impact. Horizontal velocity was varied to match experimental values, as presented in Figure 7.8. Velocity in $y$-direction for the top and bottom nodes was set to 0 $m/s$ to ensure the 1D nature of the simulation. This 1D assumption is valid, as long as stress waves from the side edges of the plates have not reached the centre of the plate. As Nguyen [96] argued, this is expected to occur at about 3400 $ns$ for the composite material and 4150 $ns$ after impact for the C45 steel components.

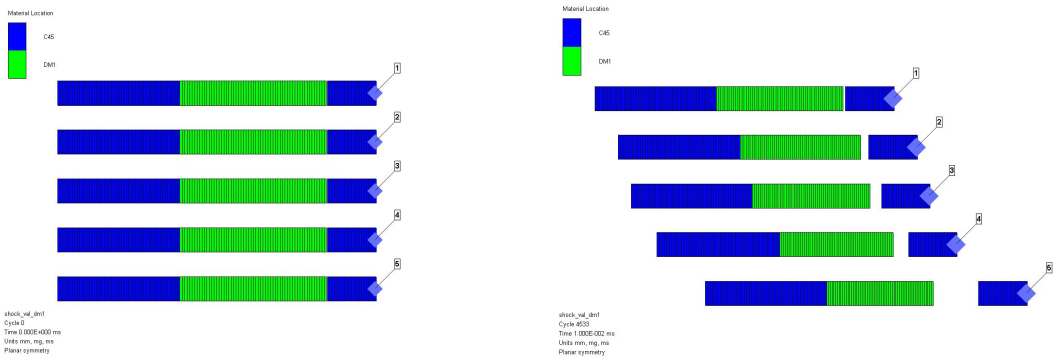

**(a)** Pre-impact condition. **(b)** Post-impact condition.

**Figure 7.4:** Illustration of the unit test approach used for IFPI tests and shock wave verification. Gauge points are indicated by the purple rhombi at the right-hand side of each subfigure.

### Through-Thickness Hardening Behaviour

The $a_{11}$ parameter is used to capture the yielding behaviour of the material in through-thickness direction. As an initial iteration, the $S_1$ value from the EOS was kept at the value of 1.3 used by Nguyen et al. [15]. The $a_{11}$ parameter was set to a value of 22, to match validation data from Chocron et al. [72], as used by Nguyen et al. [15]. Simulations using $h = 0.1$ $mm$ and impact velocities ranging from 3100 $m/s$ to 6591 $m/s$ indicated penetration was still not successfully captured under these conditions. When comparing the elevated hydrostatic pressure data taken from Chocron et al. [72] to dynamic SHB data from Shaker et al. [97], it can be seen that the SHB data cover a

far wider strain range. The $a_{11}$ parameter was then set to 70 to match the dynamic test data from Shaker et al. [97]. Repeating the simulations using $h = 0.1\ mm$ and impact velocities ranging from 3100 $m/s$ to 6591 $m/s$ indicated penetration was again not successfully captured.

Simulating flyer plate experiments using this latest iteration of the material model revealed that by increasing the $a_{11}$ parameter, shock wave propagation behaviour had begun to diverge from experimental data. This drop in observed rear face velocity in simulated IFPI experiments could be remedied by increasing the $S_1$ parameter. However, increasing the $S_1$ parameter, in turn, was found to effectively reduce the value of $a_{11}$ by increasing the slope of the through-thickness compressive stress-strain curve. The effect of changing $a_{11}$ on the through-thickness shock wave behaviour and of changing $S_1$ on the through-thickness compressive response is presented in Figure 7.5 and 7.6.

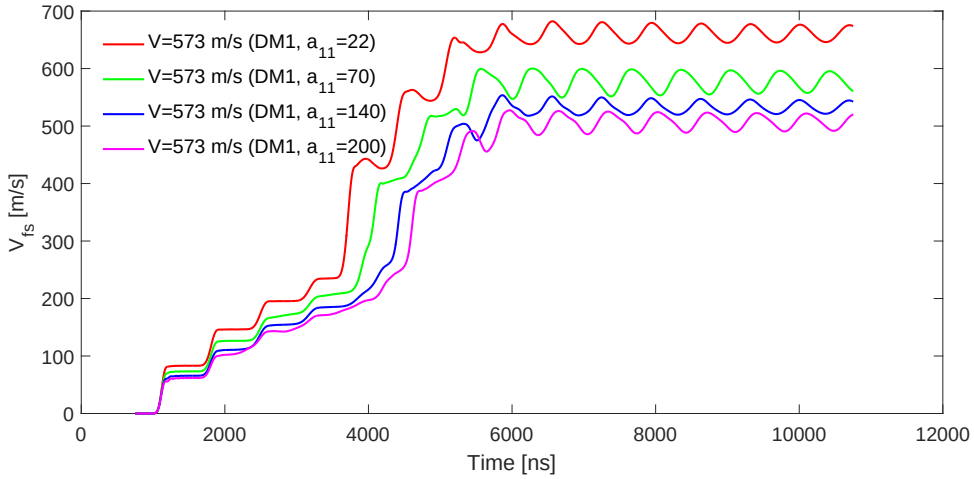


**Figure 7.5:** Effect of varying $a_{11}$ on IFPI unit test model response for DM1.

Iterative modification of the model resulted in a parameter combination of $a_{11} = 140$ and $S_1 = 2.3$. The resulting through-thickness compressive verification curve and shock-wave propagation curve are presented in Figure 7.7 and 7.8 respectively. Using this parameter combination resulted in improved model performance. This model was labelled DM1. Simulation results are presented in Chapter 9.

Figure 7.7 shows that combining the newly defined master effective stress versus plastic strain curve, results in a through-thickness compression material response that follows data from Shaker et al. [97] up to the point where the simulated curve predicts failure. The peak stress observed by Shaker et al. [97] was not reproduced for the considered value of $a_{11}$. Varying $a_{11}$ would affect the slope of the numerically generated curve, as well as the achieved peak stress. With the current master effective stress versus plastic strain curve it is not possible to perfectly match validation data for this case. Formulating a master effective stress versus plastic strain curve that would allow for a

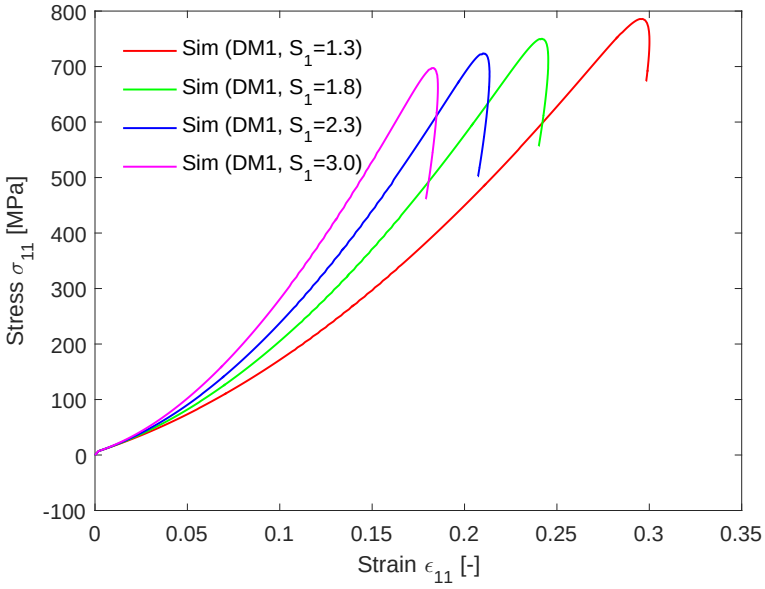


**Figure 7.6:** Effect of varying $S_1$ on through-thickness compressive response for DM1.

match in both slope and maximum stress was found to be challenging. The reason for this is the sensitivity of the model through-thickness compressive response to parameters other than $a_{11}$, as was illustrated in this section for variations in the $S_1$ parameter.

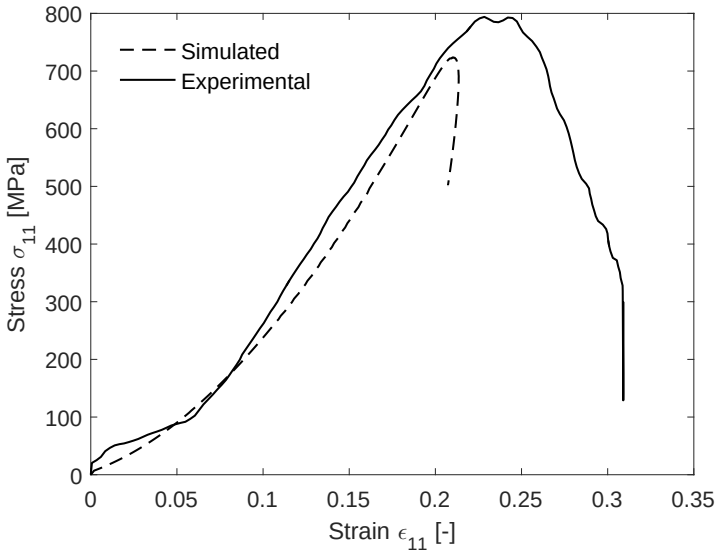


**Figure 7.7:** Through-thickness compressive verification unit test for DM1 using experimental data from Shaker et al. [97].

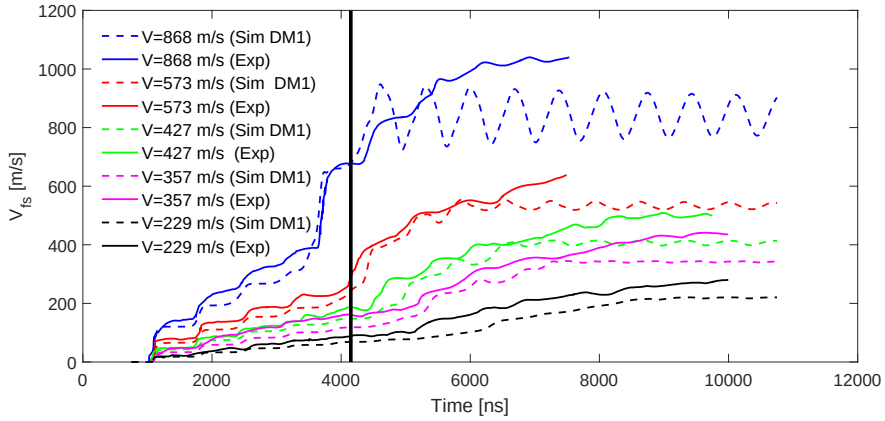


**Figure 7.8:** IFPI free surface velocity verification unit tests using DM1 and experimental data from Lässig et al. [8]. The vertical line represent the 3400 $ns$ after impact mark.

Figure 7.8 illustrates the match between simulated and validation data for the IFPI test data taken from Lässig et al. [73]. The closeness of the fit varies for the different considered impact velocities. In general, it can be seen that time-wise prediction of shock wave reflections is captured well. For the 868 $m/s$ and 573 $m/s$ plate velocity cases, for example, it can be seen four velocity platforms are formed before the large velocity jump located around 4500 $ns$. The time points at which the jumps between platforms occur are also predicted well. This match of predicted event times tends to decrease from approximately 3400 $ns$ after impact which corresponds to the expected point at which the 1D assumption ceases to be valid for the experiment.

The match in rear face velocity was found to be less good. Overall, an under prediction of rear face velocities is encountered. Mismatches of up to approximately 25% of the experimental value were encountered. Divergence at later simulation times should, again, be contributed to the fact the 1D assumption no longer held for the experimental cases. Rear face velocities for key rear face velocity platforms, such as the first platform and the platform after the large jump, were found to be represented quite well. Overall lifting of the curves by varying the $S_1$ parameter is possible, but this was found to result in a shift of the curves to the right, resulting in the disappearance of velocity plateaus.

The overall under-prediction of shock wave velocities means that in simulations, information propagation under-predicted with respect to reality. The recommended solution approach for the observed discrepancy is to attempt a more extensive formulation of the Orthotropic EOS. This could be achieved by adding additional $S$ terms for the shock formulation currently used, or switching to the polynomial formulation.

### 7.1.4 DM1 Parameters

The modelling steps described in the current section have resulted in a combination of parameters for DM1 as described in Table 7.1.

**Table 7.1:** Input parameters for the DM1 material model.

| Parameter | Value | Unit | Source | Parameter | Value | Unit | Source |
|---|---|---|---|---|---|---|---|
| EOS: Orthotropic | | | | Strength: Orthotropic yield | | | |
| Reference Density | 0.98 | $g/cm^3$ | [98] | Plasticity constant 11 | 140 | – | Fit to [97] |
| Young's modulus 11 | $3.62 \cdot 10^6$ | $kPa$ | [8] | Plasticity constant 22 | 1.0 | – | Based on [92] |
| Young's modulus 22 | $5.11 \cdot 10^7$ | $kPa$ | [92] | Plasticity constant 33 | 1.0 | – | Based on [92] |
| Young's modulus 33 | $5.11 \cdot 10^7$ | $kPa$ | [92] | Plasticity constant 12 | 0 | – | - |
| Poisson's Ratio 12 | 0.013 | – | [8] | Plasticity constant 23 | 0 | – | - |
| Poisson's Ratio 23 | 0 | – | [8] | Plasticity constant 31 | 0 | – | - |
| Poisson's Ratio 31 | 0.5 | – | [8] | Plasticity constant 44 | 700 | – | Fit to [93] |
| Shear modulus 12 | $2.0 \cdot 10^6$ | $kPa$ | [15] | Plasticity constant 55 | 1100 | – | Fit to [15] |
| Shear modulus 23 | $1.92 \cdot 10^5$ | $kPa$ | [15] | Plasticity constant 66 | 1100 | – | Fit to [15] |
| Shear modulus 31 | $2.0 \cdot 10^6$ | $kPa$ | [15] | Eff. Stress #1 | $1.71 \cdot 10^5$ | $kPa$ | Based on [92] |
| | | | | Eff. Stress #2 | $3.09 \cdot 10^5$ | $kPa$ | Based on [92] |
| Volumetric Response: Shock | | | | Eff. Stress #3 | $4.46 \cdot 10^5$ | $kPa$ | Based on [92] |
| Grüneisen coefficient | 1.64 | – | [94] | Eff. Stress #4 | $5.84 \cdot 10^5$ | $kPa$ | Based on [92] |
| Parameter C1 | $3.57 \cdot 10^3$ | $m/s$ | - | Eff. Stress #5 | $7.21 \cdot 10^5$ | $kPa$ | Based on [92] |
| Parameter S1 | 2.3 | – | Match to [8] | Eff. Stress #6 | $8.59 \cdot 10^5$ | $kPa$ | Based on [92] |
| Reference Temperature | 293 | $K$ | - | Eff. Stress #7 | $9.96 \cdot 10^5$ | $kPa$ | Based on [92] |
| Specific Heat | $1.85 \cdot 10^3$ | $J/kgK$ | [98] | Eff. Stress #8 | $1.13 \cdot 10^6$ | $kPa$ | Based on [92] |
| | | | | Eff. Stress #9 | $1.27 \cdot 10^6$ | $kPa$ | Based on [92] |
| Failure: Orthotropic softening | | | | Eff. Stress #10 | $1.41 \cdot 10^6$ | $kPa$ | Based on [92] |
| Tensile failure stress 11 | $4.50 \cdot 10^4$ | $kPa$ | [68] | Eff. Plastic Strain #1 | 0.00021 | – | Based on [92] |
| Tensile failure stress 22 | $1.15 \cdot 10^6$ | $kPa$ | [92] | Eff. Plastic Strain #2 | 0.00064 | – | Based on [92] |
| Tensile failure stress 33 | $1.15 \cdot 10^6$ | $kPa$ | [92] | Eff. Plastic Strain #3 | 0.00107 | – | Based on [92] |
| Maximum shear stress 12 | $1.56 \cdot 10^5$ | $kPa$ | [88] | Eff. Plastic Strain #4 | 0.00150 | – | Based on [92] |
| Maximum shear stress 23 | $5.50 \cdot 10^4$ | $kPa$ | [93] | Eff. Plastic Strain #5 | 0.00193 | – | Based on [92] |
| Maximum shear stress 31 | $1.56 \cdot 10^5$ | $kPa$ | [88] | Eff. Plastic Strain #6 | 0.00236 | – | Based on [92] |
| Fracture energy 11 | 790 | $J/m^2$ | [8] | Eff. Plastic Strain #7 | 0.00279 | – | Based on [92] |
| Fracture energy 22 | 30 | $J/m^2$ | [68] | Eff. Plastic Strain #8 | 0.00322 | – | Based on [92] |
| Fracture energy 33 | 30 | $J/m^2$ | [68] | Eff. Plastic Strain #9 | 0.00365 | – | Based on [92] |
| Fracture energy 12 | $1.46 \cdot 10^3$ | $J/m^2$ | [68] | Eff. Plastic Strain #10 | 0.00408 | – | Based on [92] |
| Fracture energy 23 | $1.46 \cdot 10^3$ | $J/m^2$ | [68] | | | | |
| Fracture energy 31 | $1.46 \cdot 10^3$ | $J/m^2$ | [68] | | | | |
| Damage coupling coefficient | 0.50 | – | [8] | | | | |

## 7.2 Formulation of DM2

For model DM2, an Orthotropic Shock EOS, Von Mises failure model and Material Stress strength model are used. This model was formulated on the observed success from the IM1 model. The problem of over-prediction of residual velocity at lower impact velocities for the IM1, as reported in Subsection 6.3.3, has been addressed by exploring the Orthotropic post-failure options available in the Material Stress strength model.

### 7.2.1 Von Mises Yield Failure Model

The Von Mises Failure model was used to capture material failure. In the DM2 model. Since the loading mode is in the through-thickness direction, the shear modulus used is the through-thickness shear modulus proposed by Nguyen et al. [15]. The yield strength used is based on the through-thickness shear stress at which initial non-linearity is reported by Ruiz-Ripoll et al. [88]. Validation unit tests for this case are limited to in-plane tensile and through-thickness compression tests. This is because Autodyn® did not allow the necessary material rotations to be implemented in the material model required for shear unit testing.

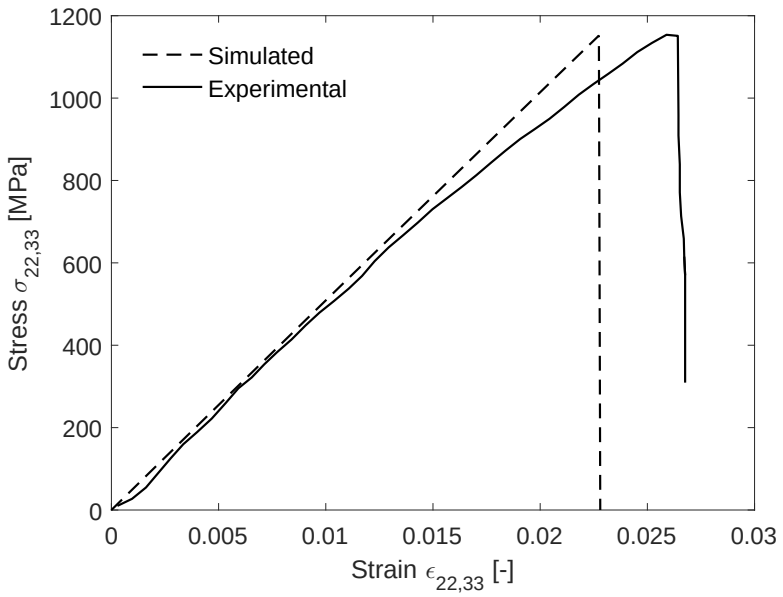


**Figure 7.9:** In-plane tensile unit test for DM2 using experimental data from Heisserer [92].

Unit tests for in-plane and through-thickness tensile tests are presented in Figure 7.9 and 7.10. In Figure 7.9 it can be seen that the fit resulting from in-plane tensile testing is less than was obtained for DM1. This is caused by the decreased measure of control one has over the post failure material behaviour using the Von Mises yield criterion as opposed to the Orthotropic Yield criterion. Surprising were the results obtained from the

through-thickness compressive material testing. In Figure 7.10 it can be clearly seen the simulated through-thickness compressive response does not follow the data from Shaker et al. [97]. If anything, the material response appears to be in line with that observed for DM0 and presented in Figure 6.8. The very response that was hypothesised to be the root cause of the issues observed for DM0.

Simulation results for both DM1 and DM2, and the comparison of these results to validation data are presented in Chapter 9. Considering the improvement in model behaviour presented there, as compared to the behaviour observed for DM0 in Chapter 6, means the hypothesis that the discrepancies originated from the Orthotropic Yield model is probably still correct.

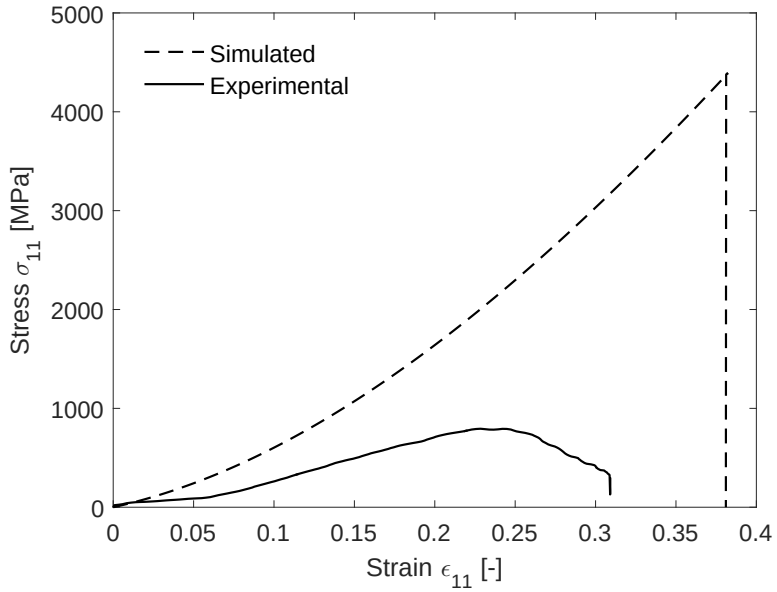


**Figure 7.10:** Through-thickness compressive unit test for DM2 using experimental data from Shaker et al. [97].

As was discussed in Subsection 6.3.3, it was not possible to independently test the model response to disabling either the Orthotropic Yield or the Orthotropic Softening model in DM0. Therefore, it stands to reason that complex parts of the post failure response resulting from the combination between the Orthotropic Yield or the Orthotropic Softening model were not fully covered in Chapter 6. This explanation is further supported by examining the unit test cubes for the DM0 and DM2 models. Figure 7.11 presents a side-view of 3D unit test cubes, where compression took place in vertical direction. The first cube, presented in Figure 7.11a, was modelled using DM0. The cube modelled using DM2 is presented in Figure 7.11b. It can clearly be seen that the DM0 cube still retained a hexagonal shape at the end of the simulation, whereas for the DM2 model the unit cube was fully flattened.

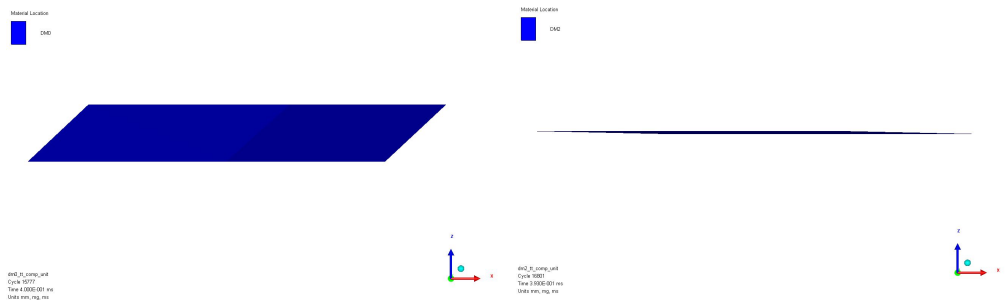

**(a)** DM0 unit test cube. **(b)** DM2 unit test cube.

**Figure 7.11:** Post-loading through-thickness unit test cubes for DM0 and DM2 models.

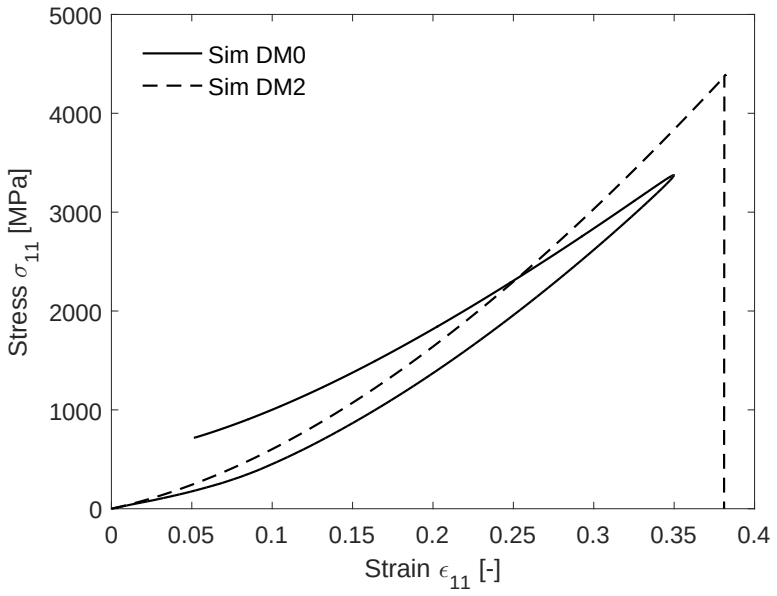


**Figure 7.12:** Comparison of through-thickness compressive unit test results obtained from DM0 and DM2.

Further comparing the through-thickness compressive responses of DM0 and DM2, as presented in Figure 7.12, another notable difference was observed. For DM2, failure causes the stress-strain curve to drop straight down. So failure causes full loss of material strength for DM2. For DM0, though, the stress strain curve does not move down after the ultimate stress is reached. It instead starts moving backwards. So for a given material strain, encountered material stresses are higher after ultimate conditions were reached, than they were before.

The hypothesis for the observed discrepancy between experimental and numerical data for DM0 is expanded. It is expected that the combination of excessively high ultimate

stress and post-failure stress-strain response resulting from the Orthotropic Yield model parameter set derived by Nguyen et al. [15] is the cause of the discrepancy between the experimental data and the simulation results.

### 7.2.2 Material Stress Strength Model

For the Material Stress model, two separate sets of input parameters were considered. First, the material strength parameters were determined. Second, orthotropic post failure options were set to accurately simulate material impact response.

#### Material Strength Values

The through-thickness material strength was set in line with the value used in DM1, taken from Clegg et al. [68]. In-plane tensile failure stress is taken from Nguyen et al. [15], which was based on data from Heisserer et al. [92]. Maximal through-thickness shear stress values are set to the material strength reported by Ruiz-Ripoll et al. [88]. Maximum in-plane shear is kept at the value proposed by Nguyen et al. [15].

#### Material Post-Failure Options

For the DM2 model, the material Post Failure Option was set to Orthotropic to allow for a closer representation of material failure than was achieved using the Isotropic option. For all considered option sets, the Residual Shear Stiffness Fraction, Maximum Residual Shear Stress, Decomposition Temperature, Matrix Melt Temperature, Melt Matrix Failure Mode and Stochastic failure were kept at default settings. Three sets of failure coupling conditions, defined in Table 7.2 were considered. These were combined with the input parameters presented in Table 7.2 in Appendix A. The resulting models are referred to as IM2, IM3 and IM4. The material input are described in Table 7.2. They are combined with the input parameters in Appendix A.

**Table 7.2:** Material post failure coupling combinations for IM2, IM3 and IM4.

| | IM2 | IM3 | IM4 |
|---|---|---|---|
| Failed in 11, Failure mode | 11 only | 11 only | 11 only |
| Failed in 22, Failure mode | 22 only | 22 only | 12 & 22 only |
| Failed in 33, Failure mode | 33 only | 33 only | 31 & 33 only |
| Failed in 12, Failure mode | 12 & 22 only | 12 & 11 only | 12 & 11 only |
| Failed in 23, Failure mode | 23 & 33 only | 23 & 33 only | 23 & 33 only |
| Failed in 31, Failure mode | 31 & 33 only | 31 & 11 only | 31 & 11 only |

The three models were compared for four initials velocity cases, with impacts at 3100, 3532, 5370 and 6591 $m/s$. Particle smoothing lengths were set at 0.15 $mm$, as will be explained in Chapter 8. Targets with a thickness of 15 $mm$ and Aluminium impactors

with a 6 $mm$ diameter were used, conform [8]. The resulting residual velocities are presented in Table 7.3. These velocities are taken at $1.0 \cdot 10^{-1}$ $ms$ after impact, and represent particle velocities taken from within 15 $mm$ in front of the most forward, large concentration of impactor fragments. This margin is taken to account for the fact that the experimental data also contain target plate material. Excessive spallation was also frequently encountered during the simulations. For these cases, velocities in the front of the debris cloud did not give a reasonable representation of impactor residual velocities. For some cases with highly fragmented impactors, best estimates have been made regarding the measurement point.

**Table 7.3:** Experimental [8] and numerical residual velocities for IM2, IM3 and IM4. Numerical results are rounded of with a resolution of 50 $m/s$.

| $[m/s]$ | 3100 | 3532 | 5370 | 6591 |
|---|---|---|---|---|
| Exp [8] | 679 | 958 | 1730 | 2457 |
| IM2 | 1400 | 1500 | 1950 | - |
| IM3 | 600 | 900 | 1650 | 2300 |
| IM4 | 650 | 900 | 1650 | 2300 |

As can be seen in Table 7.3, IM2 significantly over-predicted impactor residual velocity. Furthermore, significant impactor fragmentation was already encountered at an impact velocity of 3100 $m/s$. For $V_0 = 6591$ $m/s$ the simulation failed because the time step became so small the simulation stagnated. Figure 7.13a presents a simulation result for an impact at $V_0 = 5370$ $m/s$ using IM2 at $t = 1.0 \cdot 10^{-1}$ $ms$ after impact, which illustrates the excessive fragmentation observed. So the IM2 set of parameters was discarded.

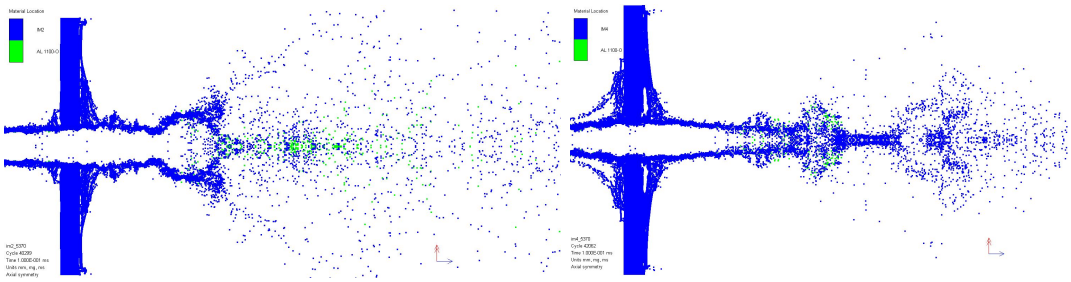

**(a)** Simulation result using IM2. **(b)** Simulation result using IM4.

**Figure 7.13:** Simulation results of a $V_0 = 5370$ $m/s$ impact using IM2 and IM4 at t=$1.0 \cdot 10^{-1}$ $ms$ after impact.

For both IM3 and IM4, comparable results were obtained, with IM4 giving a slightly closer approximation of the residual velocity at 3100 $m/s$. Debris cloud shapes were also very comparable. Relating Table 7.2 to Table 7.3 indicates that having in-plane material failure coupled to through-thickness shear failure, as done in IM2, results in strong overestimation of residual velocities. Of course, neither having failure in 11 or

22/33 direction directly follow from through-thickness shear failure is fully accurate. However, with the simple options available in the Material Stress Model, linking through-thickness shear to through-thickness normal failure yields quite a close approximation of experimental data. Comparing IM3 to IM4, it can be seen that linking failure having through-thickness shear failure follow from normal in-plane failure does not greatly affect material response. IM3 and IM4 both seem suitable candidates. Given the slightly better velocity prediction performance for the 3100 $m/s$ impact case seen in IM4, this set was selected for use in DM2.

Figure 7.13b presents a simulation result of an impact at $V_0 = 5370$ $m/s$ using IM4 at t=$1.0 \cdot 10^{-1}$ $ms$ after impact. This serves as illustration of the more coherent debris cloud obtained using IM3 and IM4, compared to IM2. If required, reference footage for this case is presented in Figure 9.7.

### 7.2.3 Orthotropic Shock EOS

For the DM2 model, the $S_1$ parameter was also chosen to have numerical and experimental IFPI data match. The $S_1$ parameter was set to a value of 1.5, which yielded a fit as presented in Figure 7.14.

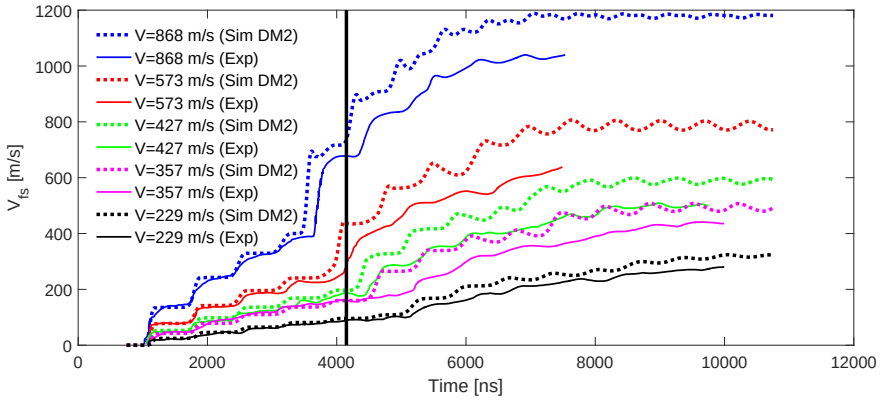


**Figure 7.14:** IFPI free surface velocity verification unit tests using DM2 and experimental data from Lässig et al. [8]. The vertical line represent the 3400 $ns$ after impact mark.

This figure shows a closer match between simulated and experimental rear face velocity data for lower $V_{fs}$ platforms. Again, it can be seen that numerical and experimental data start to diverge at around 3400 $ns$ after impact, which is the approximate time at which the assumption of 1D shock waves cease to be valid for the experimental tests.

### 7.2.4 DM2 Parameters

The modelling steps described in the current section have resulted in a combination of parameters for DM2 as described in Table 7.4.

**Table 7.4:** Input parameters for the DM2 material model.

| Parameter | Value | Unit | Source | Parameter | Value | Unit | Source |
|---|---|---|---|---|---|---|---|
| EOS: Orthotropic | | | | Failure: Material Stress | | | |
| Reference Density | 0.98 | $g/cm^3$ | [98] | Tensile Failure Stress 11 | $4.50 \cdot 10^4$ | $kPa$ | [68] |
| Young's modulus 11 | $3.62 \cdot 10^6$ | $kPa$ | [8] | Tensile Failure Stress 22 | $1.15 \cdot 10^6$ | $kPa$ | [92] |
| Young's modulus 22 | $5.11 \cdot 10^7$ | $kPa$ | [92] | Tensile Failure Stress 33 | $1.15 \cdot 10^6$ | $kPa$ | [92] |
| Young's modulus 33 | $5.11 \cdot 10^7$ | $kPa$ | [92] | Maximum Shear Stress 12 | $1.56 \cdot 10^5$ | $kPa$ | [88] |
| Poisson's Ratio 12 | 0.013 | – | [8] | Maximum Shear Stress 23 | $1.20 \cdot 10^5$ | $kPa$ | [15] |
| Poisson's Ratio 23 | 0 | – | [8] | Maximum Shear Stress 31 | $1.56 \cdot 10^5$ | $kPa$ | [88] |
| Poisson's Ratio 31 | 0.5 | – | [8] | | | | |
| Shear modulus 12 | $2.0 \cdot 10^6$ | $kPa$ | [15] | Post Failure Option: Orthotropic | | | |
| Shear modulus 23 | $1.92 \cdot 10^5$ | $kPa$ | [15] | Failed in 11, Failure mode | 11 only | | |
| Shear modulus 31 | $2.0 \cdot 10^6$ | $kPa$ | [15] | Failed in 22, Failure mode | 12 & 22 only | | |
| | | | | Failed in 33, Failure mode | 31 & 33 only | | |
| Volumetric Response: Shock | | | | Failed in 12, Failure mode | 12 & 11 only | | |
| Grüneisen coefficient | 1.64 | - | [94] | Failed in 23, Failure mode | 23 & 33 only | | |
| Parameter C1 | $3.57 \cdot 10^3$ | $m/s$ | - | Failed in 31, Failure mode | 31 & 11 only | | |
| Parameter S1 | 1.5 | – | Match to [8] | | | | |
| Reference Temperature | 293 | $K$ | - | Strength: Von Mises | | | |
| Specific Heat | $1.85 \cdot 10^3$ | $J/kgK$ | [98] | Shear Modulus | $2.0 \cdot 10^6$ | $kPa$ | [15] |
| | | | | Yield Stress | $1.0 \cdot 10^4$ | $kPa$ | [88] |

# Chapter 8

# Particle Density Refinement Study for Orthotropic Material Models

In this chapter, particle density refinement studies are presented for the DM1 and DM2 models for the combination of $AD = 15\ kg/m^2$ targets and 6 $mm$ diameter impactors.

## 8.1 DM1

For DM1, smoothing lengths of 1.0 $mm$, 0.50 $mm$, 0.20 $mm$, 0.15 $mm$, 0.10 $mm$ and 0.05 $mm$ were considered. Used impactor velocities were as presented in Table 8.1. Smoothing lengths of 1.0 $mm$, 0.5 $mm$, 0.2 $mm$ were found to be unsuitable for the considered cases. The fragmentation in both target and impactor meant that nodes, and therefore data points, became so scattered that obtaining meaningful data was deemed to be impossible. Figure 8.1 serves as illustration of this fact. Figure 8.1a presents a clear lack of penetrating material, making residual velocity estimates unreliable. Figure 8.1b is illustrative for the undeveloped debris cloud geometries obtained using $h = 0.50\ mm$.

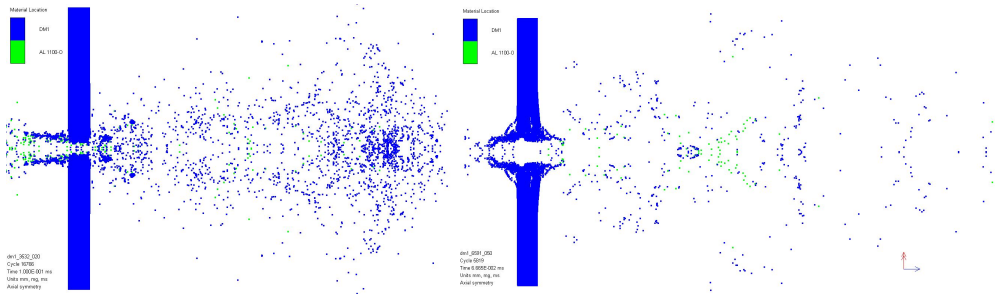

**(a)** Impact simulated using $h = 0.20\ mm$ with $V_0 = 3532\ m/s$ at $t = 1.0 \cdot 10^{-1}\ ms$ after impact.

**(b)** Impact simulated using $h = 0.50\ mm$ with $V_0 = 6591\ m/s$ at $t = 0.67 \cdot 10^{-1}\ ms$ after impact.

**Figure 8.1:** Illustration of complications encountered when using large smoothing length values in DM1 HVI simulations.

Residual velocity results for smoothing lengths of 0.15 $mm$ and 0.10 $mm$ are presented in Table 8.1. Two different measurement standards were used to obtain these velocity data. As will be presented in 9.1.2, simulations using DM1 managed to capture the

lateral expansion of the debris cloud, recreating the shape of the cloud quite accurately for the cases with an impact velocity of 5370 $m/s$ and 6591 $m/s$. For these two cases, the main simulated residual velocity value is taken from what could be identified as the front of the debris cloud if one were to ignore excessive spallation or over-penetration. For all other cases, the main values are as taken from the impactor material itself or the DM1 debris cloud within 15 $mm$ in front of it. Residual velocities caused by excessive spallation or over-penetration are reported between brackets.

**Table 8.1:** Residual velocity values for the DM1 models with 15 $kg/m^2$ AD targets and various particle smoothing lengths. Values between brackets represent the peak debris cloud velocity encountered.

| $[m/s]$ | 2052 | 2453 | 3100 | 3532 | 5370 | 6591 |
|---|---|---|---|---|---|---|
| Exp [8] | 0 | 0 | 679 | 958 | 1730 | 2457 |
| $h = 0.15\ mm$ | 50 (500) | 150 (1100) | 700 (2500) | 1150 (3850) | 1650 (2750) | 2400 (3150) |
| $h = 0.10\ mm$ | 150 (200) | 300 (1600) | 750 (2950) | 700 (3500) | 1700 (3000) | 2400 (3500) |

As can be seen from Table 8.1, excessive spallation is a general problem. This will be further discussed in Chapter 9. For the case with $h = 0.10\ mm$, with $V_0 = 6591\ m/s$, significant over-penetration from the impactor was observed, as will be further explained in Subsection 9.1.2. Therefore the value between brackets presented in this table is aluminium based, rather than DM1 based, as was done for all other cases.

An attempt was made to increase the particle density further to $h = 0.05\ mm$. This was done for impact velocities of $V_0 = 6591\ m/s$, $V_0 = 5370\ m/s$ and $V_0 = 3532\ m/s$. Two problems were encountered because of this last step. First, computational times soared to well in excess of 600 hours, by the end of which the in-simulation termination time of $t = 1.0 \cdot 10^{-1}\ ms$ still was not reached. As illustrated in Figure 8.2, it was also found that for $V_0 = 6591\ m/s$, simulations became erratic. This case is to be compared to experimental footage as presented in Figure 9.10. Clearly, a larger particle density does not necessarily lead to a more converged solution.

Table 8.1 shows that, taking the measurement uncertainties that accompany fragmentation processes into account, the residual velocities of the aluminium based parts of the debris cloud vary little between the two considered cases. Given the extensive fragmentation observed for simulations using $DM1$, it was decided that the higher of the two particle densities, so using $h = 0.10\ mm$, is the more desirable option. The higher resolution was found aid in analysis of debris cloud features. The over-penetration by the impactor for the $h = 0.10\ mm$ case was found to be a cause for concern. This topic will be further discussed in Chapter 9 and 11.

From this point onwards, all simulations of DM1 will use a smoothing length of $h = 0.10\ mm$. Per extension, this also holds for simulations using KFRP.

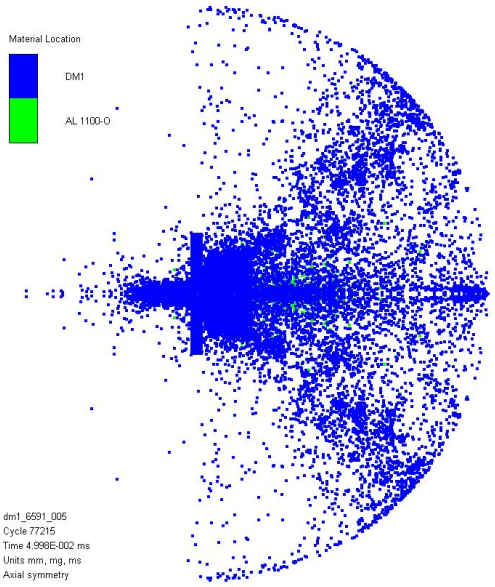


**Figure 8.2:** Simulation results of a $V_0 = 6591\ m/s$ impact using DM1 at $t = 0.5 \cdot 10^{-1}\ ms$ after impact generated using $h = 0.05\ mm$.

## 8.2 DM2

For model DM2, smoothing lengths of 0.2 $mm$, 0.15 $mm$, 0.10 $mm$ were considered. As will be discussed in Chapter 9, DM2 was found to predict far less fragmentation than DM1. This behaviour was also observed during the mesh refinement study. This has as consequence that increasing particle density was not required to help in interpretation of produced debris clouds. For all considered smoothing lengths, debris cloud geometry was stable and comparable. This is illustrated in Figure 8.3, where smoothing lengths of $h = 0.10\ mm$ and $h = 0.20\ mm$ are used to simulate a $V_0 = 6591\ m/s$ impact.

As can be seen from Table 8.2, reduction of the particle smoothing length to $h = 0.10\ mm$ allows for the ballistic limit to be accurately reproduced. Since the model is in this case intended to predict secondary damage, rather than ballistic limits, this final layer of accuracy was deemed not necessary. A smoothing length of 0.15 was therefore deemed to be sufficient for DM2. From this point onwards, all simulations of DM2 will use a smoothing length of $h = 0.15\ mm$.

**Table 8.2:** Residual velocity values for the DM2 models with $15\ kg/m^2$ AD targets and various particle smoothing lengths. Values between brackets represent the peak debris cloud velocity encountered.

| $[m/s]$ | 2052 | 2453 | 3100 | 3532 | 5370 | 6591 |
|---|---|---|---|---|---|---|
| Exp [8] | 0 | 0 | 679 | 958 | 1730 | 2457 |
| $h = 0.20\ mm$ | 150 (1750) | 0 (2100) | 500 (2400) | 700 (2450) | 1750 (3150) | 2300 (3350) |
| $h = 0.15\ mm$ | 100 (1650) | 0 (2000) | 650 (2100) | 900 (2200) | 1650 (3250) | 2300 (3250) |
| $h = 0.10\ mm$ | 0 (1700) | 0 (2150) | 650 (2250) | 900 (2500) | 1650 (3500) | 2250 (3350) |

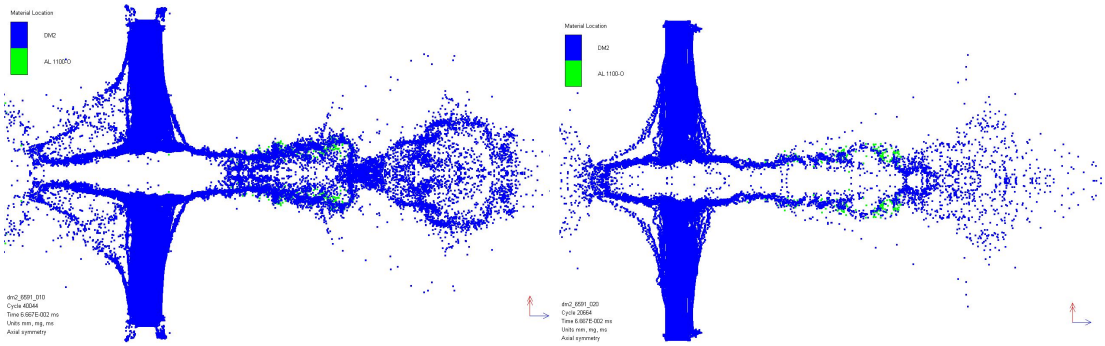

**(a)** $h = 0.10\ mm$. **(b)** $h = 0.20\ mm$.

**Figure 8.3:** Simulation results of a $V_0 = 6591\ m/s$ impact using DM2 at $t = 0.67{\cdot}10^{-1}\ ms$ after impact generated using different smoothing lengths.

# Chapter 9

# Evaluation and Validation of Proposed Dyneema® Models

Throughout this report, at various points, comparisons have been made between experimental and numerical data. In this chapter, the two proposed impact response models for Dyneema® HB26 material models are presented again in a more detailed and structured manner. These data are compared to the experimental data from Lässig et al. [8]. To obtain a better perspective of the behaviour of the proposed material models, comparisons are also presented between the two proposed models, and simulation results from the KFRP model proposed by Clegg et al. [68] and the Lagrangian element-based model proposed by Lässig et al. [8].

## 9.1 Experimental Validation of DM1 and DM2

In this section, a detailed comparison between experimental and numerical results from DM1 and DM2 is presented. The focus here is both on comparing the predicted residual velocities, and on evaluation of the general debris cloud shape. Experimental residual velocity data are taken from Lässig et al. [8]. Assessment of the debris cloud shape will be performed on a qualitative basis. Further processing of the debris cloud footage could yield information such as the radial size or velocity of the more fragmented debris clouds. This step was considered to be beyond the scope of this project, but performing this processing step is still recommended.

### 9.1.1 Residual Velocity Validation

In Table 9.1 the maximal experimental debris cloud velocities and numerical residual velocities are presented. It must be stated that all velocity values are determined, based on measurements performed using engineering judgement. Due to the nature of SPH-based discretisation, significant fragmentation of both target and impactor was sometimes encountered. Substantial variation between the velocity of adjacent particles, and difficulty in determining the exact cloud feature to use as measurement point, sometimes introduced numerical uncertainty.

In Table 9.1 velocity values between brackets represent the maximum velocity encountered for the numerical model. This value is included to give an indication of the amount

of spallation encountered. The other value represents the best estimate for the impactor residual velocity. For DM2, these values are as taken from the DM2 debris cloud directly in front of the impactor. To account for the 15 $mm$ thickness of the target plate in the experimental set-up, these measurements were taken within 15 $mm$ of the front of the impactor fragments. For DM1, two different measurement standards were used. As will be presented in Section 9.1.2, simulations using DM1 managed to capture the lateral expansion of the debris cloud, recreating the shape of the cloud quite accurately for the cases with an impact velocity of 5370 $m/s$ and 6591 $m/s$. For these two cases, the main simulated residual velocity value is taken from what could be identified as the front of the debris cloud if one were to ignore excessive spallation or over-penetration.

**Table 9.1:** Residual velocity values for the DM1 and DM2 models with 15 kg/m$^2$ AD targets. Values between brackets represent the peak debris cloud velocity encountered.

| $[m/s]$ | 2052 | 2453 | 3100 | 3532 | 5370 | 6591 |
|---|---|---|---|---|---|---|
| Exp [8] | 0 | 0 | 679 | 958 | 1730 | 2457 |
| DM1 | 150 (200) | 300 (1600) | 750 (2950) | 700 (3500) | 1700 (3000) | 2400 (3500) |
| DM2 | 100 (1650) | 0 (2000) | 650 (2100) | 900 (2200) | 1650 (3250) | 2300 (3250) |

### 9.1.2 Qualitative Debris Cloud Comparison

In this section, photographic footage for the experimental impact test cases is compared to their simulated counter parts. Each of the following subsubsections will be dedicated to one of the experimental impact cases available. The velocities used are 2453 $m/s$ to represent an impact below the ballistic limit, 3532 $m/s$ to represent an impact in the velocity range where DM1 struggled, and 5370 $m/s$ and 6591 $m/s$ to represent the highest available impactor velocities. For the first three cases, the footage is taken at $t = 1.0 \cdot 10^{-1}$ $ms$ after impact. For the 6591 $m/s$ impactor velocity case, footage is taken $t = 0.67 \cdot 10^{-1}$ $ms$ after impact because the quality of the experimental footage was better at this time stamp.

#### $V_0$ = 2453 m/s Impact Case

Experimental footage portraying the result of the impact at 2453 $m/s$ case is presented in Figure 9.1. Since this impact velocity is below the ballistic limit, no penetration occurred.

Considering the simulated case using DM1 presented in Figure 9.2 it can be seen that the ballistic limit is not fully captured by this model. Substantial fragmentation of the impactor was observed, combined with penetration of the target. The residual velocity of the main surviving aluminium fragment, presented in Figure 9.2b was about 300 $m/s$. Substantial spallation of the target is also encountered, as presented in Figure 9.2a.

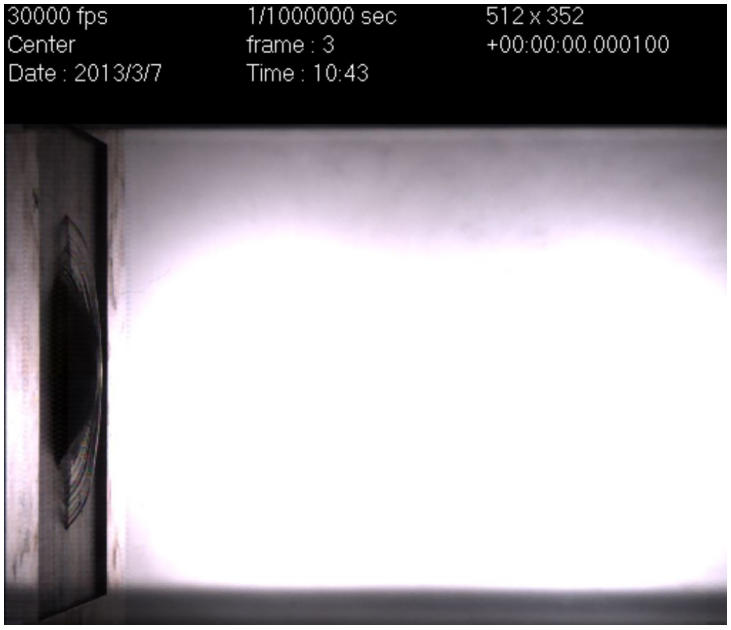


**Figure 9.1:** Experimental footage with $V_0 = 2453\ m/s$ at $t = 1.0 \cdot 10^{-1}\ ms$ after impact, showing no penetration [8].

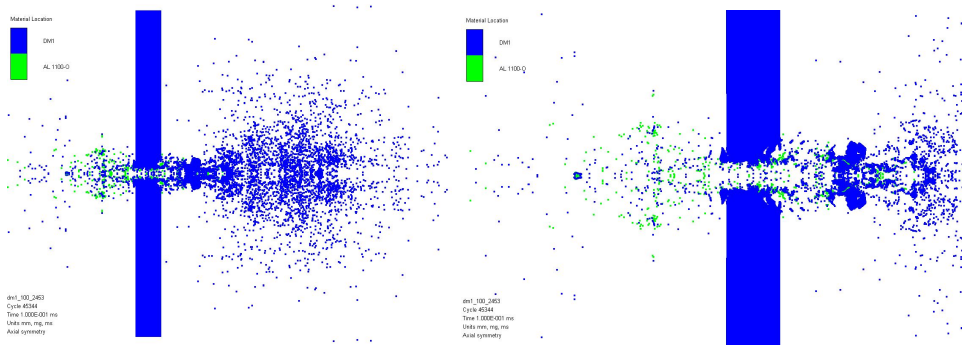

**(a)** Simulation still-shot.

**(b)** Enlarged image focussing on impactor fragments.

**Figure 9.2:** Simulated debris clouds using DM1 for $V_0 = 2453\ m/s$ at $t = 1.0 \cdot 10^{-1}\ ms$ after impact.

In Figure 9.3, simulation results using DM2 are presented. In Figure 9.3b it can be seen that the ballistic limit is better approximated by DM2. Perforation still occurs, but the impactor material fails to achieve any significant residual velocity. Again, excessive spallation is present, as can be seen in Figure 9.3a.

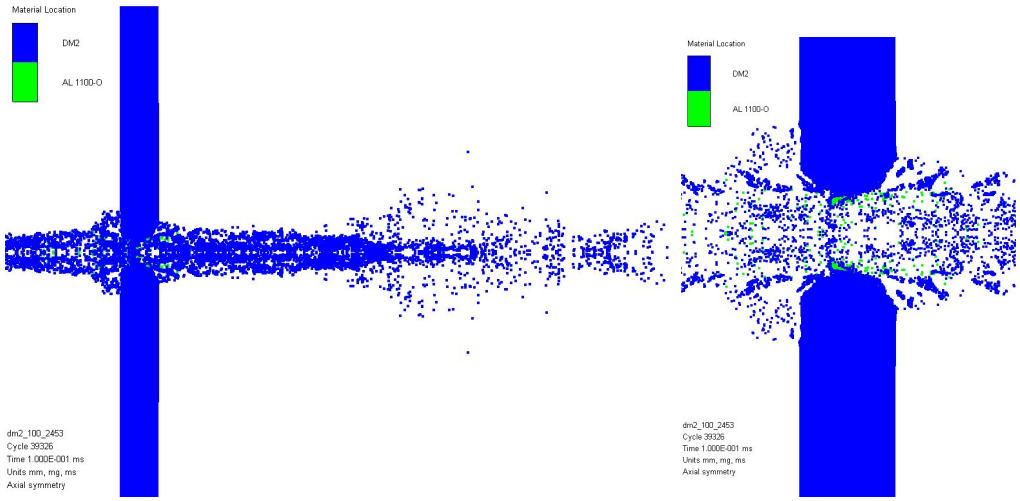


**(a)** Simulation still-shot.

**(b)** Enlarged image focussing on impactor fragments.

**Figure 9.3:** Simulated debris clouds using DM2 for $V_0 = 2453\ m/s$ at $t = 1.0 \cdot 10^{-1}\ ms$ after impact.

### $V_0$ = 3532 m/s Impact Case

Figure 9.4 presents experimental footage from the impact case with an initial velocity of 3532 $m/s$. It can clearly be seen penetration has occurred. Given the shape of the resulting debris cloud, it is expected that the impactor has remained at least partially intact and is present in the front of the debris cloud. Torn-out Dyneema® yarns can be seen to fan out from the impact site.

Simulation results obtained using DM1 are presented in Figure 9.5. Significant fragmentation of the impactor is encountered. Figure 9.5b shows that the forward travelling (moving right) debris cloud contains several larger aluminium fragments, but no mostly intact main impactor body. The front of the aluminium cloud had a residual velocity of about 700 $m/s$. The relatively large concentration of DM1 material on the right edge of Figure 9.5b does have a residual velocity of around 1000 $m/s$. In Figure 9.5a, again, excessive spallation can be observed.

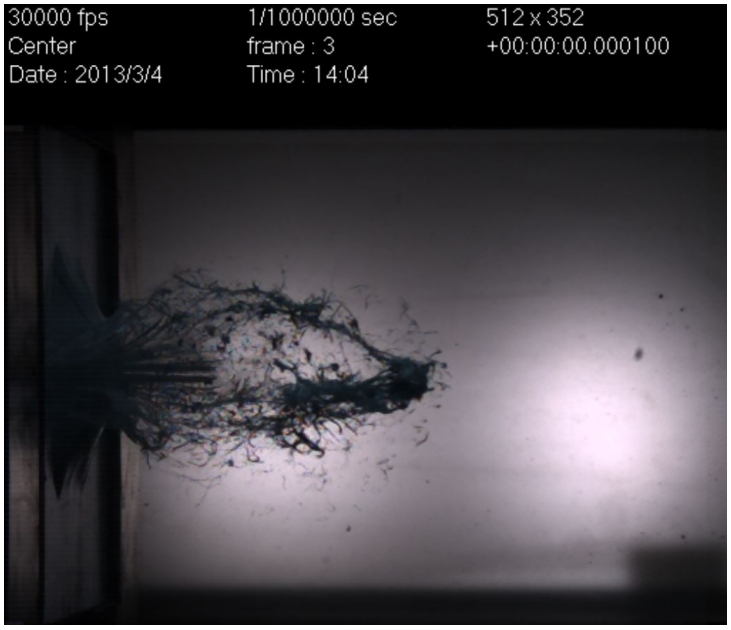


**Figure 9.4:** Experimental footage with $V_0 = 3532\ m/s$ at $t = 1.0 \cdot 10^{-1}\ ms$ after impact [8].

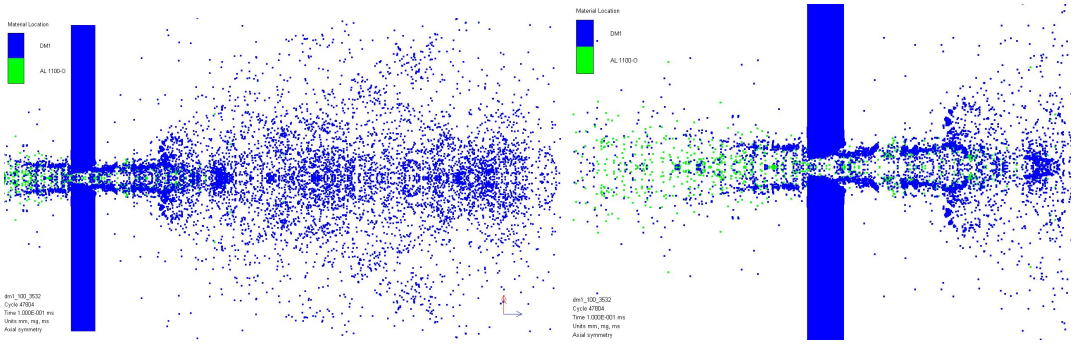

**(a)** Simulation still-shot.

**(b)** Enlarged image focussing on impactor fragments.

**Figure 9.5:** Simulated debris clouds using DM1 for $V_0 = 3532\ m/s$ at $t = 1.0 \cdot 10^{-1}\ ms$ after impact.

Figure 9.6 presents simulation results obtained using DM2. The main fragment of the aluminium impactor was located in the tip of the part of the debris cloud showed in Figure 9.6b. Comparing Figure 9.6b to Figure 9.6a, it can again be seen significant excessive spallation occurred.

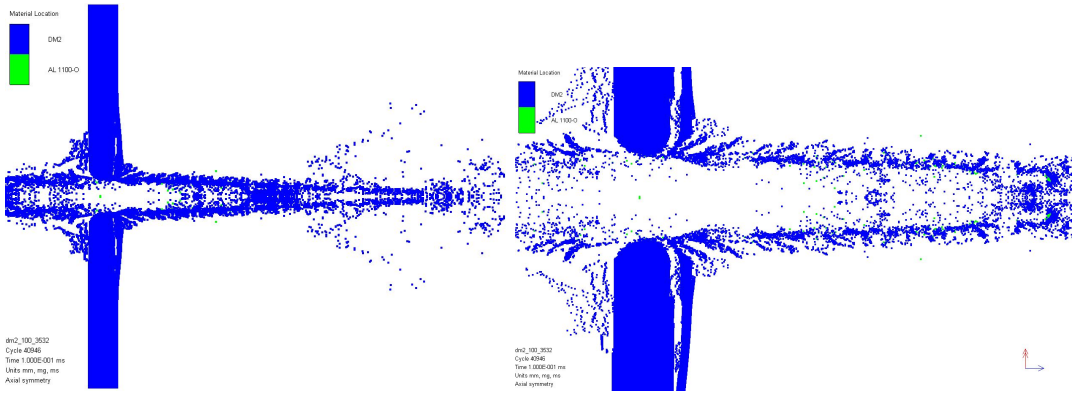


**(a)** Simulation still-shot.

**(b)** Enlarged image focussing on impactor fragments.

**Figure 9.6:** Simulated debris clouds using DM2 for $V_0 = 3532\ m/s$ at $t = 1.0 \cdot 10^{-1}\ ms$ after impact.

### $V_0$ = 5370 m/s Impact Case

Figure 9.7 represents experimental footage for the impact response to a 5370 $m/s$ impact. This velocity is notable for two reasons. Firstly, for all impacts up to this point, the state and location of the impactor could be estimated somewhat reasonably. In case of the ballistic limit, penetration simply did not occur, and for the impact velocities of 3100 $m/s$ and 3532 $m/s$ a mostly intact impactor in the front of the debris cloud seemed reasonable. In Figure 9.7, though, significant fragmentation can be observed. Within the scope of this thesis, it was not feasible to accurately deduce the nature of each of the fragments on display. It stands to reason that most of the outer halo consists of fibre material being flung outward by the impact, and that most of the impactor debris should be expected in the inner cone that can be distinguished in Figure 9.7. A second notable point, is that the maximal residual velocity in the experimental debris cloud is 1730 $m/s$. This is relatively close to the reported through-thickness bulk speed of sound 1922 $m/s$ for the material [8]. So this is the first data point where nearly the complete impact process occurs within the hypervelocity regime.

Figure 9.8 presents simulation results obtained using DM1. Figure 9.8b presents a zoomed-in caption of what was considered to be the main body of the debris cloud. It is the velocity of the leading edge of this main cloud that was taken as the velocity reported in Table 9.1. Comparing these results to Figure 9.7, it can be seen that the simulation does not include the halo mentioned earlier. The location of the impactor debris in this simulation corresponds to the concentration in debris in the middle of the halo present in Figure 9.7. Whether this location is correct cannot be ascertained because of the difficulty in distinguishing between impactor and composite-based debris in Figure 9.7. At least some impactor debris was expected closer to the leading edge of the main debris cloud to act as a driving force in the target penetration process. Further post-processing of the footage or x-ray-based footage in further experiments

are recommended to provide additional insights into this matter. Figure 9.8a gives a representation of the extent to which excessive spallation occurred.

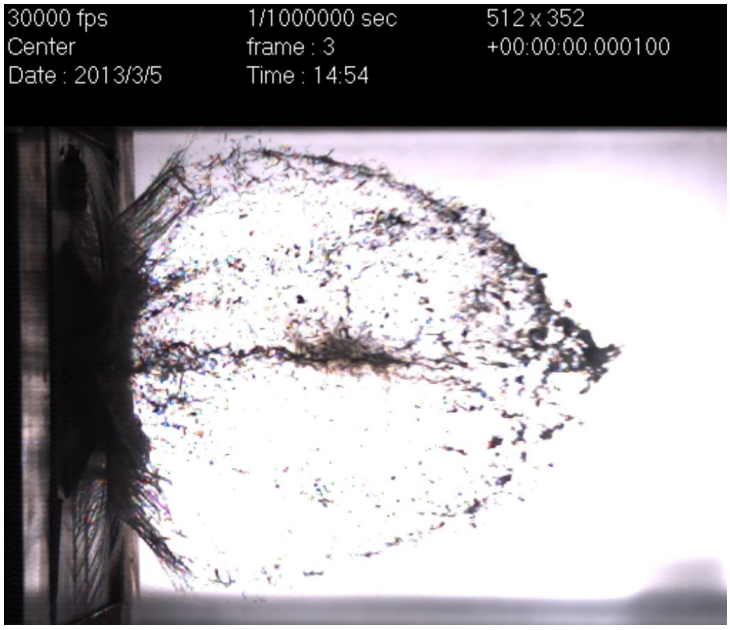


**Figure 9.7:** Experimental footage with $V_0 = 5370\ m/s$ at $t = 1.0 \cdot 10^{-1}\ ms$ after impact [8].

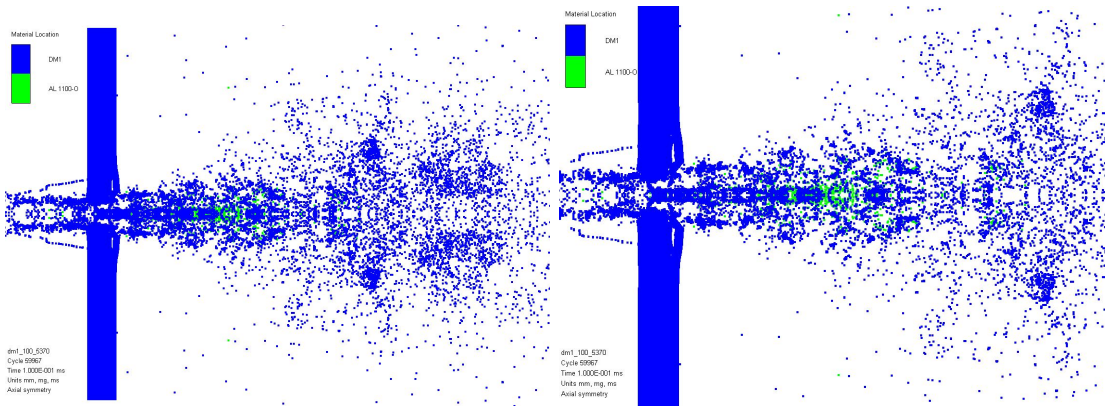

**(a)** Simulation still-shot.

**(b)** Enlarged image focussing on impactor fragments.

**Figure 9.8:** Simulated debris clouds using DM1 for $V_0 = 5370\ m/s$ at $t = 1.0 \cdot 10^{-1}\ ms$ after impact.

Figure 9.9 presents simulated results obtained using DM2 under an impact at 5370 $m/s$. Velocity measurements were performed around the main impactor fragments present in

the tip of the debris cloud presented in Figure 9.9b. Note that for DM2, the assumption that the impactor-based debris should be located around the leading edge of the debris cloud gives reasonable residual velocity results, as presented in Table 9.1. Another notable feature is that the debris cloud follows a narrow path. Fanning out, as seen for all DM1-based simulations in this section, is hardly observed. For the case with an impact velocity of 3532 $m/s$, this shape did correspond to the experimental observation, but for the cases with impact velocities at 5370 $m/s$ and 6591 $m/s$ discussed in the next subsubsections, this deviation becomes more notable. A feasible explanation for this is that failure in through-thickness shear direction is set to induce failure in 11 (through-thickness) direction, as was explained in Subsection 7.2.2.

Whether this lack of radial expansion is a problem for the model depends on its intended application. If one is mainly interested in the damage propagation behaviour of a debris cloud and its effect on an inner wall of a SWS, it is of little to no consequence. If one is interested in the scatter of the post-impact scatter of the composite for other reasons, it could reduce the suitability of the model.

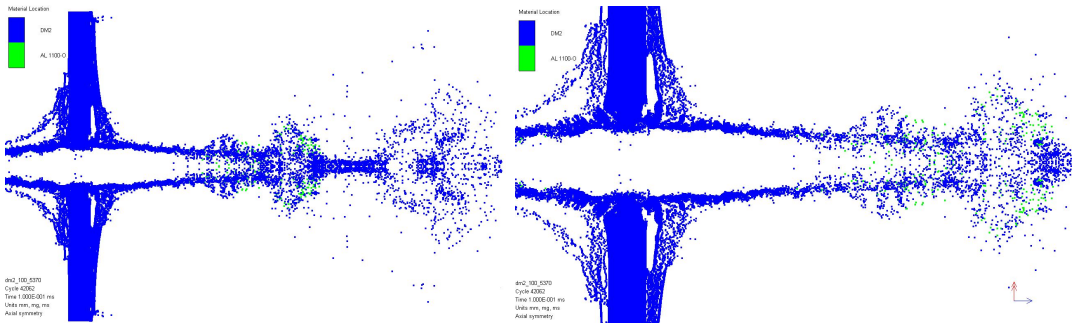

**(a)** Simulation still-shot.

**(b)** Enlarged image focussing on impactor fragments.

**Figure 9.9:** Simulated debris clouds using DM2 for $V_0 = 5370\ m/s$ at $t = 1.0 \cdot 10^{-1}\ ms$ after impact.

Besides the matter of radial debris cloud expansion, the most notable difference between the results obtained using DM1 and DM2 is in the location and residual velocity of the debris originating from the impactor. With the experimental data currently available, no conclusive statement is possible as to which one represents reality more closely.

### $V_0$ = 6591 m/s Impact Case

Figure 9.10 shows footage from the impact case with an initial velocity of 6591 $m/s$. This footage is taken at $t = 0.67 \cdot 10^{-1}\ ms$ after impact, rather than the $t = 1.0 \cdot 10^{-1}\ ms$ used for the other cases, because the experimental footage was clearer. With this last increase in impactor velocity, the point has been reached where the complete impact process is taking place in the hypervelocity regime. Figure 9.10 presents significant fragmentation

of both impactor and target. The halo first mentioned when discussing the 5370 $m/s$ impact velocity case can still be distinguished. For this case, it can clearly be seen that the left half of this halo at least consists of fibre material flung outwards during the impact. Again, a clear cone containing most of the debris can be identified.

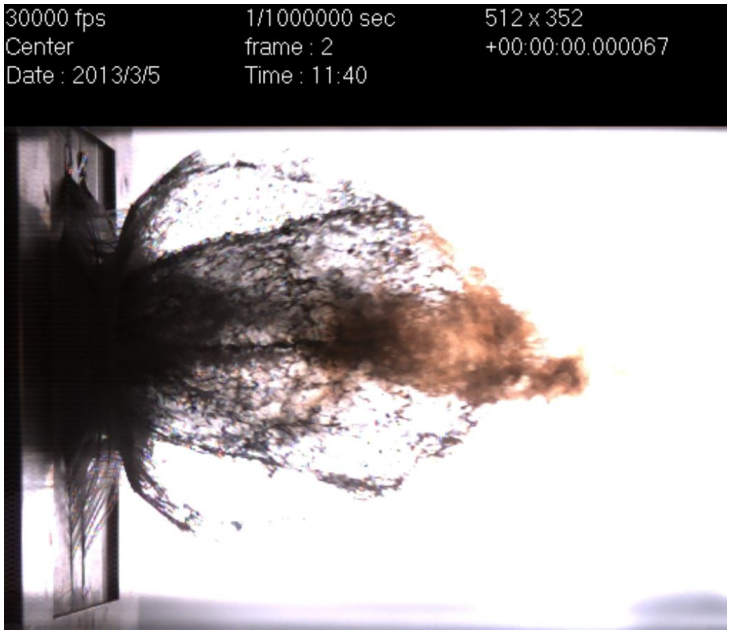


**Figure 9.10:** Experimental footage with $V_0 = 6591\ m/s$ at $t = 0.67 \cdot 10^{-1}\ ms$ after impact [8].

Figure 9.11 presents simulation results obtained using DM1. In contrast to the excessive spallation encountered for DM1 for the previous cases, over-penetration is clearly present here. Figure 9.11b presents what was identified to be the main debris cloud. Again, this does not include the outer debris halo, but the main debris cone can be seen to be represented reasonably well. The front of the cloud presented in Figure 9.11b is where the velocity reported in Table 9.1 is taken. Looking at Figure 9.11b, it can be seen that some impactor material penetrates beyond the main-debris cloud presented in Figure 9.11b. This plume is the result of the over-penetrating impactor.

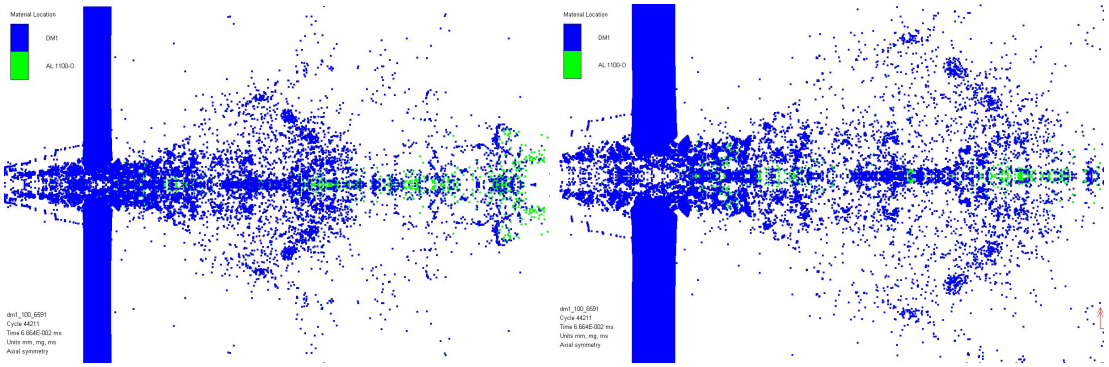

**(a)** Simulation still-shot.

**(b)** Enlarged image focussing on impactor fragments.

**Figure 9.11:** Simulated debris clouds using DM1 for $V_0 = 6591\ m/s$ at $t = 0.67 \cdot 10^{-1}\ ms$ after impact.

Figure 9.12 presents simulation results from obtained using DM2. Again, the rather narrow debris cloud trajectory can be identified. Looking at the evolution from Figure 9.3 to 9.12, it can be seen that as velocity increased, the amount of the debris cloud that could be classified as excessive spallation reduced.

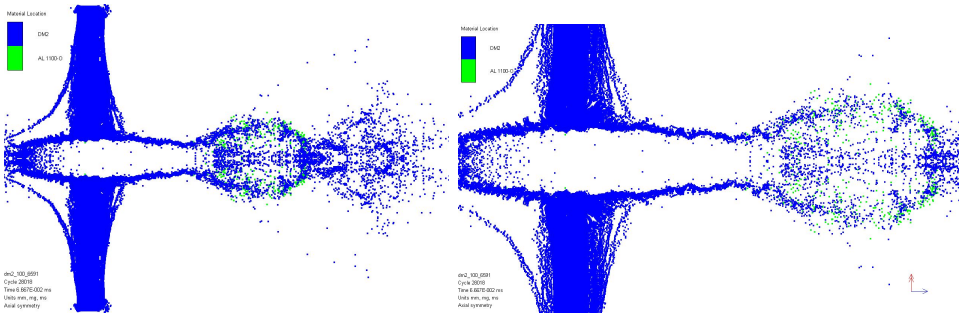

**(a)** Simulation still-shot.

**(b)** Enlarged image focussing on impactor fragments.

**Figure 9.12:** Simulated debris clouds using DM2 for $V_0 = 6591\ m/s$ at $t = 0.67 \cdot 10^{-1}\ ms$ after impact.

### 9.1.3 Reflection on DM1

Assessing all results for DM1 presented in Subsection 9.1.1, one main observation can be made. Namely that for all impact cases, except for the case with an initial velocity of 6591 $m/s$, the leading edge of the debris cloud was inflated by excessive spallation. Particles in these regions were found to have higher than experimentally determined velocities, as presented in Table 9.1. For the case with an initial impact velocity of 6591 $m/s$, in turn, over-penetration was encountered. This indicates that the model

does not systematically under- or over-predict the ballistic performance of the physical laminate. An impact velocity or strain rate dependence appears to exist. Part of the problem may be attributed to the fact that a spall strength was used that belongs to a different material. Namely a stiff, epoxy-aramid composite [68], rather than a flexible polyurethane-UHMWPE-based composite. Since this spall strength affects the through-thickness shear behaviour of the model, which in turn affects the through-thickness compressive behaviour of the material model, this potentially faulty value could have an affect on the material model.

A similar concern holds for the through-thickness compressive stress-strain data, taken from Shaker et al. [97], used for the calibration of the $a_{11}$ parameter in DM1. Shaker et al. [97] themselves report the SHB generated stress-strain data are material dependent. Since they are not using Dyneema® HB26, this may cause part of the discrepancy between the simulated and experimental results. Per extension, this argument of uncertainty about the suitability of third party data obtained from literature and the subsequent fit to these data achieved by DM1, holds to a larger or smaller extent for all parts of the model.

A potentially more fundamental limitation of the model may be found in the fact that Wicklein et al. [70] and Shaker et al. [97] report strain rate dependent stress-strain behaviour. A consequence of such a dependence would be that one set of model parameters may not be able to accurately cover all impact cases in the first place. This problem would subsequently be further exacerbated by the use of thick laminates. The deceleration of the impactor during the penetration process would mean different regions of the target are be subjected to different strain rates. To assess whether the 15 $kg/m^2$ laminate used in this study should be considered a thick laminate and whether this should be expected to affect the model performance three steps were taken. These consist of comparisons with both the SPH-based KFRP model presented by Clegg et al. [68] and the element-based model proposed by Lässig et al. [8]. Further discussion of these steps is presented in Section 9.2, 9.3 and Chapter 10.

### 9.1.4 Reflection on DM2

Simulations using DM2 have demonstrated that, for the available cases, the model has been able to match experimental ballistic limit and residual velocity data with reasonable accuracy. This is illustrated in Table 9.1. In Section 9.1.2 it was also demonstrated DM2 generally suffers from excessive spallation and produced very narrow debris clouds. Whether these two aspects of the model are prohibitive to any user will depend on his intended application. Given the model validation that has been available, it appears that DM2 can be used as a first-order residual velocity estimation tool. The relatively low density of the material in the part of the debris cloud that has so far been labelled as excessive spallation, means this model can most likely also be used for secondary damage estimations. Use outside the validation range should always be combined with proper reflection on the assumptions made.

## 9.2 Comparison with 15 kg/m$^2$ KFRP Models

To gain additional insights into whether the behaviour of DM1, as described in Subsection 9.1.2 and 9.1.3, can be linked to the used target AD, a comparison with the KFRP model published by Clegg et al. [68] is made. This model contains exactly the same material sub-models as those used in DM1. Riedel et al. [69] mention a nominal thickness of 5.7 $mm$ for their KFRP composite samples. With a reported bulk density for the KFRP of 1.65 $g/cm^3$ [68] this equates to an areal density of about 9.4 $kg/m^2$, which is considerably less than the 15 $kg/m^2$ targets used by Lässig et al. [8]. For equal AD comparison purposes, 9.0 $mm$ thick KFRP models were created. In-plane dimensions, impactor parameters and boundary conditions were kept equal to those used for the DM1 and DM2 models. Smoothing length was set to 0.1 $mm$. The considered impact velocities were $V_0 = 3532$ $m/s$, $V_0 = 5370$ $m/s$ and $V_0 = 6591$ $m/s$.

For the KFRP model, input parameters as reported by Clegg et al. [68] were used. The one change is that the shear strength in 23 direction was changed from $2.0 \cdot 10^4$ $kPa$, as mentioned in [68] to $2.0 \cdot 10^5$ $kPa$ to better preserve consistency with unit test data presented in the article.

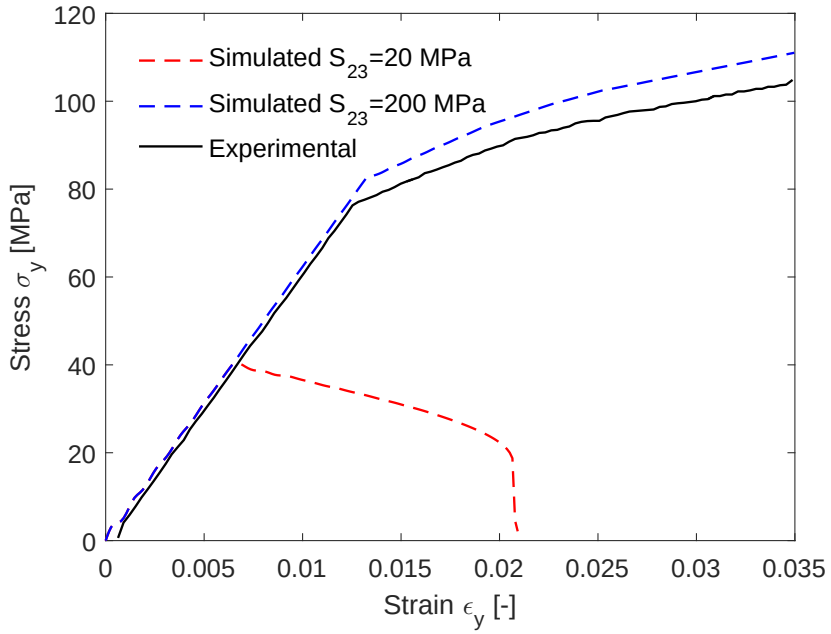


**Figure 9.13:** Experimental and numerical stress-strain response of in-plane tensile tests at 45° to fibre direction of KFRP samples using varying in plane shear strength-based on [68].

Figure 9.14 and 9.15 present simulated impact responses using the KFRP model for 9.0 $mm$ thick targets under 3532 $m/s$ and 6591 $m/s$ impacts respectively.

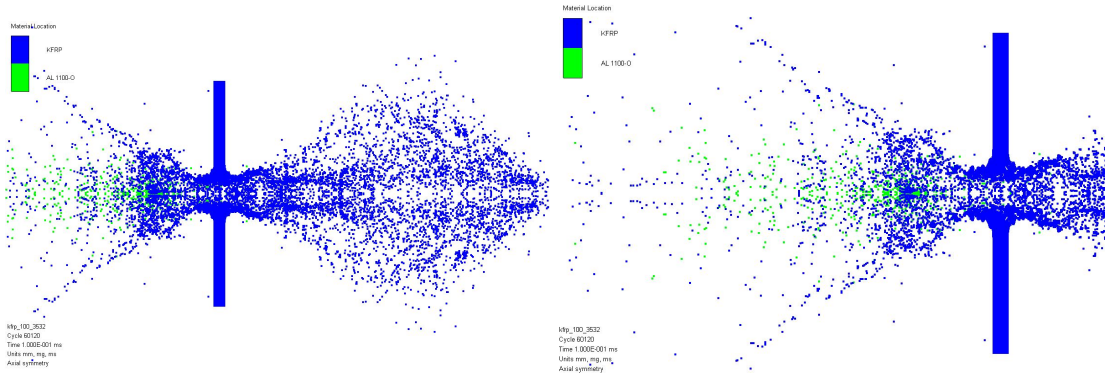


**(a)** Simulation still-shot.

**(b)** Enlarged image focussing on impactor fragments.

**Figure 9.14:** Simulated debris clouds using KFRP for $V_0 = 3532\ m/s$ at $t = 1.0 \cdot 10^{-1}\ ms$ after impact.

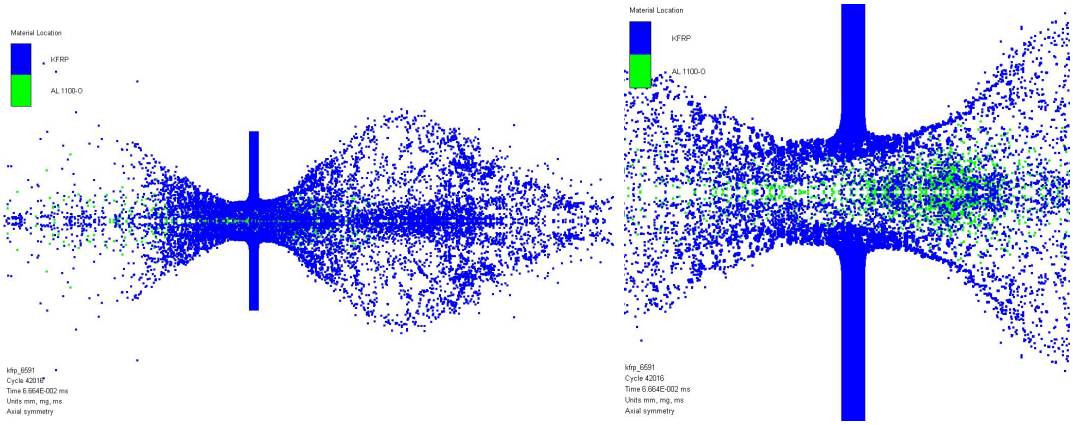


**(a)** Simulation still-shot.

**(b)** Enlarged image focussing on impactor fragments.

**Figure 9.15:** Simulated debris clouds using KFRP for $V_0 = 6591\ m/s$ at $t = 0.67 \cdot 10^{-1}\ ms$ after impact.

To further facilitate comparison between the behaviour of DM1 and DM2, and KFRP models using a single measure Table 9.2 presents a comparison of the momentum in $x$-direction of the aluminium impactor, 100 microseconds after impact. The parameter $(p_{x0})$ denotes the momentum of the impactor at the associated velocity before the impact. The choice for the $x$-momentum as physical quantity to use for this comparison is because it contains both a measure of damage potential of the impactor and, unlike kinetic energy, takes directionality into account.

**Table 9.2:** Residual $x$-momentum values of the impactor for the DM1, DM2 and KFRP models with 15 kg/m$^2$ AD targets.

| $[m/s]$ | 3532 | 5370 | 6591 |
|---|---|---|---|
| $p_{x0}$ $[kg \cdot m/s]$ | 1.06 | 1.61 | 1.97 |
| DM1 $[kg \cdot m/s]$ | 0.030 | 0.150 | 0.288 |
| DM2 $[kg \cdot m/s]$ | 0.081 | 0.272 | 0.397 |
| KFRP $[kg \cdot m/s]$ | -0.402 | -0.192 | -0.074 |

For the case with $V_0 = 3532\ m/s$, it can be seen in Figure 9.14 that full impactor reversal has occurred during the impact. For the $V_0 = 6591\ m/s$ impact case, it has can be seen that penetration does occur. It is accompanied by substantial spallation and consulting Table 9.2 it can be found that the net $x$-momentum of the impactor has become negative.

Absent the availability of direct impact validation data for the KFRP for this thesis, two hypotheses are put forward to explain the observed response of the KFRP model. First, the possibility exists that 15 $kg/m^2$ of physical KFRP would actually stop a 6.0 $mm$ diameter Al 1100-O impactor. In that case, the excessive fragmentation and negative net $x$-momentum would be signs from the SPH-based model that it is predicting a ballistic limit, but that the target model cannot maintain cohesion under the dynamic loading. Second, it is possible that the complex orthotropic models used in DM1 and KFRP struggle with capturing the response of laminates that are thick compared to the impactor size, modelled with SPH.

Absent direct physical impact data on 15 $kg/m^2$ KFRP models, neither of these two hypotheses can be definitively excluded. However, observing comparable behaviour in equal AD simulations using both DM1 and KFRP, the second explanation appears reasonable.

## 9.3 Comparison with 15 kg/m$^2$ Element-Based Models

Given the hypothesis that target thickness plays a role in the behaviour observed for the DM1 model, the logical next step was to perform simulations using thinner target plates. The results of this investigation will be reported in Chapter 10. Absent validation data for impacts into thinner laminates, though, an attempt had to be made to obtain reference data via an alternative method. For this, simulations on Lagrangian element-based targets modelled with the material proposed by Lässig et al. [8] were proposed. This material model will be referred to as HB26T.

Modelling was performed as described in [8] with two notable exceptions. First, discretisation was performed in Autodyn, which means meshing with a double gradient in the in-plane directions and constant element size along the target edges, as presented in [8] was not possible. Instead, a double gradient as presented in Figure 9.16 was used. The target was modelled using Lagrangian elements without symmetry constraints, so

the full 200 $mm$ x 200 $mm$ x 15 $mm$ target was generated. The target centre is meshed with 35 by 35 by 10 elements that are 1.5 $mm$ in all directions, in line with Lässig et al. [8]. The total target contains 55 elements in $x$- and $y$-directions respectively. For the impactor, 6 elements were used through the radius. The second deviation was that no boundary conditions were used along the edge of the plate. This is in line with the model as proposed by Nguyen et al. [15], whereas Lässig et al. [8] constrained movement in $z$-direction.

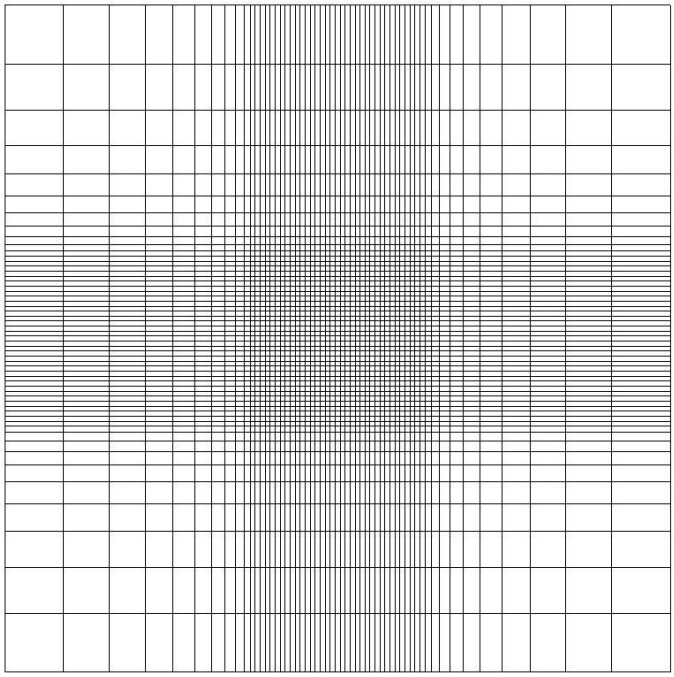

**Figure 9.16:** Grid as used for Lagrangian element-based impact simulations on 15 $kg/m^2$ targets using the material model described by Lässig et al. [8].

Cases with initial impactor velocities of $V_0 = 3532\ m/s$, $V_0 = 5370\ m/s$ and $V_0 = 6591\ m/s$ were considered. Simulations were set to run up to $1 \cdot 10^{-1}\ ms$. Two notable observations were made. First, of the three considered cases, only one was able to run for the full prescribed simulation time. All others were prematurely terminated by the program. In-simulation times at which wrap-up occurred are $t = 1.0 \cdot 10^{-1}\ ms$, $t = 0.958 \cdot 10^{-1}\ ms$ and $t = 0.598 \cdot 10^{-1}\ ms$.

This problem is attributed to a failure in the Geometric Strain erosion criterion, also noted by Nguyen et al. [15]. Geometric erosion is controlled by the measure represented in Equation 9-1 [87]. As was pointed out by Nguyen et al. [15], premature through-thickness material failure can cause strain combinations that mean the $\varepsilon_{eff}$ remains below the 2.5 value for the target plate used by Lässig et al. [8], even for severely distorted elements.

In Figure 9.17, an effective strain plot for the results from the $V_0 = 5370\ m/s$ impact case

are represented. Red colouration represents the maximal effective strain encountered in the model, which corresponds to a value of 2.102. This means that the geometric strain erosion criterion can fail to identify severely deformed elements, which go on to cause computational problems that resulted into premature termination. It was this observation that prompted Nguyen et al. [15] to formulate their in-plane damage-based erosion criterion.

$$\varepsilon_{eff} = \frac{2}{3}\left[\left(\varepsilon_1^2 + \varepsilon_2^2 + \varepsilon_3^2\right) - (\varepsilon_1\varepsilon_2 + \varepsilon_2\varepsilon_3 + \varepsilon_3\varepsilon_1) + 3\left(\varepsilon_{12}^2 + \varepsilon_{23}^2 + \varepsilon_{31}^2\right)\right]^{1/2} \tag{9-1}$$

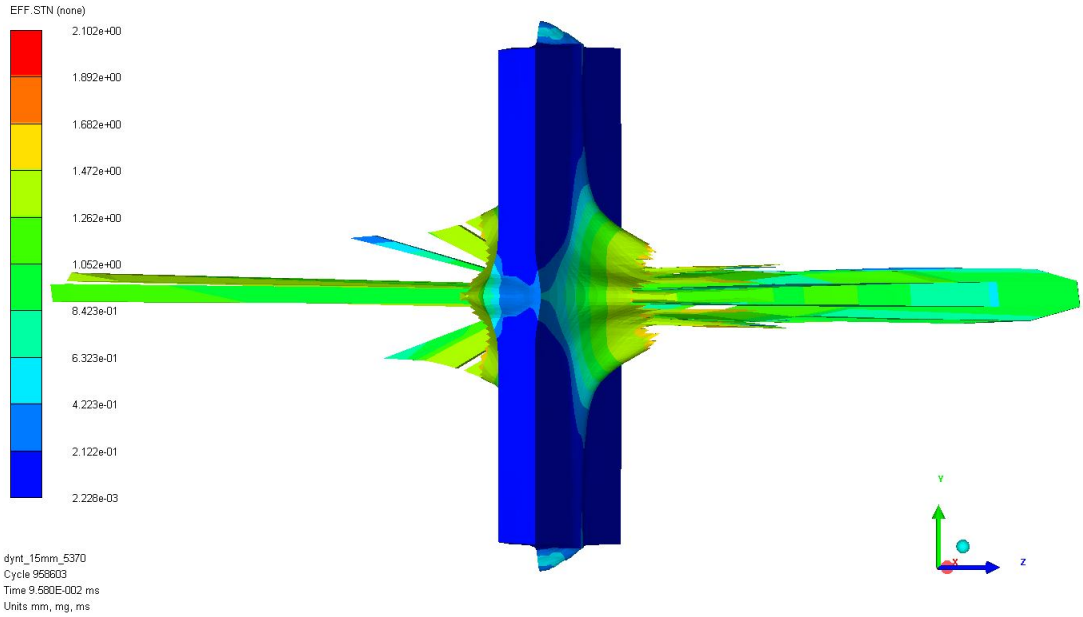


**Figure 9.17:** Illustration of the distribution of effective strain values using an element-based model in combination with the HB26T model proposed by Lässig et al. [8].

Second, for all these three cases, penetration was not satisfactorily captured. For all three cases, the main body of the impactor was present in or around the main body of the laminate at simulation termination. The debris plume more or less consists solely of target material. Figure 9.18 is indicative of this observation. Figure 9.18a is the full result of the impact simulation at time of termination. Figure 9.18b contains only the impactor at this point in time. Figure 9.18a and 9.18b are aligned to show the impactor location within the full simulation. Because of the modelling approach, it was found to be impossible to generate a cross-section of the model, necessitating this presentation approach. The impactor passed the rear face of the target plate by no more than 10 $mm$.

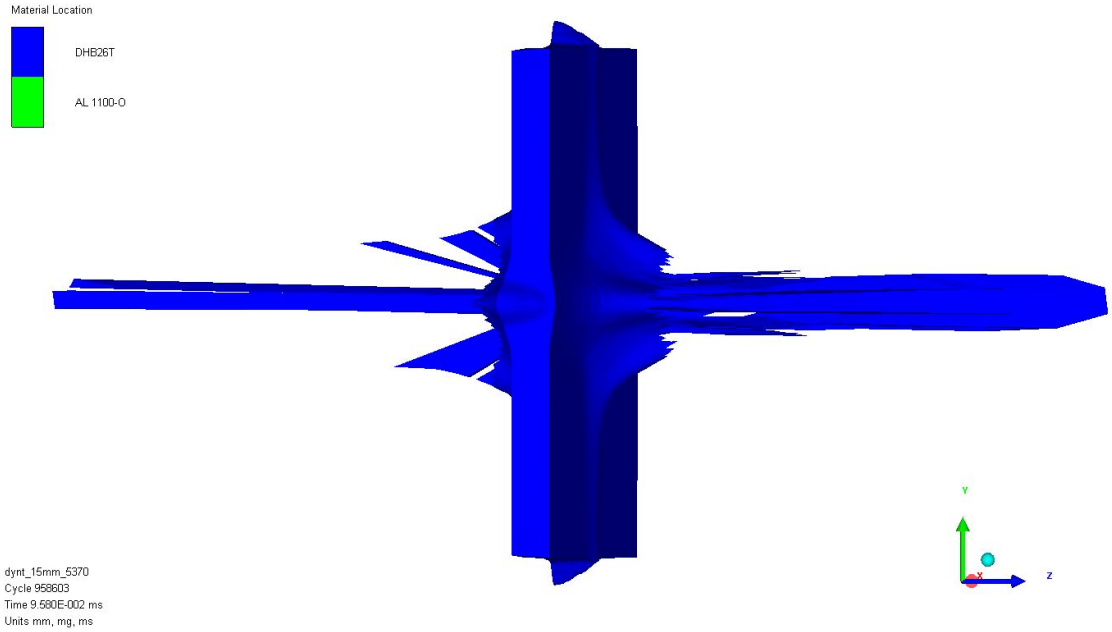


**(a)** Simulation still-shot.

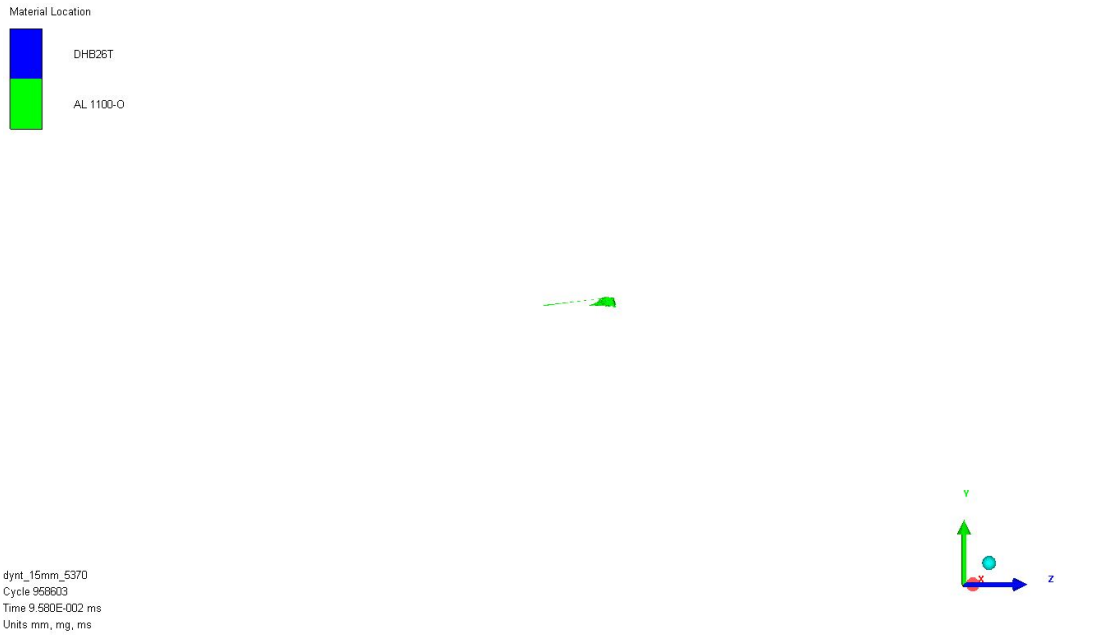


**(b)** Isolated Impactor.

**Figure 9.18:** Simulation result using HB26T for $V_0 = 5370\ m/s$ at $t = 0.958 \cdot 10^{-1}\ ms$ after impact.

The observations from this section serve as a potent illustration of the advantages of SPH-based discretisation for hypervelocity impact simulations. Firstly, Lagrangian element-

based formulations are prone to computational difficulties due to severe element distortion. Second, velocity data are, at least when using the geometric strain controlled erosion mechanism, measurement time dependent. Nguyen et al. [15] reported this problem is alleviated by using more sophisticated erosion models. For the HB26T model, though, elements will continue to absorb energy during their deformation up to erosion. Third, erosion itself is a process that is by its very definition physically accurate. The ANSYS® Mechanical User's Guide [87] warns that erosion should be used with caution. Fourth, comparing Figure 9.18 with Figure 9.7 it becomes apparent model HB26T does not capture the overall shape and experimental fragmentation behaviour. This is inherent to the use of standard Lagrangian formulations, since the formulation is not intended to capture fragmentation. Last, comparing Figure 9.18, 9.8 and 9.9 it becomes apparent that the models predict substantially different post-impact response of the impactor. Absent concrete experimental data on this part, it is not possible to conclusively say which model more closely represents reality.

Given these points, it stands to reason simulation data produced using HB26T cannot simply be used as a proxy for experimental validation. They will still be considered in Chapter 10. However, proper caution is required since this constitutes an extrapolation beyond the original validation range of the model.

# Chapter 10

# Effect of Target Thickness Variation

In this chapter, the change in model response brought about by reducing target AD is investigated. As mentioned in Chapter 9, no validation data were available for any of the cases considered in this chapter. This chapter will therefore mainly contain qualitative assessment of debris cloud shapes and comparisons between different material models.

The target AD considered in this chapter is the value of 9.4 $kg/m^2$ used for the KFRP model proposed by Clegg et al. [68] and used by Riedel et al. [69]. In Section 10.1, both DM1- and DM2-based simulations are discussed. Section 10.2 contains element-based simulations using the HB26T model. It also covers the comparison between the results from Section 10.1 and the results from the element-based simulations. A comparison between the proposed DM1 and DM2 models and the published KFRP model is then presented in Section 10.3. For all cases considered in this chapter, in-plane dimensions were kept at 200 $mm$ target width, the impactor diameter was kept at 6.0 $mm$ diameter.

## 10.1 Behaviour of DM1 and DM2 for 9.4 kg/m$^2$ Targets

The areal densidy of 9.4 $kg/m^2$ considered in this chapter was converted to a target thickness of 9.6 $mm$ for the DM1- and DM2-based simulations. For DM1-based simulations an overall smoothing length of 0.10 $mm$ was uses. For DM2-based simulations this was set to 0.15 $mm$. All impactor residual velocity data presented in this section are taken from within 15 $mm$ of the most forward positioned large concentration of impactor debris. This definition contains a certain degree of subjectivity, but given the problem of fragmentation, it was selected as the most reliable method. Comparable to what was done for the 15 $kg/m^2$ target AD, a series of different impactor velocity cases was considered, ranging from 3100 $m/s$ to 8000 $m/s$. Table 9.1 contains the considered impactor velocities and corresponding residual impactor velocities. Again, maximal debris cloud velocities that are thought to be related to excessive spallation and over-penetration are presented between brackets.

### $V_0$ = 3100 m/s Impact Case

From Figure 10.1, and considering these images alongside those from Figure 9.5 it can be seen that for the two considered cases, the response of DM1 is rather comparable. Note that for this case an impact velocity of 3100 $m/s$ is used, rather than the 3532 $m/s$ considered in Subsection 9.1.2. The use of a thinner target laminate most likely resulted

**Table 10.1:** Residual velocity values for the DM1 and DM2 models with $9.4\ kg/m^2$ AD targets. Values between brackets represent the peak velocity encountered in the composite debris cloud.

| $[m/s]$ | 3100 | 3532 | 4500 | 5370 | 6591 | 8000 |
|---|---|---|---|---|---|---|
| DM1 | 1050 (4500) | 1050 (4500) | 1850 (4400) | 2350 (3500) | 3750 (4250) | 4600 (5350) |
| DM2 | 1250 (2700) | 1550 (2400) | 2200 (3150) | 2800 (3500) | 3650 (4500) | 4400 (5300) |

in a comparable shock state in both the target and impactor when compared to the 15 $kg/m^2$, $V_0 = 3532\ m/s$ case.

Figure 10.1b shows a strongly fragmented impactor, which is not expected for this case. For the thicker laminate, both $V_0 = 3100\ m/s$ and $V_0 = 3532\ m/s$ experimental impact footage gave rise to the suspicion that the impactor retained significant cohesion post-impact. It is unlikely that a thinner target of the same material would have resulted in significant fragmentation in the impactor. Figure 10.1a again shows the excessive spallation.

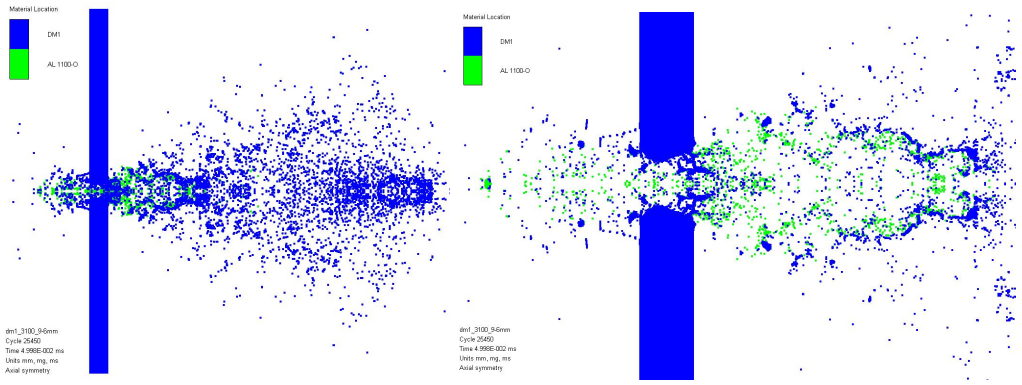


**(a)** Simulation still-shot.

**(b)** Enlarged image focussing on impactor fragments.

**Figure 10.1:** Simulated debris clouds using DM1 for $V_0 = 3100\ m/s$ at $t = 0.5 \cdot 10^{-1}\ ms$ after impact into a $9.6\ mm$ thick target.

Figure 10.2 indicates that the behaviour of DM2 appears to be similar for both considered laminate thicknesses. Again a relatively narrow debris trail is presented, combined with excessive spallation originating from the debris cloud tip.

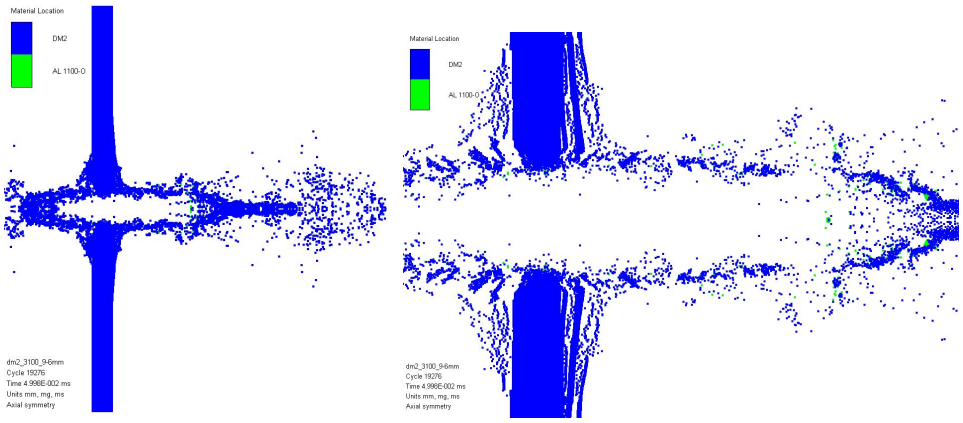


**(a)** Simulation still-shot. **(b)** Enlarged image focussing on impactor fragments.

**Figure 10.2:** Simulated debris clouds using DM2 for $V_0 = 3100\ m/s$ at $t = 0.5 \cdot 10^{-1}\ ms$ after impact into a $9.6\ mm$ thick target.

### $V_0$ = 4500 m/s Impact Case

As can be seen in Table 10.1, for DM1 an impact velocity of $V_0 = 4500\ m/s$ marks the threshold were nearly the complete impact process takes place in the hypervelocity range. The residual velocity of $1850\ m/s$ mentioned here was recorded at the large aluminium concentration at the far right in Figure 10.3b. This concentration may represent a mostly intact impactor. This seems feasible for this velocity-AD combination, since for the $15\ kg/m^2$, $V_0 = 3532\ m/s$ case the impactor was also expected to remain concentrated in the tip of the debris cloud.

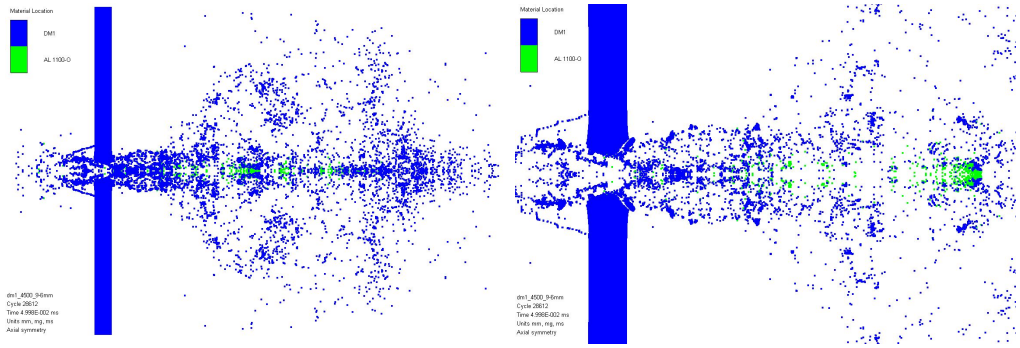


**(a)** Simulation still-shot. **(b)** Enlarged image focussing on impactor fragments.

**Figure 10.3:** Simulated debris clouds using DM1 for $V_0 = 4500\ m/s$ at $t = 0.5 \cdot 10^{-1}\ ms$ after impact into a $9.6\ mm$ thick target.

Figure 10.4 suggests that at higher impact velocities the linear debris cloud propagation behaviour is maintained. In cloud shape and residual velocity, the case considered here is quite comparable to the 15 $kg/m^2$, $V_0 = 6591$ $m/s$ case. Consulting Table 10.1, it can be seen that for this case, the residual velocities of the impactor for DM1 and DM2 are within 20% of one another. Both models also predict the impactor remains mostly concentrated after penetration.

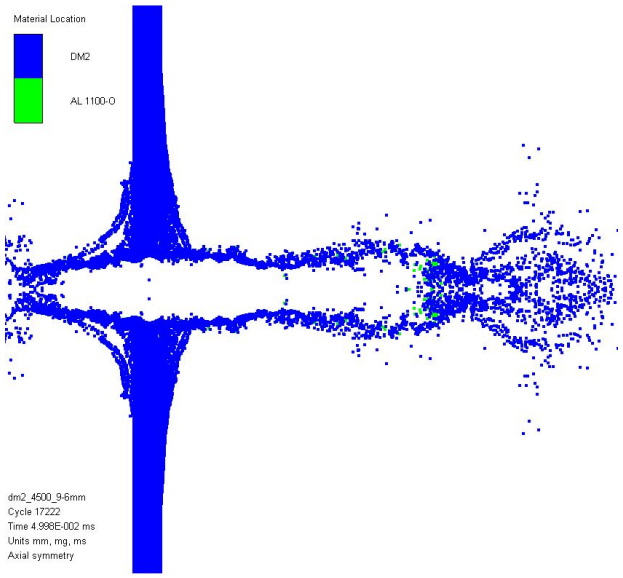


**Figure 10.4:** Simulated debris clouds using DM2 for $V_0 = 4500$ $m/s$ at $t = 0.5 \cdot 10^{-1}$ $ms$ after impact into a 9.6 $mm$ thick target.

### $V_0$ = 6591 m/s Impact Case

Because excessive spallation in the simulations became decreasingly pronounced as impact velocity increased, the decision was made to omit the enlarged images used before. Instead, a side-by-side representation of the simulation results obtained using DM1 and DM2 under a 6591 $m/s$ impact are presented in Figure 10.5. The simulation results from DM1, presented in Figure 10.5a appear to be somewhat messier than those from DM2. The debris cloud predicted by DM2 appears to have become somewhat wider compared to the case depicted in Figure 10.4. Comparing Figure 10.5a to Figure 10.5b, it can be seen that the general shape of the leading edge of the debris cloud, and particularly of the impactor material shows similarities. Predicted residual velocities are also close, as presented in Table 10.1.

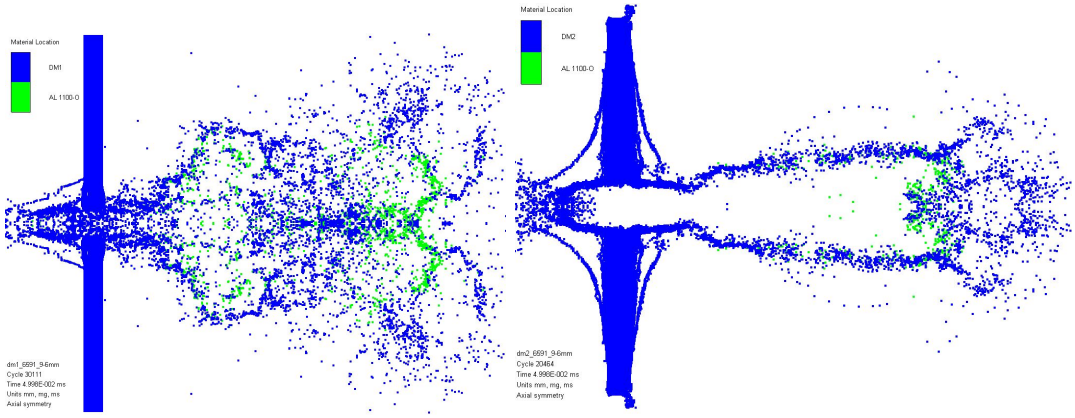

**(a)** DM1. **(b)** DM2.

**Figure 10.5:** Simulated debris clouds for $V_0 = 6591\ m/s$ at $t = 0.5 \cdot 10^{-1}\ ms$ after impact into a $9.6\ mm$ thick target.

### $V_0$ = 8000 m/s Impact Case

Figure 10.6 presents simulation results for both DM1 and DM2 under a simulated $V_0 = 8000\ m/s$ impact. Figure 10.6a shows that DM1 again experiences a slight tendency towards over-penetration at the leading edge of the debris cloud, as was the case for the 15 $kg/m^2$, $V_0 = 6591\ m/s$ case. DM1 can also be seen to predict a larger scatter of impactor material within the debris cloud than DM2.

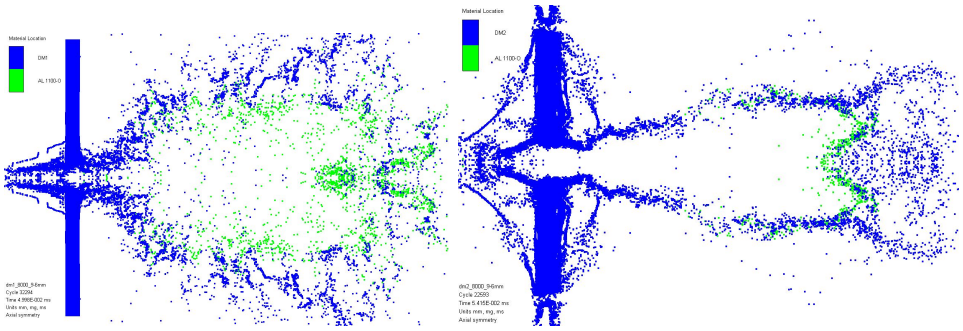

**(a)** DM1. **(b)** DM2.

**Figure 10.6:** Simulated debris clouds for $V_0 = 8000\ m/s$ at $t = 0.5 \cdot 10^{-1}\ ms$ after impact into a $9.6\ mm$ thick target.

### Reflection on Target AD Reduction

Absent validation data for the cases considered in this Section, it is impossible to make definitive statements as to the accuracy of the presented results. A good match between simulated and experimental residual velocity data was found for DM2 in Chapter 9.

Assuming this match extends to the reduced AD case considered in this chapter, DM2 residual velocity data were taken as a first benchmark. From $V_0 = 4500\ m/s$ upwards main debris cloud velocities for both DM1 and DM2 were found to remain within approximately 20% of one another. DM1 maintained its tendency to produce debris clouds that displayed more radial expansion than those produced by DM2.

For the reduced thickness targets, DM1 still appears to have trouble capturing elements of lower velocity impacts, suffering from excessive impactor fragmentation and displaying excessive spallation. However, for impact velocities between 4500 $m/s$ and 8000 $m/s$, Figure 10.3 to Figure 10.6 indicate that model behaviour matches more closely than has been observed for the 15 $kg/m^2$ target case.

## 10.2 Comparison to 9.4 kg/m$^2$ HB26T Targets

The target centre is meshed with 50 x 50 x 10 elements that are 0.96 $mm$ in all directions. This was done to ensure the through-thickness element resolution remains the same as used by Lässig et al. [8]. The total target contains 70 elements in $x$- and $y$-directions respectively. For the impactor, 6 elements were used through the radius. Table 10.2 presents the residual velocities found for the considered impact cases using the element-based HB26T model. The presented values are the maximum residual velocity values found for the impactor. The values between brackets represent the maximal velocity encountered in the HB26T. All simulations were set to run for $1.0 \cdot 10^{-1}\ ms$. The times at which the simulations self-aborted are also presented in Table 10.2. This underlines that for none of the considered cases the simulation could run to the prescribed end time.

**Table 10.2:** Residual velocity values for element-based HB26T model and SPH-based DM1 and DM2 simulations with 9.4 $kg/m^2$ AD targets. Values between brackets represent the peak velocity encountered in the composite debris cloud.

| $[m/s]$ | 3100 | 3532 | 4500 | 5370 | 6591 | 8000 |
|---|---|---|---|---|---|---|
| HB26T | 1150 | 1450 | 2050 | 2800 | 4000 | 4700 |
| | (2950) | (3000) | (3850) | (4050) | (5300) | (5450) |
| End time $[10^{-1}\ ms]$ | 0.231 | 0.233 | 0.399 | 0.525 | 0.0975 | 0.543 |
| DM1 | 1050 | 1050 | 1850 | 2350 | 3750 | 4600 |
| | (4500) | (4500) | (4400) | (3500) | (4250) | (5350) |
| DM2 | 1250 | 1550 | 2200 | 2800 | 3650 | 4400 |
| | (2700) | (2400) | (3150) | (3500) | (4500) | (5300) |

Table 10.2 also contains the simulation results for the SPH-based simulations already presented in Table 10.1, to facilitate comparison of the values. Note that for DM1 and DM2 the velocities were measured at $t = 1.0 \cdot 10^{-1}$, which constituted the end of the prescribed simulation time. For the SPH-based simulations, particle velocities were found to hardly change once the penetration process was fully completed. Velocity data

presented for HB26T were obtained at the last available simulation time. For the HB26T element-based model the residual velocity is not constant in time, even after penetration is completed. Measurements at later points in time might therefore have yielded lower residual velocities for HB26T simulations.

Nonetheless, Table 10.2 indicates that quite good agreement exists between the element- and SPH-based simulation models. Especially between HB26T and DM2, the overall resulting difference in predicted impactor residual velocity can be seen to remain within 10%. The match between the simulation results for the three considered cases supports the proposed DM1 and DM2 models.

## 10.3 Comparison to 9.4 kg/m$^2$ KFRP Targets

For the KFRP material model, the same three impact velocities used in Section 9.2 were considered. These being $V_0 = 3532\ m/s$, $V_0 = 5370\ m/s$ and $V_0 = 6591\ m/s$. Target thickness was set at 5.7 $mm$, conform [69]. Figure 10.7 and 10.8 present simulation results for the $V_0 = 3532\ m/s$ and $V_0 = 6591\ m/s$ impact case respectively. Figure 10.7b clearly shows a large impactor fragment surviving past penetration, as was also the case for the equal AD and velocity simulations using DM1. Figure 10.7a furthermore shows significant spallation.

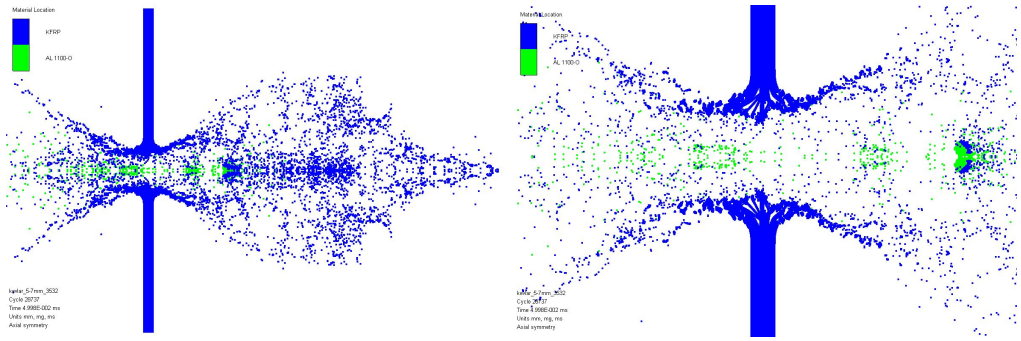

**(a)** Simulation still-shot.

**(b)** Enlarged image focussing on impactor fragments.

**Figure 10.7:** Simulated KFRP debris clouds for $V_0 = 3532\ m/s$ at $t = 0.5 \cdot 10^{-1}\ ms$ after impact into a 9.6 $mm$ thick target.

Figure 10.8a clearly shows the debris cloud halo that was encountered in the experimental validation footage presented in Figure 9.7 and Figure 9.10, but could not be captured by either DM1 or DM2. The impactor fragments appear to be mostly concentrated at the centre of the debris cloud for the simulated case. Absent experimental validation footage, it is not possible to say how closely these simulations represent the physical process.

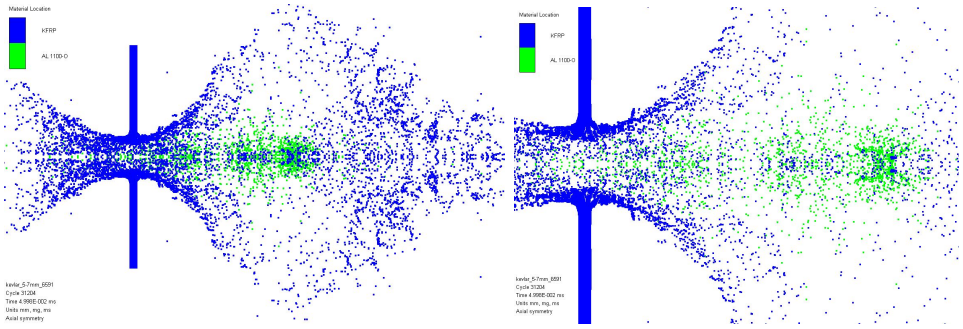

**(a)** Simulation still-shot.

**(b)** Enlarged image focussing on impactor fragments.

**Figure 10.8:** Simulated KFRP debris clouds for $V_0 = 6591\ m/s$ at $t = 0.5 \cdot 10^{-1}\ ms$ after impact into a $9.6\ mm$ thick target.

A summary of the post-impact linear momentum in $x$-direction of the impactor for both $9.6\ mm$ DM1 and DM2 and $5.7\ mm$ KFRP targets is presented in Table 10.3. Residual momentum values obtained from impact simulations into KFRP were found to consistently be below those predicted by both DM1 and DM2. For the $V_0 = 3532\ m/s$ case, the value even became negative, signifying a significant part of the impactor debris achieved large negative velocities.

Based solely on the data presented in Table 10.3, it would appear that, under direct hypervelocity impact conditions, the Kevlar®-epoxy material which the KFRP model represents should be expected to be better slowing down an impactor than the considered Dyneema® HB26. However, given the validation basis available, such statements would be premature. The cases considered here are also all direct hypervelocity impacts of monolithic impactors. As was pointed out in Subsection 3.4.1, low density ballistic composites should ideally not be used as outer bumper from a ballistics point of view. Performance within an SWS, as would be used aboard a spacecraft, is not yet considered here.

**Table 10.3:** Residual $x$-momentum values of the impactor for the DM1, DM2 and KFRP models with $9.4\ kg/m^2$ AD targets.

| $[m/s]$ | 3532 | 5370 | 6591 |
|---|---|---|---|
| $p_{x0}\ [kg \cdot m/s]$ | 1.06 | 1.61 | 1.97 |
| DM1 $[kg \cdot m/s]$ | 0.184 | 0.423 | 0.595 |
| DM2 $[kg \cdot m/s]$ | 0.244 | 0.535 | 0.730 |
| KFRP $[kg \cdot m/s]$ | -0.081 | 0.291 | 0.528 |

It should also be pointed out that, the Kevlar®-epoxy and Dyneema® HB26 composites are very different in nature. The former is a stiff laminate with a fibre volume fraction of 60% and an epoxy matrix. The latter is a flexible ballistic composite with a fibre volume fraction of 83% and a polyurethane matrix.

For proper comparison between various fibre-based ballistic protection systems for spacecraft, ideally a different kind of investigation would be required than has been possible within the scope of this project. For ideal comparison, one would need to create various ballistic composites with similar structural properties. So either stiff or flexible. If comparison of different fibre reinforcement systems is the goal, one should also attempt to get fibre volume fractions either as close to each other as possible, or as high as possible for each considered composite. Side-by-side comparison of equal AD impact experiments on bare composites and composites placed inside SWS configurations could then be used to filter out as many non-fibre-related influences on ballistic performance as possible.

Ideally, such investigations should not only be limited to Kevlar® and Dyneema® based composites, but should also encompass other high-strength ballistic fibres such as PIPD and PBO [10]. As advocated earlier, these kinds of experimental campaigns should be combined with consistent material characterisation and numerical modelling efforts. This approach would yield a comprehensive dataset and a thorough understanding of the effects of various fibre properties on hypervelocity impact response of fibre reinforced composites.

# Chapter 11

# Sensitivity Study of Proposed Dyneema® Models

In this chapter, the sensitivity of DM1 and DM2 to variations in their material input data are investigated. The goal of this step is to help assess whether observed model responses are stable, or whether observed phenomena occur due to particular numerical value choices or combinations of parameters. All test cases in this chapter were performed on 15 $kg/m^2$ targets, because of the availability of experimental reference data. The $V_0 = 6591$ $m/s$ scenario was always used as primary case. This was done to allow for consistency between various cases. This was also the experimental impact scenario that displayed the most complex debris cloud shape, and the numerical case with the most curious anomaly. Namely the over-penetration of the impactor at the front of the debris could.

For several variation cases it was observed that only minimal changes in the shape of the overall debris cloud occurred. This does not mean that the two simulation cases yielded identical results. Generally changes in the debris cloud peak velocity and residual velocities of the impactor were obtained. For may cases, variations in these already difficult to quantify output quantities were relatively small. Moreover, given the uncertainties regarding the internal debris cloud structures and the lack of repetition of experiments at specific impact velocities, it is often not possible to adequately determine whether changes in the impactor fragmentation response are significant. This broader statement is believed to better capture the nature of the observed variations.

## 11.1 Sensitivity Study for DM1

In this section, the stability of the simulation results obtained using DM1 under perturbation of several of its model components is investigated. Perturbations in the Orthotropic Yield and Orthotropic Softening models are considered, and the influence of the used Maximum velocity setting was investigated.

### 11.1.1 Increased Through-Thickness Shear Yielding

For DM1, the through-thickness shear response was based on data obtained from Lässig et al. [93]. For the perturbed case, the curves reported by Ruiz-Ripoll et al. [88] were

used as input. As indicated in Section 7.1, figures from that publication will not be used in this report. Setting the $a_{55}$ and $a_{66}$ parameters of the Orthotropic Yield model to 1550 produced a through-thickness shear yield curve more in line with failure strains reported by Ruiz-Ripoll et al. [88]. It was noted that by doing so, the compressive through-thickness material response changed as presented in Figure 11.1. The resulting through-thickness shear stress-strain plot is not presented here, as discussed with Dr. Nguyen [91].

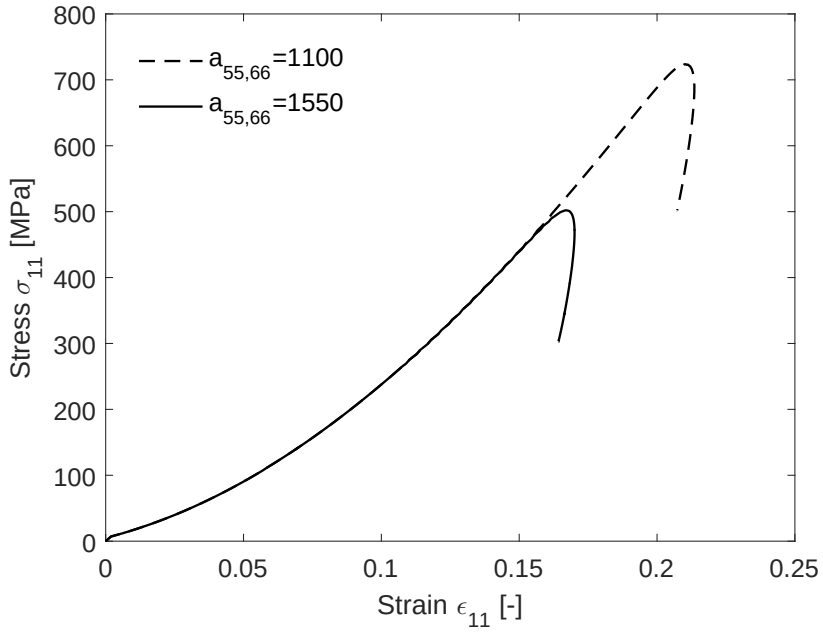


**Figure 11.1:** Through-thickness compressive unit test for DM1 with $a_{55} = a_{66} = 1100$ and $a_{55} = a_{66} = 1550$.

Figure 11.2 presents the results of simulations with $V_0 = 3532\ m/s$ using the modified through-thickness shear strength. This can be compared to experimental footage presented in Figure 9.4 and simulation results obtained using DM1, presented in Figure 9.4. Figure 11.2a shows that the overall shape of the forward debris cloud is relatively unaffected when compared to the original DM1 case presented in Figure 9.5a. Focussing on the impactor debris, though, one main difference was observed compared to DM1. Looking at Figure 11.2b, it was found that for the modified case the impactor was far less fragmented post-impact than was predicted by DM1. The average residual $x$-velocity was approximately 0 $m/s$. For this test case, using DM1, far more impactor fragmentation was predicted. For the original model a larger degree of penetration was observed. Here the average residual impactor velocity was approximately 100 $m/s$.

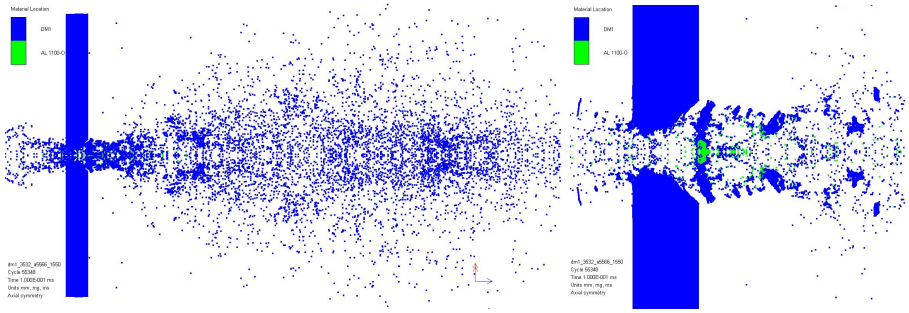

**(a)** Simulation still-shot. **(b)** Impact site enlarged.

**Figure 11.2:** Simulated debris clouds using DM1 with $a_{55} = a_{66} = 1550$ for $V_0 = 3532\ m/s$ at $t = 1.0 \cdot 10^{-1}\ ms$ after impact.

Figure 11.3 presents a side-by-side depiction of $V_0 = 5370\ m/s$ impact simulations using the modified and original DM1 model. For the case with the modified through-thickness shear behaviour, depicted in Figure 11.3a, it was found excessive spallation decreased. The residual velocity at the front of the main debris cloud increased from approximately 1700 $m/s$ to approximately 2000 $m/s$. However, it should be noted that for the modified model this also constitutes the peak debris cloud velocity. For the DM1-based simulation excessive spallation drove this peak value op to almost 3000 $m/s$. The peak residual velocity of the larger impactor fragments was also found to increase from about 900 $m/s$ for DM1 to about 1400 $m/s$ for the modified case.

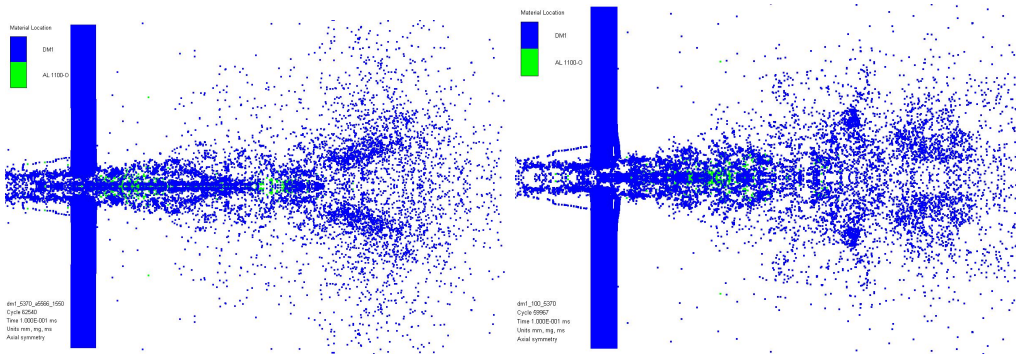

**(a)** $a_{55} = a_{66} = 1550$. **(b)** DM1.

**Figure 11.3:** Simulated debris clouds using DM1 and modified DM1 with $a_{55} = a_{66} = 1550$ for $V_0 = 5370\ m/s$ at $t = 1.0 \cdot 10^{-1}\ ms$ after impact.

Figure 11.4 presents a side-by-side depiction of $V_0 = 6591\ m/s$ impact simulations using the modified and original DM1 model. As can be seen from Figure 11.4a, increasing $a_{55}$ and $a_{66}$ has reduced, but not removed the tendency of over-penetration of DM1. The velocity at the front of the debris cloud was found to be approximately 2800 $m/s$, whilst the peak velocity at the front of the main body of the debris cloud was around

2500 $m/s$. The peak velocity of the larger impactor based debris fragments was found to be reduced to approximately 2000 $m/s$, rather than the value of 3500 $m/s$ found for the over-penetrating material for DM1.

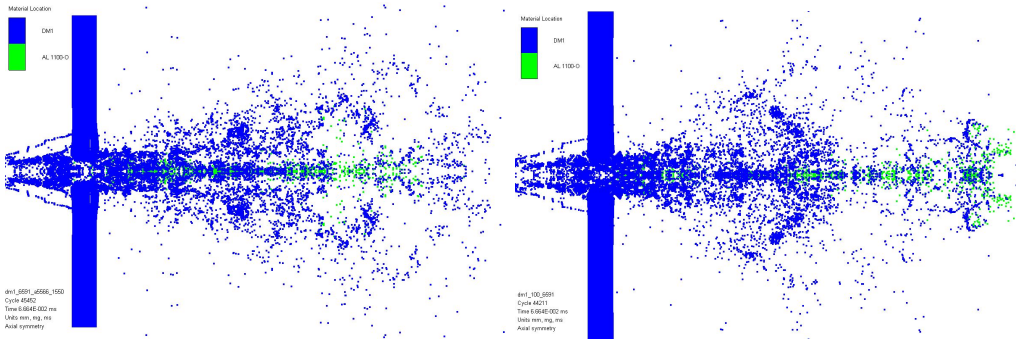

**(a)** $a_{55} = a_{66} = 1550$. **(b)** DM1.

**Figure 11.4:** Simulated debris clouds using DM1 and modified DM1 with $a_{55} = a_{66} = 1550$ for $V_0 = 6591\ m/s$ at $t = 0.67 \cdot 10^{-1}\ ms$ after impact.

### 11.1.2 Varying Orthotropic Yield Model

For the Orthotropic Yield criterion, the apparent importance of the $a_{11}$ parameter has already been illustrated in Subsection 7.1.2. The effect of changing $a_{55}$ and $a_{66}$ is illustrated in Subsection 11.1.1. The importance of correct selection of the master curve is illustrated in Chapter 6 and Chapter 7. This leaves the importance of the in-plane tension ($a_{22}$ and $a_{33}$) and shear ($a_{44}$) model response to be addressed.

#### Varying $a_{44}$

To assess the impact of changing the in-plane model response of DM1, two cases were considered. Using a constant impact velocity of $V_0 = 6591\ m/s$, targets were simulated with the $a_{44}$ parameter halved and doubled respectively. Neither operation significantly changed either the impactor residual velocity nor the overall debris cloud shape as compared to the pristine DM1 simulation. This insensitivity of DM1 to changes in its in-plane shear response also partially justifies the reduction of the in-plane shear from DM0 to DM1 discussed in Section 7.1.2.

#### Varying $a_{22}$ and $a_{33}$

Sensitivity of DM1 to changes in its in-plane tensile stress-strain response was assessed by considering two cases. Using a constant impact velocity of $V_0 = 6591\ m/s$, targets were simulated with both the $a_{22}$ and $a_{33}$ parameter decreased and increased by 20%. Reducing the $a$ parameters to 0.8 lead to a steeper stress strain curve, resulting in a lower strain at failure. This resulted in over-penetration of the target, as was the case

for the pristine DM1 model. This case is illustrated in Figure 11.5a. Increasing the $a$ parameters to 1.2 had the opposite effect, and actually ensured bulk impactor residual velocities did not rise above 2400 $m/s$. The resulting debris cloud is presented in Figure 11.5b.

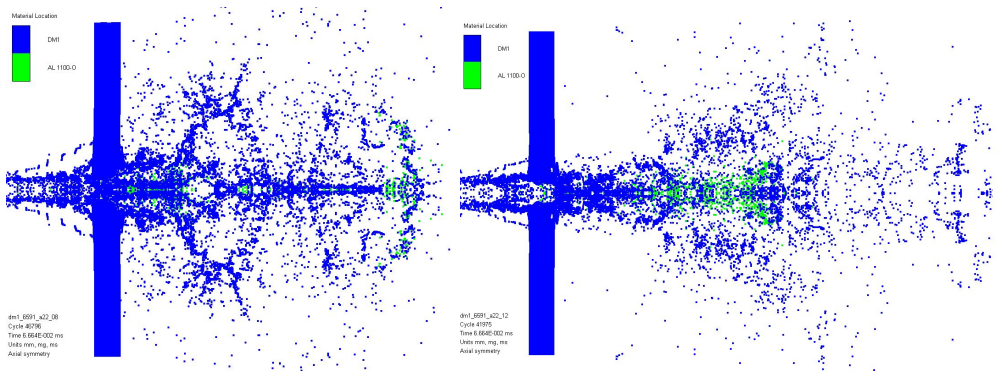

**(a)** $a_{22} = a_{33} = 0.8$. **(b)** $a_{22} = a_{33} = 1.2$.

**Figure 11.5:** Simulation results of a $V_0 = 6591\ m/s$ impact using DM1 at $t = 0.67 \cdot 10^{-1}\ ms$ after impact under varying $a_{22}$ and $a_{33}$.

The experimental maximum residual velocity for this case was 2457 $m/s$ [8]. In Subsection 3.4.1 it was asserted that material strength is not driving in the ballistic performance of outer bumpers. This was supported by the observations for aluminium on aluminium impact simulation presented in Subsection 5.2.2. The simulated test cases considered in the current subsubsection indicate that predicted residual velocities obtained using DM1 are sensitive to changes in in-plane material stiffness. Whether changes to in-plane and out-of plane material strength do affect the model response of DM1 is discussed in Subsection 11.1.3.

### 11.1.3 Varying Material Strength Values

All sensitivity tests in this subsection were performed using a constant impact velocity of $V_0 = 6591\ m/s$ and an AD of 15 $kg/m^2$. Each variation case will consist of the relevant parameters being reduced and increased using a consistent factor.

#### Varying In-Plane Tensile Strength

The tensile strength in both 22- and 33-directions was reduced and increased by 25%. Both of these cases lead to the removal of the excessive penetration encountered for the pristine DM1 model. Peak velocities for impactor based debris fragments remained below 2500 $m/s$ and 2000 $m/s$ respectively for these cases. The resulting changes in debris cloud geometry can be observed in Figure 11.6a and Figure 11.6b for the reduced and increased in-plane strength case respectively.

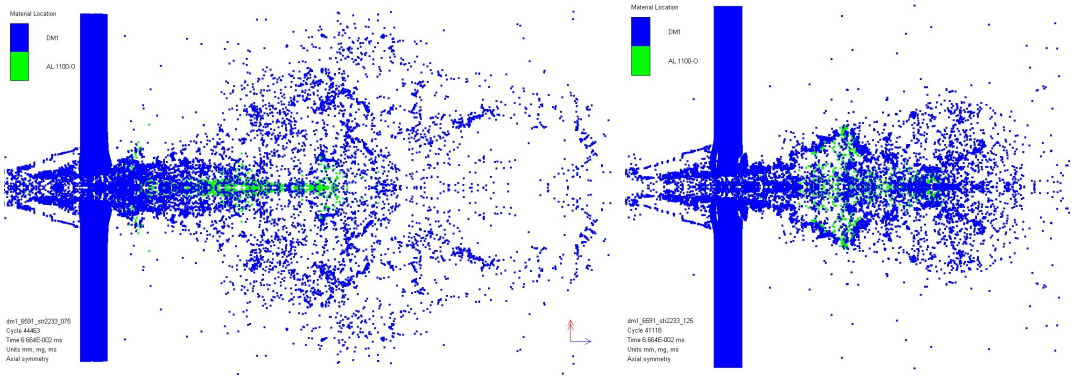

**(a)** Tensile Failure Stress 22 and 33 are 862.5 $MPa$. **(b)** Tensile Failure Stress 22 and 33 are 1437.5 $MPa$.

**Figure 11.6:** Simulation results of a $V_0 = 6591\ m/s$ impact using DM1 at $t = 0.67 \cdot 10^{-1}\ ms$ after impact under varying in-plane strength.

### Varying Through-Thickness Tensile Strength

For the considered cases, the tensile strength the 11-direction was halved to 22.5 $MPa$ and doubled to 90 $MPa$. Note that through the coupling between through-thickness tensile and shear strength described by Nguyen et al. [73], this should also be expected to influence through-thickness shear strength. For the case with reduced strength, general loss of cohesion was encountered between regions of the target plate. Reducing spall strength should be expected to have this effect. The resulting spallation was partially directed vertically, as is illustrated in Figure 11.7a. Increasing the through-thickness strength removed most of the observed over-penetration, but individual aluminium particles in the front of the cloud still reached velocities of around 3000 $m/s$ as can be seen in Figure 11.7b.

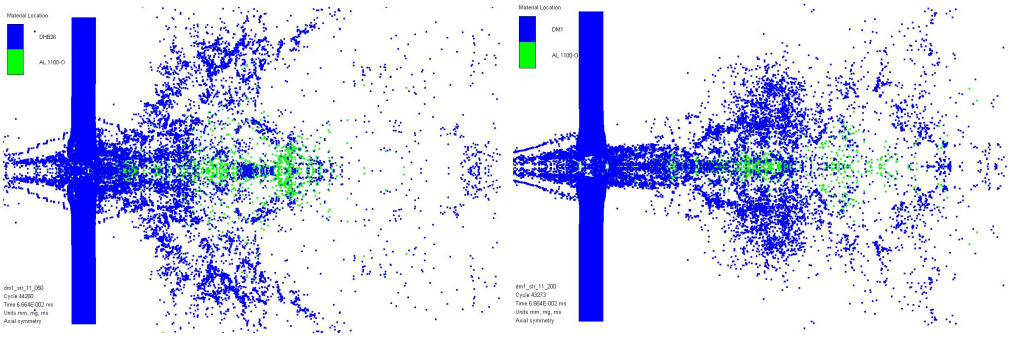

**(a)** Tensile Failure Stress 11 is 22.5 $MPa$. **(b)** Tensile Failure Stress 11 is 90 $MPa$.

**Figure 11.7:** Simulation results of a $V_0 = 6591\ m/s$ impact using DM1 at $t = 0.67 \cdot 10^{-1}\ ms$ after impact under varying through-thickness strength.

#### Varying Through-Thickness Shear Strength

Maximal shear strength in both 12 and 31 direction was halved to 78 $MPa$ for one case and doubled to 312 $MPa$ for the other. For both cases, this means the ultimate shear strength is above the value of 47.5 $MPa$ that signifies shear failure for the material model as presented in Figure 7.3. So changing this shear stress should not affect material performance. However, for both considered cases the over-penetration encountered for the pristine DM1 model disappeared.

The residual $x$-momentum of the impactor for the regular DM1 model was also found to be higher than that for both the case with the reduced and increased shear strength. Measured at $1.0 \cdot 10^{-1}$ $ms$ after impact, a value of 0.29 $kg \cdot m/s$ was obtained for pristine DM1 and values of 0.23 $kg \cdot m/s$ and 0.14 $kg \cdot m/s$ were found for the case with the reduces and increased strength respectively. The pre-impact $x$-momentum of the impactor for these cases is 1.97 $kg \cdot m/s$, which means the scatter stays within 10% of the initial value. The overall shape of the debris cloud remained similar for the three considered cases.

### 11.1.4 Varying Damage Coupling Coefficient

The damage coupling coefficient in DM1 was set to a value of 0.5, in line with the value used by Lässig et al. This value was changed to 0 and 1.0 for these test cases. An impact velocity of 6591 $m/s$was considered. For both cases it was found that the original problem for over-penetration for this case seized. Setting $C$ to 0 caused to result in significant excessive spallation. Setting $C$ to 1 yielded minimal change to the overall debris cloud shape. This case was further also implemented cases with initial impact velocities of $V_0 = 5370$ $m/s$, $V_0 = 3532$ $m/s$, $V_0 = 3100$ $m/s$, $V_0 = 2453$ $m/s$and $V_0 = 2052$ $m/s$. The overall shape of the debris cloud was hardly affected by this variation.

### 11.1.5 Varying Maximal Particle Velocity

For all SPH based simulations, the Maximum velocity was set to about 1.5 times the impactor velocity. This prevented particles from reaching essentially unbound velocities, ensuring physical consistency and preventing most time-step related complications. To test model sensitivity to this assumption, simulations were performed with the Maximum velocity set to the impactor velocity. For the $V_0 = 6591$ $m/s$, this variation resulted in the impactor over-penetration no longer occurring. The general shape of the debris cloud remained unaffected. For $V_0 = 3532$ $m/s$, $V_0 = 3100$ $m/s$, $V_0 = 2453$ $m/s$and $V_0 = 2052$ $m/s$, the overall shape of the debris cloud was found to remain largely unaffected.

### 11.1.6 Overall Reflection on the Sensitivity of DM1

In this section, model sensitivity studies were mainly performed using an initial impactor velocity of 6591 $m/s$. This was done because for this case the most complex

debris cloud shape was obtained experimentally [8] and because for this case the overall agreement between the experimental and numerical data was found to be closest. Testing model sensitivity for more velocity cases, and particularly for various target ADs is recommended. Overall it was found that the debris cloud shape was quite stable under parameter variation. It was also found that the over-penetration found for the the $V_0 = 6591\ m/s$ impact case was most likely the consequence of a very specific subset of parameters. In-plane and through-thickness tensile strength and plastic stiffness and through-thickness plastic shear stiffness were found to have particularly strong effects here, but most model perturbations removed the phenomenon nearly all together. Through-thickness shear strength was found to have an unexpected effect on impactor penetration behaviour, where both increasing and decreasing its value prevented over-penetration. This happened despite the fact that unit testing on Lagrangian elements predicted both alternative strength values were in a range the model would be unable to achieve in the first way.

Throughout this study, it was found that the orthotropic material models in Autodyn tend to have complex internal interactions. It is also expected that combining this with an SPH discretisation in thick targets introduces a certain degree of complexity to impact simulations in general.

## 11.2 Sensitivity Study for DM2

The material sub-models used in DM2 are relatively simple, compared to DM1. Consequently, since there were fewer input parameters, fewer sensitivity tests were required. Two model components were identified that required testing of model sensitivity to input variation. These where the yield stress used by the Von Mises strength criterion and the through-thickness tensile strength used by the Material Stress Failure criterion.

### 11.2.1 Increased Yield Strength

Since the main loading direction during impact is in the through-thickness direction, the yield stress originally selected for the Von Mises yield criterion was estimated based on through-thickness shear test data [88]. Due to the orthotropic nature of the considered material, various different yield stress values can be defined for the different loading directions. Testing of the effect of increasing the yield strength to a value more in line with yielding in the in-plane tension direction was undertaken. The Yield Stress input value was increased from $1.0 \cdot 10^4\ kPa$ to a value of $1.5 \cdot 10^5\ kPa$ [92].

Two test cases were considered. AD was set to 15 $kg/m^2$. $V_0$ was set to 3100 $m/s$ and 6591 $m/s$ respectively, since these values represent the lowest and highest available data points for which penetration was observed. For both considered cases, no significant changes were encountered in either debris cloud shape or impactor residual velocity.

### 11.2.2 Increased Through-Thickness Tensile Strength

The second main variable for which significant uncertainty existed was the through-thickness tensile strength. The value of 45 $MPa$ was taken from the KFRP model presented by Clegg et al. [68]. For their CFRP model, Wicklein et al. [70] used a value of 245.7 $MPa$. The effect of increasing the tensile strength in 11 direction to the latter value was investigated. Again, AD was set to 15 $kg/m^2$ and $V_0$ was set to 3100 $m/s$ and 6591 $m/s$. For both considered cases, no significant changes were encountered in either debris cloud shape or impactor residual velocity. This can be explained by the fact that, in case of successful penetration, the process is mostly driven by through-thickness compression and shearing.

### 11.2.3 Overall Reflection on the Sensitivity of DM2

The DM2 model appears to be quite stable in its predictive capabilities under the most logical parameter input variations. DM2 was found to be insensitive to increases in either the yield stress and through-thickness tensile strength. This further supports the hypothesis that the complex nature of the DM1 model is in part responsible for any observed model sensitivities.

# Chapter 12

# Simulated Stuffed Whipple Shield Configurations

In this chapter, the two proposed models for Dyneema® HB26 and the reported model for Kevlar®-epoxy are combined with aluminium models to create simulated SWS configurations. The component dimensions were based on the ISS Columbus module [82] and simulations as described by Clegg et al. [68]. Over the course of this project, the overall focus has shifted towards the formulation and validation of SPH compatible hypervelocity impact models for the Dyneema® HB26 ballistic composite. As a consequence, the initially intended extensive numerical comparison study between Kevlar®- and Dyneema®-based SWS configurations gradually started to fall outside its scope. This chapter focusses on the demonstration of the intended simulation configuration, and provides a first indicative result. However, only one impactor-target configuration combination was considered for one impact velocity. Further variation of this impactor-target configuration combination and if possible, experimental validation of the SWS simulations are recommended.

## 12.1 Dimensions and Configurations

All reported $y$-dimensions should be doubled, since the sketches outlined in this section were rotated around the $x$-axis. Unlike in previous chapters, figures containing simulation still-shots will not be presented mirrored in the $x$-axis because of image size. The outer bumper was modelled as an Al 6061-T6 rectangle with a thickness of 2.5 $mm$ and a $y$-dimension of 100 $mm$. The stuffing layer was modelled as rectangles with a $y$-dimension of 200 $mm$. The front (impacted) face was placed 70 $mm$ behind the rear face of the outer bumper. The used thickness was either 9.6 $mm$ for DM1 or DM2 models, or 5.7 $mm$ for KFRP models. The impactor and first two bumpers were modelled using an SPH discretisation. For DM1 and KFRP based models, smoothing lengths of h=0.10 $mm$ were used. For DM2 based models, smoothing lengths of h=0.15 $mm$ were selected. The impactor was modelled as half an Al 1100-O sphere with a diameter of 6.0 $mm$.

The rear wall was modelled as an Al 2024-T4, 200 $mm$ high, 4.75 $mm$ thick rectangle. Its front face was placed 120 $mm$ from the rear face of the outer bumper. Discretisation was performed using Lagrangian elements. At the plate bottom (so at the middle of the mirrored plate), an element size of 0.2375 mm was used, which is close to the 0.25 $mm$

used by Clegg et al. [68]. This results in a 20 elements through-thickness resolution. This element size was maintained in $y$-direction for 235 elements. A total of 300 elements was used in $y$-direction.

## 12.2 Boundary Conditions and Test Cases

The boundary condition used for the SWS configuration are in line with those used for target plates throughout this work. This means both metallic walls were constrained using boundary conditions at their outer-most row of particles/nodes setting velocity in both $x$- and $y$-directions to zero. For the composite walls, the top row of particles was prevented from moving in $x$-direction only. The impactors were given an initial velocity of 6591 $m/s$. Maximal particle velocities were set at 10000 $m/s$.

## 12.3 Simulation Results

Using these settings, for all three cases, the impactor penetrated the outer wall and fragmented. The resulting primary debris cloud then struck the stuffing layers. For the simulated set-up containing DM2, the model performed as expected after this point. The primary debris cloud impacted the front face of the stuffing layer, followed by reversal of the primary debris cloud and fragmentation of the stuffing layer. This secondary debris cloud struck the rear wall and no penetration occurred. This indicates the considered impactor velocity was bellow the ballistic limit of the configuration for the used impactor diameter. Simulation results are presented in Figure 12.1.

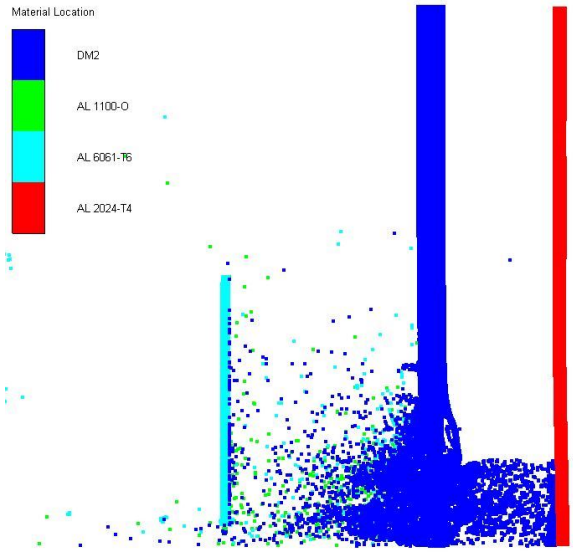


**Figure 12.1:** Simulated impact in a DM2-based SWS configuration with $V_0 = 6591\ m/s$ at $t = 1.5 \cdot 10^{-1}\ ms$ after initial impact.

For the models using DM1 and KFRP, though, simulations were aborted by the program just after the primary debris could hit the stuffing layer. This occurred because the numerical time step dropped below the prescribed Minimum time step. For all simulations the Minimum time step option was left to default, which means Autodyn® determines one based on numerical stability considerations for each step. In the data-files from the time step at which abortion occurred, it was found that for these cases a minimum time step of $3.793203 \cdot 10^{-8}$ $ms$ was enforced. Changing the permitted minimum time step from default to $1.0 \cdot 10^{-10}$ $ms$, simulations were found to continue past the moment of contact between the initial debris cloud and the stuffing layer.

Figure 12.2 shows that the SWS containing the KFRP model displayed significant fragmentation of the stuffing layer. As can be seen in Figure 12.3, the stuffing layer in the DM1-based SWS displays a narrower main spallation band. It was also found that for the DM1-based simulation, the core of the stuffing layer around the impact site was not fragmented to the point where coherence with the rest of the laminate was lost. For both KFRP- and DM2-based simulations fragmentation was predicted to this extent. For none of the considered cases, penetration of the rear wall was predicted. This seems reasonable, since the configuration simulated is based on that used on the Columbus module of the ISS, which was intended to stop impactors with a diameter up to 1.0 $cm$ in the considered velocity range [82].

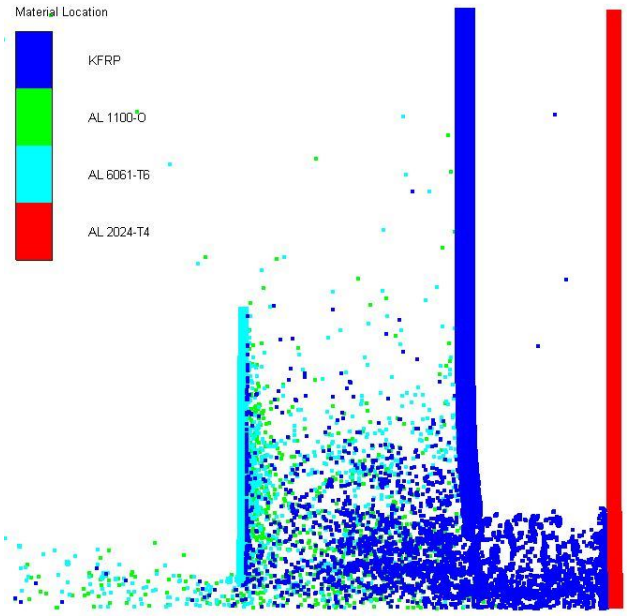


**Figure 12.2:** Simulated impact in a KFRP-based SWS configuration with $V_0 = 6591$ $m/s$ at $t = 1.5 \cdot 10^{-1}$ $ms$ after initial impact.

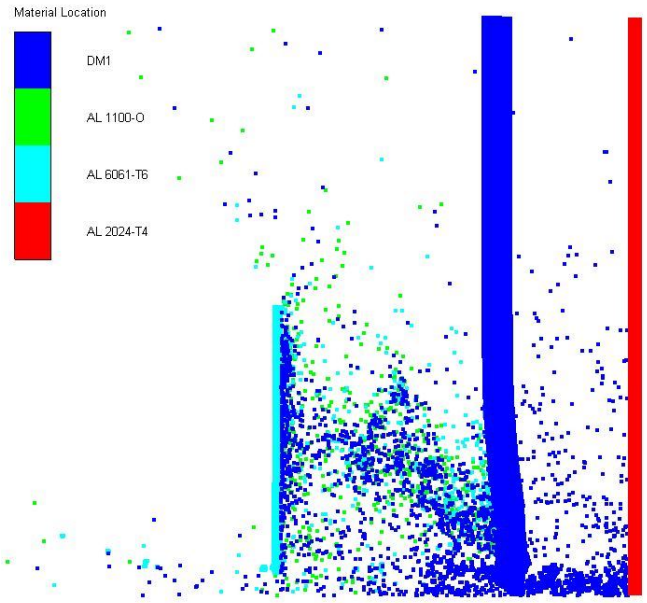


**Figure 12.3:** Simulated impact in a DM1-based SWS configuration with $V_0 = 6591\ m/s$ at $t = 1.5 \cdot 10^{-1}\ ms$ after initial impact.

## 12.4 Reflection on SWS Test Cases

After implementation of fixed minimum time steps, it was found all three test cases could run without premature termination. Only one combination of target AD, and impactor diameter and velocity was considered here, and no validation data were available of any of these cases. For any conclusive verdicts on the accuracy of the results predicted by either DM1 or DM2 in this setting, dedicated validation experiments are required.

Comparing the simulated SWS configuration containing DM1 and DM2, it was observed that for neither configuration material from the primary debris cloud was able to penetrate past the stuffing layer. The main difference in the predicted results for the two Dyneema® models is that for DM2, significant disintegration of the stuffing layer is predicted post-impact, whereas for DM1 damage to the stuffing layer appeared to be concentrated mostly at the front and rear face. This observation is accompanied by the fact that the DM1 based model predicts higher backwards ejecta velocities than were predicted by the DM2 based model. For DM2 backwards ejecta velocities were found to rarely exceed 1000 $m/s$, whereas for DM1 velocities of 3000 $m/s$ were readily achieved. Comparing simulations using DM1 and DM2, and KFRP stuffing layers, it was found that fragmentation behaviour in the KFRP layer was comparable to that observed for the DM2 model. For the KFRP based mode, backwards ejecta velocities on the order of 1200 $m/s$ were obtained. Peak forward debris cloud velocities of the composite stuffing layer were approximately 400 $m/s$ for DM1, $1,000\ m/s$ for DM2 and 550 $m/s$ for KFRP.

Further simulation test campaigns are strongly recommended. Systematically varying impactor mass and velocity to gain sets of constant or varying impactor momentum and kinetic energy can be used to obtain valuable insights into the ballistic protection Dyneema® based SWS configurations can offer, compared to other MMOD protection systems. Simulations of this kind can also be used to more efficiently plan experimental test campaigns or to aid in predicting material behaviour under conditions beyond current testing capabilities.

# Chapter 13

# Conclusions and Recommendations

This chapter contains the final conclusions and recommendations resulting from this master thesis project. The main conclusions of these reports, and how they relate to the questions formulated in Chapter 2, are presented in Section 13.1. Recommendations for further research based on these conclusions, or general observations made over the course of the project, can be found in Section 13.2.

## 13.1 Conclusions

In this section, the main conclusions of this report are presented. These are grouped by their relation to the research sub-questions. After these three sub-questions are answered, a main conclusion relating to the main research question is presented.

*Sub-question 1: What aspects of the space environment are expected to cause degradation to UHMWPE fibre-based composites, thus affecting the ballistic performance of Dyneema®-based spacecraft protection systems?*

It was found that for protection against impacts in the hypervelocity regime, multi-layered shielding configurations, such as the Stuffed Whipple Shield (SWS), form the most efficient shielding configurations. In such structures, ballistic composites are not ideal as outer walls. They should rather be used behind an outer bumper made from a denser material. Three main aspects of the space environment were identified that are expected to cause degradation of the ballistic performance of Ultra High Molecular Weight PolyEthylene (UHMWPE) fibre-based composites. These are exposure to extreme temperatures, atomic oxygen and radiation. It was also found that significant interest in the use of UHMWPE-based materials for space applications already exists because of its radiation shielding properties. If applied within a SWS configuration, it is not expected these environmental influences will compromise the viability of UHMWPE fibre-based composites. However, they should be considered during design and further material characterisation experiments are recommended.

*Sub-question 2: Can the response of Dyneema® HB26 to hypervelocity impacts accurately be predicted using an SPH-based discretisation?*

To assess the hypervelocity impact response of Dyneema®-based composites, smoothed particle hydrodynamics simulations were performed. Published material models for UHMWPE-based composites, designed for use with Lagrangian elements, were initially

used. Combining these formulations with an Smoothed Particle Hydrodynamics (SPH)-based discretisation yielded results that did not match validation data. The through-thickness compressive response of the model, brought about by the material strength formulation used, was identified as the cause for the encountered discrepancies. Two new nonlinear orthotropic hydrocode material models where therefore proposed, which were labelled DM1 and DM2.

These models were validated using footage from hypervelocity impact experiments on 15 $kg/m^2$ Dyneema® HB26 targets, with impactor velocities ranging up to 6591 $m/s$. DM2 was found to yield good prediction of residual impactor velocities, generally being within 10% of experimental data, including approximate prediction of the ballistic limit. Debris clouds generated by DM2 followed a narrow trajectory over the full considered impactor velocity range. For DM1, promising prediction of both debris cloud shape and velocity was achieved for the higher impact velocities, but performance decreased as the impact velocity decreased and approached the ballistic limit. Compared to element-based simulation, the modelling approach using the proposed models and an SPH-based discretisation constitutes an improvement in capturing both the penetration and fragmentation behaviour associated with hypervelocity impact phenomena. Further experimental characterisation and validation are required to further improve the proposed models.

*Sub-question 3: How do the ballistic performances of simulated Dyneema®- and Kevlar®-based composites compare in response to hypervelocity impacts?*

The model used for simulation of Kevlar®-epoxy targets, labelled KFRP, used the same components as the DM1 model. Simulating direct impacts into 15 $kg/m^2$ Kevlar®-epoxy targets presented under-penetration and excessive spallation, in line with those encountered for lower impact velocities using DM1. The hypothesis was formulated this behaviour was caused by the used combination of impactor diameter and target Areal Density (AD). Reducing AD indeed resulted in improved performance of both the DM1 and KFRP models. For all considered direct impact cases, the Kevlar®-epoxy model consistently predicted lower post-impact residual impactor momentum. For the considered SWS test cases, comparable ballistic performance was encountered for the Kevlar®- and Dyneema®-based systems. This basis for comparison could be improved by considering additional test cases.

*Main research question: Are UHMWPE fibre-based composites a viable material for use in spacecraft hypervelocity impact shielding, if integrated into an SWS structure as currently used aboard the Columbus module of the ISS?*

Based on the work presented in this report, using UHMWPE-based composites for spacecraft HVI shielding is considered feasible. To further establish whether it is the best design solution available, more research will be require. HVI test campaigns will be required to allow for a more complete comparison between the performance of Kevlar®- and Dyneema®-based shields. The modelling work presented in this report should also be continued and further refined. Recommendations for future work are discussed in Section 13.2.

## 13.2 Recommendations

This section contains the main recommendations for further research that follow from this project. These are grouped in the various subsections according to their respective fields of application.

### 13.2.1 Space Environment Compatibility Testing

As was pointed out in Chapter 3, publicly available compatibility testing between Dyneema® and the space environment was found to be limited. This kind of information is of paramount importance when seeking to predict the evolution of material over the mission life time of a spacecraft. Therefore three types of material ageing testing are recommended.

First, the compatibility between fibrous UHMWPE, UHMWPE fibre-based composites and the space radiation environment should be investigated. This investigation was initially envisioned to form the main part of this Master Thesis, but could not be performed within the scope of this project. The Program Advisory Committee from the KVI-Center for Advanced Radiation Technology at the University of Groningen has decided to grant a timeslot of research time at their proton accelerator for this purpose. It is strongly recommended to investigate whether this original project proposal can still be executed.

Second, the compatibility between UHMWPE, UHMWPE fibre-based composites and the space thermal environment should be investigated. Typical spacecraft designs for various mission profiles should be analysed to obtain a range of temperatures that can be expected within the ballistic composite layer in an SWS configuration. Based on this data, thermal accelerated ageing experiments should be designed. These tests should take oxygen-free environments and the full range of expected thermal conditions into account. This would help further increase the understanding the evolution of the mechanical and ballistic properties of UHMWPE-based fibres and composites in general.

### 13.2.2 High Strain Rate Material Characterisation

It was found that appropriate fundamental understanding of the high strain rate response of materials is invaluable to accurate numerical modelling of ballistic phenomenal. Further increase of the understanding of the dynamic material behaviour of UHMWPE fibre and UHMWPE fibre-based composites is therefore recommended. First, the spallation behaviour and spall strength of the material should be investigated. Experiments using SHB experiments, or alternative equivalent tests, should then be used to create a publicly available dataset containing high strain rate through-thickness compressive and shear material responses. It would also be interesting to assess how the UHMWPE molecule chain length and selected matrix system influence material response.

### 13.2.3 Experimental Validation

Given the high costs associated with the use of hypervelocity impact testing, validation data was a scarce commodity. The experimental impact data presented by Lässig et al. [8] and the footage made available by the Fraunhofer Intitut were invaluable to the success of this project. The next step should be to expand the available impact data base. Since all available impact tests where performed using one constant target AD, it is recommended to use at least one different target AD for such a follow-up campaign. This would create a firmer validation base for models such as the ones presented by Lässig et al. [8], Nguyen et al. [15] and the ones presented in this report. It would also help to confirm or deny the hypothesis formulated in this work that target thickness has a significant effect on the stability of models like the proposed DM1 model. If possible at al, the use of techniques that help discern between debris originating from the impactor and target plate would be recommended. This would help greatly in assessing to what extend the simulated and experimental internal structure of the debris cloud match. Footage of the backwards ejecta plume would also be valuable.

### 13.2.4 Model Refinement

As an overarching statement, it is of course recommended that both DM1 and DM2 are modified and updated if and when new data become available. This refers to data from the tests recommended in this Section, but also to new modelling insights in general. On a more specific note, there are several recommended steps to be taken to improve the fit of DM1 to the input data used in its creation. First, the equation of state used in DM1 should be modified to better match the experimental inverse flyer plate impact data. This can mean either expanding the number of therms in the Shock formulation, or switching to the polynomial formulation of the Orthotropic EOS. Second, an effort should be made to modify the parameters used in the Orthotropic Yield criterion to create a better fit with the material characterisation data on which it is based. In particular the mismatch between the experimental and numerical through-thickness shear data should be addressed. This includes determining the cross-coupling $a$ parameters currently set to 0. These can be determined based on plastic Poisson ratios or using combined loading experiments. Third, state dependent material properties should be identified. If adequate characterisation of these properties, or analytical prediction of their state dependence, is possible, this should be numerically implemented.

### 13.2.5 Wide Scope Follow-Up Projects

Over the duration of this project, its scope shifted from assessing the suitability of UHMWPE-based composites for spacecraft shielding applications to the creation of two numerical models to allow for SPH based hypervelocity impact simulations of the Dyneema® HB26 composite material. One-to-one comparison between the proposed models and other published models, such as the KFRP model, based only on numerical

simulations, though, remains difficult. Differences in dataset choices (laminate vs fibre in-plane test data), model sub-components (shock versus polynomial EOS formulation) and laminate type (flexible ballistic composite versus stiff epoxy based composite), to name a few areas, introduce variations. And in any case, simulations are still numerical approximations of reality. Diligent combination of experimental and numerical data should in the end be used to compare the stopping powers of various ballistic materials for spacecraft shielding applications. This would also help identify which material properties drive performance for the stuffing layers used in SWS configurations.

Therefore it is recommended to investigate the possibility of development of comparable composites using various fibre materials, such as UHMWPE, aramid, PIPD and PBO. Side by side material characterisation and HVI testing of such composites should allow for more direct information on the actual fibre performance to be obtained. Expanding these impact tests into the field of HVI testing on SWS configurations, would further allow for the identification of optimal shielding materials for spacecraft protection purposes.

# Bibliography


[1] S. M. Kurtz. *Chapter 1 - A Primer on UHMWPE*. In S. M. Kurtz, editor, *UHMWPE Biomaterials Handbook*, pages 1 – 6. Academic Press, Boston, second edition edition, 2009. ISBN 978-0-12-374721-1.

[2] J. L. J. van Dingenen. *Chapter 3 - Gel-Spun High-Performance Polyethylene Fibres*. In *High Performance Fibres*. Woodhead Publishing, 2001. ISBN 978-1-85573-539-2.

[3] Eurofibers. Ultra high molecular weight polyethylene fiber from dsm dyneema. URL, November 2010. Visited from October to 2016.

[4] P. H. Cunniff. *Dimensionless parameters for optimization of textile-based body armor systems*. In *Proceedings of the 18th International and Symposium on Ballistics*, pages 1303–1310. 1999.

[5] M. Hudspeth, X. Nie, and W. Chen. *Dynamic failure of Dyneema SK76 single fibers under biaxial shear/tension*. In *Polymer*, 53(24):5568–5574, 2012.

[6] B. Sanborn, A. M. DiLeonardi, and T. Weerasooriya. *Tensile properties of Dyneema SK76 single fibers at multiple loading rates using a direct gripping method*. In *Journal of Dynamic Behavior of Materials*, 1(1):4–14, 2015.

[7] S. Hiermaier. *Structures under crash and impact: continuum mechanics, discretization and experimental characterization*. Springer Science & Business Media, 2007.

[8] T. R. Lässig, L. H. Nguyen, M. May, W. RiedeL, U. Heisserer, H. van der Werff, and S. Hiermaier. *A non-linear orthotropic hydrocode model for ultra-high molecular weight polyethylene in impact simulations*. In *International Journal of Impact Engineering*, 75:110–122, 2014.

[9] K. Karthikeyan, B. P. Russell, N. A. Fleck, H. N. G. Wadley, and V. S. Deshpande. *The effect of shear strength on the ballistic response of laminated composite plates*. In *European Journal of Mechanics-A/Solids*, 42:35–53, 2013.

[10] M. R. O'Masta, V. S. Deshpande, and H. H N G Wadley. *Mechanisms of projectile penetration in Dyneema® encapsulated aluminum structures*. In *International Journal of Impact Engineering*, 74: 16–35, 2014.

[11] L. H. Nguyen, S. Ryan, S. J. Cimpoeru, A. P. Mouritz, and A. C. Orifici. *The effect of target thickness on the ballistic performance of ultra high molecular weight polyethylene composite*. In *International Journal of Impact Engineering*, 75:174–183, 2015.

[12] K. Thoma, W. Riedel, F. Schäfer, and S. Hiermaier. *Hypervelocity impacts and protection*. In *Space Debris*, volume 473, pages 555–567. 2001.

[13] G. Griffith, and T. Goka. *Chapter 2 - The Space Environment: Natural and Induced.* In G. Musgrave, A. Larsen, and T. Sgobba, editors, *Safety Design for Space Systems*, pages 7 – 104. Butterworth-Heinemann, Burlington, 2009. ISBN 978-0-7506-8580-1. doi: http://dx.doi.org/10.1016/B978-0-7506-8580-1.00002-6.

[14] ANSYS, Inc. *Autodyn Composite Modeling V15.0.* Manual, ANSYS, Inc., ANSYS, Inc., Southpointe, 275 Technology Drive, Canonsburg, PA 15317, United States, November 2013.

[15] L. H. Nguyen, T. R. Läessig, S. Ryan, W. Riedel, A. P. Mouritz, and A. C. Orifici. *A methodology for hydrocode analysis of ultra-high molecular weight polyethylene composite under ballistic impact.* In *Composites Part A: Applied Science and Manufacturing*, 84:224–235, 2016.

[16] P. J. Hazell, G. J. Appleby-Thomas, X. Trinquant, and D. J. Chapman. *In-fiber shock propagation in Dyneema®.* In *Journal of Applied Physics*, 110(4):043504, 2011.

[17] T. R. Lässig, F. Bagusat, M. May, and S. Hiermaier. *Analysis of the shock response of UHMWPE composites using the inverse planar plate impact test and the shock reverberation technique.* In *International Journal of Impact Engineering*, 86:240–248, 2015.

[18] F. L. Whipple. *Meteorites and space travel.* In *The astronomical journal*, 52:131, 1947.

[19] H. F. Swift, and A. K. Hopkins. *The effects of bumper material properties on the operation of spaced hypervelocity particle shields.* Technical report, DTIC Document, 1968.

[20] ESA Requirements and Standards Division. *Space engineering: Space environment.* Standard, ESA Requirements and Standards Division, ESTEC, P.O. Box 299, 2200 AG Noordwijk, The Netherlands, November 2008.

[21] R. Destefanis, F. Schäfer, M. Lambert, and M. Faraud. *Selecting enhanced space debris shields for manned spacecraft.* In *International journal of impact engineering*, 33(1):219–230, 2006.

[22] W. P. Schonberg. Characterizing the material in a debris cloud created in a hypervelocity impact. In *Proceedings First European Conference on Space Debris*, 1993.

[23] W. P. Schonberg. *Debris Cloud Material Characterisation for Hypervelocity Impacts of Single- and Multi-Material Projectiles.* Report, Universty of Alabama in Huntsville, Huntsville, AL, United States, May 1994.

[24] W. P. Schonberg, and E. J. Walker. *Use of composite materials in multi-wall structures to prevent perforation by hypervelocity particle impact.* In *Composite structures*, 19(1):15–40, 1991.

[25] E. L. Christiansen, and J. H. Kerr. *Mesh double-bumper shield: a low-weight alternative for spacecraft meteoroid and orbital debris protection.* In *International Journal of Impact Engineering*, 14 (1-4):169–180, 1993.

[26] M. Millinger. Private correspondence with dr. mark millinger, 2016. Space Environments and Effects division at the European Space Agency.

[27] S. Ryan, T. Hedman, and E. L. Christiansen. *Honeycomb vs. foam: Evaluating potential upgrades to ISS module shielding.* In *Acta astronautica*, 67(7):818–825, 2010.

[28] S. J. Ryan, E. L. Christiansen, and D. M. Lear. *Development of the Next Generation of Meteoroid and Orbital Debris Shields.* Report, USRA Lunar and Planetary Institute, Houston, Texas 77058, United States, 2009.

[29] S. Ryan, and E. L. Christiansen. *Hypervelocity impact testing of advanced materials and structures for micrometeoroid and orbital debris shielding.* In *Acta Astronautica*, 83:216–231, 2013.

[30] R. Destefanis, F. Schäfer, M. Lambert, M. Faraud, and E. Schneider. *Enhanced space debris shields for manned spacecraft.* In *International journal of impact engineering*, 29(1):215–226, 2003.

[31] K. Thoma, F. Schäfer, S. Hiermaier, and E. Schneider. *An approach to achieve progress in spacecraft shielding.* In *Advances in Space research*, 34(5):1063–1075, 2004.

[32] S. Khatiwada, C. A. Armada, and E. V. Barrera. *Hypervelocity impact experiments on epoxy/-high molecular weight polyethylene fiber composites reinforced with single-walled carbon nanotubes.* In *Procedia Engineering*, 58:4–10, 2013.

[33] S. Sen, E. Schofield, J. S. O'Dell, L. Deka, and S. Pillay. *The development of a multifunctional composite material for use in human space exploration beyond low-earth orbit.* In *JOM*, 61(1):23–31, 2009.

[34] J. R. Wertz, D. F. Everett, and J. J. Puschell. *Space Mission Eningeering: The New SMAD.* Microcosm Press and Springer, 20. ISBN 978-1-881-883-15-9.

[35] M. M. Finckenor, J. A. Vaughn, and E. Watts. Changes in polymeric tether properties due to atomic oxygen. In *42nd AIAA Aerospace Sciences Meeting, Reno, NV*, 2004.

[36] V. L. Pisacane. *Chapter 7 - Spacecraft Thermal Control.* In *Fundamentals of Space Systems (2nd Edition).* Oxford University Press, 2005. ISBN 978-0-19-516205-9.

[37] J. H. Meulman, H. van der Werf, S. Chabba, and A. Vunderink. *Ballistic performance of Dyneema® at elevated temperatures, extreme for body armor.* Report, DSM Dyneema, P.O. Box 1163, 6160 BD Geleen, The Netherlands, 2010.

[38] T. Peijs, E. A. M. Smets, and L. E. Govaert. *Strain rate and temperature effects on energy absorption of polyethylene fibres and composites.* In *Applied composite materials*, 1(1):35–54, 1994.

[39] S. Chabba, M. V. Es, E. J. V. Klinken, M. J. Jongedijk, D. Vanek, P. Gijsman, and A. C. L. M. van der Waals. *Accelerated aging study of ultra high molecular weight polyethylene yarn and unidirectional composites for ballistic applications.* In *Journal of materials science*, 42(8):2891–2893, 2007.

[40] X. Liu, and W. Yu. *Evaluation of the tensile properties and thermal stability of ultra-high-molecular-weight polyethylene fibers.* In *Journal of applied polymer science*, 97(1):310–315, 2005.

[41] A. L. Forster, A. M. Forster, J. W. Chin, J. Peng, C. Lin, S. Petit, K. Kang, N. Paulter, M. A. Riley, K. D. Rice, et al. *Long-term stability of UHMWPE fibers.* In *Polymer Degradation and Stability*, 114:45–51, 2015.

[42] M. Fejdyś, M. Łandwijt, and M. H. Struszczyk. *Effect of accelerated ageing conditions on the degradation process of Dyneema® polyethylene composites.* In *Fibres & Textiles in Eastern Europe*, 19(1):84, 2011.

[43] S. Bourdarie, and M. Xapsos. *The near-earth space radiation environment.* In *IEEE Transactions on Nuclear Science*, 55(4):1810–1832, 2008.

[44] C. Zeitlin, D. M. Hassler, F. A. Cucinotta, B. Ehresmann, R. F. Wimmer-Schweingruber, D. E. Brinza, S. Kang, G. Weigle, S. Boettcher, E. Boehm, et al. *Measurements of energetic particle radiation in transit to Mars on the Mars Science Laboratory.* In *Science*, 340(6136):1080–1084, 2013.

[45] J. A. Simpson. *Elemental and isotopic composition of the galactic cosmic rays.* In *Annual Review of Nuclear and Particle Science*, 33(1):323–382, 1983.

[46] G. D. Badhwar, and P. M. O'Neill. *An improved model of galactic cosmic radiation for space exploration missions.* In *International Journal of Radiation Applications and Instrumentation. Part D. Nuclear Tracks and Radiation Measurements*, 20(3):403–410, 1992.

[47] G. D. Badhwar, and P. M. O'Neill. *Galactic cosmic radiation model and its applications.* In *Advances in Space Research*, 17(2):7–17, 1996.

[48] P. M. O'Neill. *Badhwar–O'Neill galactic cosmic ray model update based on advanced composition explorer (ACE) energy spectra from 1997 to present.* In *Advances in Space Research*, 37(9):1727–1733, 2006.

[49] B. O. Taylor, C. I. Underwood, G. Vacanti, and E. Maddox. *The interplanetary electron model (IEM).* In *IEEE Transactions on Nuclear Science*, 6(58):2785–2792, 2011.

[50] R. A. Nymmik. *Improved environment radiation models.* In *Advances in Space Research*, 40(3):313–320, 2007.

[51] N. A. Schwadron, J. B. Blake, A. W. Case, C. J. Joyce, J. Kasper, J. Mazur, N. Petro, M. Quinn, J. A. Porter, C. W. Smith, et al. *Does the worsening galactic cosmic radiation environment observed by CRaTER preclude future manned deep space exploration?* In *Space Weather*, 12(11):622–632, 2014.

[52] R. A. Nymmik, M. I. Panasyuk, and A. A. Suslov. *Galactic cosmic ray flux simulation and prediction.* In *Advances in Space Research*, 17(2):19–30, 1996.

[53] D. H. Hathaway. *The Solar Cycle.* In *Living Reviews in Solar Physics*, 7(1), 2010. doi: 10.1007/lrsp-2010-1.

[54] P. M. Sforza. *Chapter 3 - The Space Environment.* In *Manned Spacecraft Design Principles.* Elsevier, 2016. ISBN 978-0-12-804425-4.

[55] Royal Belgian Institute for Space Aeronomy and others. Spenvis. URL, September 2016. Visited from September to 2016.

[56] F. A. Cucinotta, M. Y. Kim, and L. J. Chappell. *Evaluating Shielding Approaches to Reduce Space Radiation Cancer Risks.* Report, NASA Johnson Space Center, Houston, TX 77058, United States, May 2012.

[57] S. A. Thibeault, J. H. Kang, G. Sauti, C. Park, C. C. Fay, and G. C. King. *Nanomaterials for radiation shielding.* In *MRS Bulletin*, 40(10):836–841, 2015.

[58] G. A. Nelson. *Space Radiation and Human Exposures, A Primer.* In *Radiation research*, 185(4):349–358, 2016.

[59] M. Durante, and F. A. Cucinotta. *Heavy ion carcinogenesis and human space exploration.* In *Nature Reviews Cancer*, 8(6):465–472, 2008.

[60] F. A. Cucinotta, and M. Durante. *Cancer risk from exposure to galactic cosmic rays: implications for space exploration by human beings.* In *The lancet oncology*, 7(5):431–435, 2006.

[61] S. Nambiar, and J. T. W. Yeow. *Polymer-composite materials for radiation protection.* In *ACS applied materials & interfaces*, 4(11):5717–5726, 2012.

[62] Y. Zhao, M. Wang, Z. Tang, and G. Wu. *Radiation effects of UHMW-PE fibre on gel fraction and mechanical properties.* In *Radiation Physics and Chemistry*, 80(2):274–277, 2011.

[63] D. J. Dijkstra, and A. J. Pennings. *Cross-linking of ultra-high strength polyethylene fibres by means of electron beam irradiation.* In *Polymer Bulletin*, 17(6):507–513, 1987.

[64] C. Gao, S. Li, H. Song, and L. Xie. *Radiation-induced crosslinking of ultra high molecular weight polyethylene fibers by means of electron beams.* In *Journal of applied polymer science*, 98(4):1761–1764, 2005.

[65] A. M. Visco, L. Torrisi, N. Campo, U. Emanuele, A. Trifirò, and M. Trimarchi. *Mechanical performance of electron-beam-irradiated UHMWPE in vacuum and in air.* In *Journal of Biomedical Materials Research Part B: Applied Biomaterials*, 89(1):55–64, 2009.

[66] Y. Zhao, M. Wang, Z. Tang, and G. Wu. *ESR study of free radicals in UHMW-PE fiber irradiated by gamma rays.* In *Radiation Physics and Chemistry*, 79(4):429–433, 2010.

[67] C. J. Hayhurst, I. H. Livingstone, R. A. Clegg, G. E. Fairlie, S. J. Hiermaier, and M. Lambert. Numerical simulation of hypervelocity impacts on aluminum and nextel/kevlar whipple shields. In *Proceedings of the Hypervelocity Shielding Workshop*, pages 61–72, 1998.

[68] R. A. Clegg, D. M. White, W. Riedel, and W. Harwick. *Hypervelocity impact damage prediction in composites: Part I-material model and characterisation.* In *International Journal of Impact Engineering*, 33(1):190–200, 2006.

[69] W. Riedel, H. Nahme, D. M. White, and R. A. Clegg. *Hypervelocity impact damage prediction in composites: Part II-experimental investigations and simulations.* In *International Journal of Impact Engineering*, 33(1):670–680, 2006.

[70] M. Wicklein, S. Ryan, D. M. White, and R. A. Clegg. *Hypervelocity impact on CFRP: testing, material modelling, and numerical simulation.* In *International Journal of Impact Engineering*, 35 (12):1861–1869, 2008.

[71] M. Grujicic, G. Arakere, T. He, W. C. Bell, P. S. Glomski, and B. A. Cheeseman. *Multi-scale ballistic material modeling of cross-plied compliant composites.* In *Composites Part B: Engineering*, 40(6):468–482, 2009.

[72] S. Chocron, A. E. Nicholls, A. Brill, A. Malka, T. Namir, D. Havazelet, H. van der Werff, U. Heisserer, and J. D. Walker. *Modeling unidirectional composites by bundling fibers into strips with experimental determination of shear and compression properties at high pressures.* In *Composites Science and Technology*, 101:32–40, 2014.

[73] L. H. Nguyen, T. R. Lässig, S. Ryan, W. Riedel, A. P. Mouritz, and A. C. Orifici. *Numerical Modelling of Ultra-High Molecular Weight Polyethylene Composite under Impact Loading.* In *Procedia Engineering*, 103:436–443, 2015.

[74] C. E. A. Jr, P. A. Cox, G. R. Johnson, and P. J. Maudlin. *A constitutive formulation for anisotropic materials suitable for wave propagation computer programs-II.* In *Computational Mechanics*, 15(3): 201–223, 1994.

[75] J. K. Chen, F. A. Allahdadi, and C. T. Sun. *A quadratic yield function for fiber-reinforced composites.* In *Journal of composite materials*, 31(8):788–811, 1997.

[76] ANSYS, Inc. Ansys explicit dynamics solutions v12.1, 2009.

[77] ANSYS, Inc. *ANSYS Autodyn User's Manual V15.0.* Manual, ANSYS, Inc., ANSYS, Inc., Southpointe, 275 Technology Drive, Canonsburg, PA 15317, United States, November 2013.

[78] V. Leus, Y. Neumann, and E. Racah. *Experimental and Numerical Study of Aluminum 6061-T6 Fragmentation Process at Very High Strain Rates.* In *Proceedings of the 26th International Symposium on Ballistics.* Defence Technical Information Center, 2011.

[79] J. W. Swegle, D. L. Hicks, and S. W. Attaway. *Smoothed particle hydrodynamics stability analysis.* In *Journal of computational physics*, 116(1):123–134, 1995.

[80] G.-R. Liu, and M. B. Liu. *Smoothed particle hydrodynamics: a meshfree particle method.* World Scientific, 2003.

[81] M. B. Liu, and G. R. Liu. *Smoothed particle hydrodynamics (SPH): an overview and recent developments.* In *Archives of computational methods in engineering*, 17(1):25–76, 2010.

[82] H. Klinkrad. *Chapter 10 - Meteoroid and Debris Protection.* In G. E. Musgrave, A. M. Larsen, and T. Sgobba, editors, *Safety Design for Space Systems*, pages 319 – 340. Butterworth-Heinemann, Burlington, 2009. ISBN 978-0-7506-8580-1. doi: http://dx.doi.org/10.1016/B978-0-7506-8580-1.00010-5. URL.

[83] A. J. Piekutowski. *Characteristics of debris clouds produced by hypervelocity impact of aluminum spheres with thin aluminum plates.* In *International Journal of Impact Engineering*, 14(1-4):573–586, 1993.

[84] D. R. Ek, and J. R. Asay. *The stress and strain rate dependence of spall strength in two aluminum alloys.* In Y. M. Gupta, editor, *Shock Waves in Condensed Matter*, pages 413 – 424. Plenum Press, New York, 1986. ISBN 0-306-42276-X.

[85] D. E. Grady. *The spall strength of condensed matter.* In *Journal of the Mechanics and Physics of Solids*, 36(3):353–384, 1988.

[86] M. Grujicic, P. Glomski, T. He, G. Arakere, W. Bell, and B. Cheeseman. *Material modeling and ballistic-resistance analysis of armor-grade composites reinforced with high-performance fibers.* In *Journal of Materials Engineering and Performance*, 18(9):1169, 2009.

[87] ANSYS, Inc. *ANSYS Mechanical User's Guide V15.0.* Manual, ANSYS, Inc., ANSYS, Inc., Southpointe, 275 Technology Drive, Canonsburg, PA 15317, United States, November 2013.

[88] M. Ruiz-Ripoll, O. Millon, T. Lässig, and W. Riedel. Experimental characterization of the out-of-plane shear strength of ultra-high molecular weight polyethylene composite by using the split hopkinson bar device. In *17th European Conference on Composite Materials*, 2016.

[89] Century Dynamics Ltd. *Autodyn Explicit Software for Nonlinear Dynamics SPH User Manual & Tutorial.* Manual, ANSYS, Inc., Century Dynamics Ltd, Dynamics House, Hurst Road, Horsham, West Sussex, RH12 2DT, England, 2005.

[90] T. R. Lässig. Private correspondence with dr. ing. torsten lässig, 2017. Fraunhofer Institute for High-Speed Dynamics, Ernst-Mach-Institut.

[91] L. H. Nguyen. Private correspondence with dr. l h nguyen, 2017. Australian Government Department of Defence Science and Technology Group.

[92] U. Heisserer. *Dyneema® material information for ballistic modeling.* Report, DSM, Geleen, The Netherlands, 2013.

[93] T. Lässig. *Dynamic characterization and modeling of Dyneema.* Report I-49/2012, Fraunhofer EMI, Freiburg, Germany, 2012.

[94] R. G. McQueen. *Selected hugoniots.* Report, Los Alamos National Laboratory, Los Alamos, New Mexico, 1969.

[95] I. Rohr, H. Nahme, and K. Thoma. *Material characterization and constitutive modelling of ductile high strength steel for a wide range of strain rates.* In *International Journal of Impact Engineering*, 31(4):401–433, 2005.

[96] L. H. Nguyen. *The Ballistic Performance of Thick Ultra High Molecular Weight Polyethylene Composite*. Ph.d. dissertation, RMIT University, Melbourne, Vic, Australia, December 2015.

[97] K. Shaker, A. Jabbar, M. Karahan, N. Karahan, and Y. Nawab. *Study of dynamic compressive behaviour of aramid and ultrahigh molecular weight polyethylene composites using Split Hopkinson Pressure Bar*. In *Journal of Composite Materials*, 51(1):81–94, 2017.

[98] DSM Dyneema. *Fact Sheet: Dyneema high strength, high modulus polyethylene fiber*. Report, DSM, Urmond, The Netherlands, 2008.

# Appendix A

# Material Models

## A.1 DM0 Parameters

**Table A.1:** Input parameters for the DM0 material model based on [15].

| Parameter | Value | Unit | Parameter | Value | Unit |
|---|---|---|---|---|---|
| EOS: Orthotropic | | | Strength: Orthotropic yield | | |
| Reference Density | 0.98 | $g/cm^3$ | Plasticity constant 11 | 0.016 | – |
| Young's modulus 11 | $3.62 \cdot 10^6$ | $kPa$ | Plasticity constant 22 | $6 \cdot 10^{-4}$ | – |
| Young's modulus 22 | $5.11 \cdot 10^7$ | $kPa$ | Plasticity constant 33 | $6 \cdot 10^{-4}$ | – |
| Young's modulus 33 | $5.11 \cdot 10^7$ | $kPa$ | Plasticity constant 12 | 0 | – |
| Poisson's Ratio 12 | 0.013 | – | Plasticity constant 23 | 0 | – |
| Poisson's Ratio 23 | 0 | – | Plasticity constant 31 | 0 | – |
| Poisson's Ratio 31 | 0.5 | – | Plasticity constant 44 | 1 | – |
| Shear modulus 12 | $2.0 \cdot 10^6$ | $kPa$ | Plasticity constant 55 | 1.7 | – |
| Shear modulus 23 | $1.92 \cdot 10^5$ | $kPa$ | Plasticity constant 66 | 1.7 | – |
| Shear modulus 31 | $2.0 \cdot 10^6$ | $kPa$ | Eff. Stress #1 | $1.48 \cdot 10^3$ | $kPa$ |
| | | | Eff. Stress #2 | $7.0 \cdot 10^3$ | $kPa$ |
| Volumetric Response: Shock | | | Eff. Stress #3 | $2.7 \cdot 10^4$ | $kPa$ |
| Grüneisen coefficient | 1.64 | – | Eff. Stress #4 | $4.0 \cdot 10^4$ | $kPa$ |
| Parameter C1 | $3.57 \cdot 10^3$ | $m/s$ | Eff. Stress #5 | $5.0 \cdot 10^4$ | $kPa$ |
| Parameter S1 | 2.3 | – | Eff. Stress #6 | $6.0 \cdot 10^4$ | $kPa$ |
| Reference Temperature | 293 | $K$ | Eff. Stress #7 | $8.0 \cdot 10^4$ | $kPa$ |
| Specific Heat | $1.85 \cdot 10^3$ | $J/kgK$ | Eff. Stress #8 | $9.8 \cdot 10^4$ | $kPa$ |
| | | | Eff. Stress #9 | $2.0 \cdot 10^5$ | $kPa$ |
| Failure: Orthotropic softening | | | Eff. Stress #10 | $1.0 \cdot 10^6$ | $kPa$ |
| Tensile failure stress 11 | $4.50 \cdot 10^4$ | $kPa$ | Eff. Plastic Strain #1 | 0.00 | – |
| Tensile failure stress 22 | $1.15 \cdot 10^6$ | $kPa$ | Eff. Plastic Strain #2 | 0.01 | – |
| Tensile failure stress 33 | $1.15 \cdot 10^6$ | $kPa$ | Eff. Plastic Strain #3 | 0.1 | – |
| Maximum shear stress 12 | $5.75 \cdot 10^5$ | $kPa$ | Eff. Plastic Strain #4 | 0.15 | – |
| Maximum shear stress 23 | $1.20 \cdot 10^5$ | $kPa$ | Eff. Plastic Strain #5 | 0.175 | – |
| Maximum shear stress 31 | $5.75 \cdot 10^5$ | $kPa$ | Eff. Plastic Strain #6 | 0.19 | – |
| Fracture energy 11 | 790 | $J/m^2$ | Eff. Plastic Strain #7 | 0.200 | – |
| Fracture energy 22 | 30 | $J/m^2$ | Eff. Plastic Strain #8 | 0.205 | – |
| Fracture energy 33 | 30 | $J/m^2$ | Eff. Plastic Strain #9 | 0.210 | – |
| Fracture energy 12 | $1.46 \cdot 10^3$ | $J/m^2$ | Eff. Plastic Strain #10 | 0.215 | – |
| Fracture energy 23 | $1.46 \cdot 10^3$ | $J/m^2$ | | | |
| Fracture energy 31 | $1.46 \cdot 10^3$ | $J/m^2$ | | | |
| Damage coupling coefficient | 0.50 | – | | | |

## A.2 IM1 Parameters

**Table A.2:** Input parameters for the IM1 material model based on [15].

| Parameter | Value | Unit | Parameter | Value | Unit |
|---|---|---|---|---|---|
| EOS: Orthotropic | | | Failure: Material Stress | | |
| Reference Density | 0.98 | $g/cm^3$ | Tensile Failure Stress 11 | $4.50 \cdot 10^4$ | $kPa$ |
| Young's modulus 11 | $3.62 \cdot 10^6$ | $kPa$ | Tensile Failure Stress 22 | $1.15 \cdot 10^6$ | $kPa$ |
| Young's modulus 22 | $5.11 \cdot 10^7$ | $kPa$ | Tensile Failure Stress 33 | $1.15 \cdot 10^6$ | $kPa$ |
| Young's modulus 33 | $5.11 \cdot 10^7$ | $kPa$ | Maximum Shear Stress 12 | $5.75 \cdot 10^5$ | $kPa$ |
| Poisson's Ratio 12 | 0.013 | – | Maximum Shear Stress 23 | $1.20 \cdot 10^5$ | $kPa$ |
| Poisson's Ratio 23 | 0 | – | Maximum Shear Stress 31 | $5.75 \cdot 10^5$ | $kPa$ |
| Poisson's Ratio 31 | 0.5 | – | | | |
| Shear modulus 12 | $2.0 \cdot 10^6$ | $kPa$ | Post Failure Option: Isotropic | | |
| Shear modulus 23 | $1.92 \cdot 10^5$ | $kPa$ | | | |
| Shear modulus 31 | $2.0 \cdot 10^6$ | $kPa$ | Strength: Von Mises | | |
| | | | Shear Modulus | $2.0 \cdot 10^6$ | $kPa$ |
| Volumetric Response: Shock | | | Yield Stress | – | $kPa$ |
| Grüneisen coefficient | 1.64 | – | | | |
| Parameter C1 | $3.57 \cdot 10^3$ | $m/s$ | | | |
| Parameter S1 | 1.3 | – | | | |
| Reference Temperature | 293 | $K$ | | | |
| Specific Heat | $1.85 \cdot 10^3$ | $J/kgK$ | | | |

## A.3 IM2-4 Parameters

**Table A.3:** Input parameters for the IM2-4 material model based on [15].

| Parameter | Value | Unit | Parameter | Value | Unit |
|---|---|---|---|---|---|
| EOS: Orthotropic | | | Failure: Material Stress | | |
| Reference Density | 0.98 | $g/cm^3$ | Tensile Failure Stress 11 | $4.50 \cdot 10^4$ | $kPa$ |
| Young's modulus 11 | $3.62 \cdot 10^6$ | $kPa$ | Tensile Failure Stress 22 | $1.15 \cdot 10^6$ | $kPa$ |
| Young's modulus 22 | $5.11 \cdot 10^7$ | $kPa$ | Tensile Failure Stress 33 | $1.15 \cdot 10^6$ | $kPa$ |
| Young's modulus 33 | $5.11 \cdot 10^7$ | $kPa$ | Maximum Shear Stress 12 | $1.56 \cdot 10^5$ | $kPa$ |
| Poisson's Ratio 12 | 0.013 | – | Maximum Shear Stress 23 | $1.20 \cdot 10^5$ | $kPa$ |
| Poisson's Ratio 23 | 0 | – | Maximum Shear Stress 31 | $1.56 \cdot 10^5$ | $kPa$ |
| Poisson's Ratio 31 | 0.5 | – | | | |
| Shear modulus 12 | $2.0 \cdot 10^6$ | $kPa$ | Post Failure Option: Ortho | Table 7.2 | |
| Shear modulus 23 | $1.92 \cdot 10^5$ | $kPa$ | | | |
| Shear modulus 31 | $2.0 \cdot 10^6$ | $kPa$ | Strength: Von Mises | | |
| | | | Shear Modulus | $2.0 \cdot 10^6$ | $kPa$ |
| Volumetric Response: Shock | | | Yield Stress | $2.0 \cdot 10^4$ | $kPa$ |
| Grüneisen coefficient | 1.64 | – | | | |
| Parameter C1 | $3.57 \cdot 10^3$ | $m/s$ | | | |
| Parameter S1 | 1.3 | – | | | |
| Reference Temperature | 293 | $K$ | | | |
| Specific Heat | $1.85 \cdot 10^3$ | $J/kgK$ | | | |

## A.4 KFRP Parameters

**Table A.4:** Input parameters for the KFRP material model taken from [68].

| Parameter | Value | Unit | Parameter | Value | Unit |
|---|---|---|---|---|---|
| EOS: Orthotropic | | | Strength: Orthotropic yield | | |
| Reference Density | 1.65 | $g/cm^3$ | Plasticity constant 11 | 1.5 | – |
| Young's modulus 11 | $1.948 \cdot 10^6$ | $kPa$ | Plasticity constant 22 | 1.0 | – |
| Young's modulus 22 | $1.79898 \cdot 10^7$ | $kPa$ | Plasticity constant 33 | 1.0 | – |
| Young's modulus 33 | $1.79898 \cdot 10^7$ | $kPa$ | Plasticity constant 12 | $-0.68$ | – |
| Poisson's Ratio 12 | 0.0756 | – | Plasticity constant 23 | $-0.68$ | – |
| Poisson's Ratio 23 | 0.0756 | – | Plasticity constant 31 | $-0.26$ | – |
| Poisson's Ratio 31 | 0.698 | – | Plasticity constant 44 | 4.0 | – |
| Shear modulus 12 | $2.235 \cdot 10^5$ | $kPa$ | Plasticity constant 55 | 4.0 | – |
| Shear modulus 23 | $1.857 \cdot 10^6$ | $kPa$ | Plasticity constant 66 | 4.0 | – |
| Shear modulus 31 | $2.235 \cdot 10^5$ | $kPa$ | Eff. Stress #1 | $1.55 \cdot 10^5$ | $kPa$ |
| | | | Eff. Stress #2 | $1.55 \cdot 10^5$ | $kPa$ |
| Volumetric Response: Polynomial | | | Eff. Stress #3 | $1.67 \cdot 10^5$ | $kPa$ |
| Parameter A1 | $5.89499 \cdot 10^6$ | $kPa$ | Eff. Stress #4 | $1.78 \cdot 10^5$ | $kPa$ |
| Parameter A2 | $5.0 \cdot 10^7$ | $kPa$ | Eff. Stress #5 | $1.87 \cdot 10^5$ | $kPa$ |
| Parameter T1 | $5.89499 \cdot 10^6$ | – | Eff. Stress #6 | $1.93 \cdot 10^5$ | $kPa$ |
| Reference Temperature | 300 | K | Eff. Stress #7 | $2.10 \cdot 10^5$ | $kPa$ |
| Specific Heat | $1.42 \cdot 10^3$ | $J/kgK$ | Eff. Stress #8 | $2.35 \cdot 10^5$ | $kPa$ |
| | | | Eff. Stress #9 | $2.52 \cdot 10^5$ | $kPa$ |
| Failure: Orthotropic softening | | | Eff. Stress #10 | $3.16 \cdot 10^5$ | $kPa$ |
| Tensile failure stress 11 | $4.50 \cdot 10^4$ | $kPa$ | Eff. Plastic Strain #1 | 0.0 | – |
| Tensile failure stress 22 | $2.45 \cdot 10^5$ | $kPa$ | Eff. Plastic Strain #2 | $9.0 \cdot 10^{-6}$ | – |
| Tensile failure stress 33 | $2.45 \cdot 10^5$ | $kPa$ | Eff. Plastic Strain #3 | $6.2 \cdot 10^{-4}$ | – |
| Maximum shear stress 12 | $1.40 \cdot 10^4$ | $kPa$ | Eff. Plastic Strain #4 | $1.9 \cdot 10^{-3}$ | – |
| Maximum shear stress 23 | $2.0 \cdot 10^5$ | $kPa$ | Eff. Plastic Strain #5 | $2.5 \cdot 10^{-3}$ | – |
| Maximum shear stress 31 | $1.40 \cdot 10^4$ | $kPa$ | Eff. Plastic Strain #6 | $5.0 \cdot 10^{-3}$ | – |
| Fracture energy 11 | 544.71 | $J/m^2$ | Eff. Plastic Strain #7 | $8.8 \cdot 10^{-3}$ | – |
| Fracture energy 22 | 30 | $J/m^2$ | Eff. Plastic Strain #8 | $9.0 \cdot 10^{-6}$ | – |
| Fracture energy 33 | 30 | $J/m^2$ | Eff. Plastic Strain #9 | – | – |
| Fracture energy 12 | $1.46 \cdot 10^3$ | $J/m^2$ | Eff. Plastic Strain #10 | – | – |
| Fracture energy 23 | $1.46 \cdot 10^3$ | $J/m^2$ | | | |
| Fracture energy 31 | $1.46 \cdot 10^3$ | $J/m^2$ | | | |
| Damage coupling coefficient | 0.50 | – | | | |

## A.5 C45 Parameters

**Table A.5:** Input parameters for the C45 material model based on [95].

| Parameter | Value | Unit |
|---|---|---|
| EOS: Shock | | |
| Grüneisen coefficient | 1.664 | – |
| Parameter C1 | $4.483 \cdot 10^3$ | $m/s$ |
| Parameter S1 | 1.335 | – |
| Reference Temperature | 300 | $K$ |
| Specific Heat | 420 | $J/kgK$ |
| | | |
| Strength: Elastic | | |
| Shear Modulus | $8.1 \cdot 10^7$ | $kPa$ |

## A.6 HB26T Parameters

**Table A.6:** Input parameters for the HB26T material model taken from [8].

| Parameter | Value | Unit | Parameter | Value | Unit |
|---|---|---|---|---|---|
| EOS: Orthotropic | | | Strength: Orthotropic yield | | |
| Reference Density | 0.98 | $g/cm^3$ | Plasticity constant 11 | 0.03 | – |
| Young's modulus 11 | $3.62 \cdot 10^6$ | $kPa$ | Plasticity constant 22 | $1.0 \cdot 10^{-5}$ | – |
| Young's modulus 22 | $2.69 \cdot 10^7$ | $kPa$ | Plasticity constant 33 | $1.0 \cdot 10^{-5}$ | – |
| Young's modulus 33 | $2.69 \cdot 10^7$ | $kPa$ | Plasticity constant 12 | $1.0 \cdot 10^{-6}$ | – |
| Poisson's Ratio 12 | 0.013 | – | Plasticity constant 23 | $1.0 \cdot 10^{-6}$ | – |
| Poisson's Ratio 23 | 0 | – | Plasticity constant 31 | $1.0 \cdot 10^{-6}$ | – |
| Poisson's Ratio 31 | 0.5 | – | Plasticity constant 44 | 1 | – |
| Shear modulus 12 | $3.07 \cdot 10^4$ | $kPa$ | Plasticity constant 55 | 1.75 | – |
| Shear modulus 23 | $4.23 \cdot 10^4$ | $kPa$ | Plasticity constant 66 | 1.75 | – |
| Shear modulus 31 | $3.07 \cdot 10^4$ | $kPa$ | Eff. Stress #1 | $1.76 \cdot 10^2$ | $kPa$ |
| | | | Eff. Stress #2 | $9.89 \cdot 10^2$ | $kPa$ |
| Volumetric Response: Shock | | | Eff. Stress #3 | $1.74 \cdot 10^3$ | $kPa$ |
| Parameter A1 & T1 | $7.04 \cdot 10^6$ | $kPa$ | Eff. Stress #4 | $2.42 \cdot 10^3$ | $kPa$ |
| Parameter A2 | $1.0 \cdot 10^7$ | $kPa$ | Eff. Stress #5 | $3.10 \cdot 10^3$ | $kPa$ |
| Parameter B0 & B1 | 3.864 | – | Eff. Stress #6 | $5.97 \cdot 10^3$ | $kPa$ |
| Reference Temperature | 293 | $K$ | Eff. Stress #7 | $1.20 \cdot 10^4$ | $kPa$ |
| Specific Heat | $1.85 \cdot 10^3$ | $J/kgK$ | Eff. Stress #8 | $2.07 \cdot 10^4$ | $kPa$ |
| | | | Eff. Stress #9 | $3.46 \cdot 10^4$ | $kPa$ |
| Failure: Orthotropic softening | | | Eff. Stress #10 | $2.02 \cdot 10^8$ | $kPa$ |
| Tensile failure stress 11 | $1.07 \cdot 10^3$ | $kPa$ | Eff. Plastic Strain #1 | $1.82 \cdot 10^{-4}$ | – |
| Tensile failure stress 22 | $7.53 \cdot 10^5$ | $kPa$ | Eff. Plastic Strain #2 | $1.20 \cdot 10^{-3}$ | – |
| Tensile failure stress 33 | $7.53 \cdot 10^5$ | $kPa$ | Eff. Plastic Strain #3 | $3.11 \cdot 10^{-3}$ | – |
| Maximum shear stress 12 | $1.01 \cdot 10^{20}$ | $kPa$ | Eff. Plastic Strain #4 | $6.92 \cdot 10^{-3}$ | – |
| Maximum shear stress 23 | $3.52 \cdot 10^4$ | $kPa$ | Eff. Plastic Strain #5 | $1.13 \cdot 10^{-2}$ | – |
| Maximum shear stress 31 | $1.01 \cdot 10^{20}$ | $kPa$ | Eff. Plastic Strain #6 | $2.83 \cdot 10^{-2}$ | – |
| Fracture energy 11 | 790 | $J/m^2$ | Eff. Plastic Strain #7 | $5.78 \cdot 10^{-2}$ | – |
| Fracture energy 22 | 30 | $J/m^2$ | Eff. Plastic Strain #8 | $1.06 \cdot 10^{-1}$ | – |
| Fracture energy 33 | 30 | $J/m^2$ | Eff. Plastic Strain #9 | $1.061 \cdot 10^{-1}$ | – |
| Fracture energy 12 | 1.46 | $J/m^2$ | Eff. Plastic Strain #10 | 1.0 | – |
| Fracture energy 23 | 1.46 | $J/m^2$ | | | |
| Fracture energy 31 | 1.46 | $J/m^2$ | | | |
| Damage coupling coefficient | 0.50 | – | | | |